

國立交通大學

電信工程研究所

博士論文

一位元高精確度之載波相位估計及高運算  
效率之碼相位擷取

One-bit High-Accuracy Carrier Phase  
Estimation and Computationally-Efficient  
Code Phase Acquisition

研究生：謝萬信

指導教授：高銘盛

中華民國 100 年 12 月

# 一位元高精確度之載波相位估計及高運算效率之碼相位擷取

研究生：謝萬信

指導教授：高銘盛 博士

國立交通大學 電機資訊學院  
電信工程研究所

## 摘要

本論文首先探討高精確度之一位元載波相位估計，我們根據訊雜比(signal-to-noise ratio, SNR)選擇合適的相位鑑別器，以達到高精確度的相位檢測。在低及高訊雜比的環境中，反正切函數相位鑑別器(arctangent phase discriminator)以及雜訊補償數位相位鑑別器(noise-balanced digital phase discriminator)分別可以精確地估測載波相位，但對於中等訊雜比的應用，兩者皆有估計偏移(bias)的問題。因此，本論文提出訊雜比輔助相位鑑別器(SNR-aided phase discriminator)，以解決中等訊雜比的相位檢測問題。然而，許多實際的應用無法提供訊雜比的資訊，因此我們進一步將訊雜比輔助相位鑑別器發展成同時估測相位及訊雜比的演算法。另一方面，本論文提出一個高運算效率的碼相位(code phase)擷取方法，稱為相位同步擷取法(phase coherence acquisition, PCA)。我們利用複數相量(complex phasor)擷取虛擬隨機序列(PN sequence)的碼相位，其中輸入及本地序列會先分群，接著將分群序列映射到複數相量以提升抗雜訊能力。由於相位同步擷取法主要利用複數相量之間的相位差，所以不需要複數乘法的運算，因此相位同步擷取法所需的運算量遠低於習知的快速傅立葉轉換方法。最後，本論文更進一步發展多層相位同步擷取法(multi-layer PCA)，以得到更強的抗雜訊能力。

# One-bit High-Accuracy Carrier Phase Estimation and Computationally-Efficient Code Phase Acquisition

Student: Wan-Hsin Hsieh

Advisor: Dr. Ming-Seng Kao

Institute of Communication Engineering  
College of Electrical and Computer Engineering  
National Chiao Tung University

## ABSTRACT

In the dissertation, we first investigate the high-accuracy one-bit carrier phase estimation. Signal-to-noise ratio (SNR) is utilized to select the proper phase discriminator to achieve high accuracy. The traditional arctangent phase discriminator (APD) and the noise-balanced digital phase discriminator (NB-DPD) can obtain accurate carrier phase for low and high SNR, respectively, but both algorithms have estimation bias in moderate SNR. Therefore, the SNR-aided phase discriminator (SNRaPD) is proposed to obtain the accurate phase. Since the SNR information may be unavailable in many applications, we further extend the algorithm of SNRaPD to jointly estimate the phase and SNR. On the other hand, we propose a computationally efficient method, termed Phase Coherence Acquisition (PCA), for PN sequence acquisition by using complex phasors. In order to combat noise, the input and local sequences are partitioned and mapped into complex phasors in PCA. The phase differences between pairs of phasors are then utilized for code phase acquisition, and thus complex multiplications are avoided. The computation load of PCA is much less than that of the conventional fast Fourier Transform (FFT) method. Finally, the multi-layer PCA is developed to enhance noise-robustness.

## Acknowledgements

I wish to express my deepest gratitude to my advisor, Professor Ming-Seng Kao, for his kind guidance and assistance during my pursuit of my PhD degree. In addition to the inspiration for the subject matter and enthusiasm related to academic research, he also taught me a lot about life so that I will have an optimistic attitude toward every type of difficulty. It has been a great honor for me to work under his supervision. I am also deeply grateful to Dr. Chieh-Fu Chang, for his guidance on the presentation and publication of research results. His critical advices made the results more solid and convincing. He is also a great tutor who has guided me in the spirit of academic research. Without the invaluable support from Prof. Ming-Seng Kao and Dr. Chieh-Fu Chang, this work could not have been done.

Special thanks go to my laboratory colleagues and friends, Dr. Shu-Tsung Kuo, Dr. Fan-Shuo Tseng, Mr. Ching-Hui Lin (pylon), Mr. Hao-Tang Shih (archer), Mr. Chia-Feng Chang (dream), Mr. Shih-Wei Yeh (malaymo) and Mr. Wei-Chiang Chen for their encouragement and friendship during my study at NCTU. I would also like to thank all the friends in the NCTU Aboriginal club. They introduced me to a vivid and delightful life at NCTU.

I also thank Dr. Men-Tzung Lo for the opportunity to participate in his research projects. I learned a lot about biomedical signal processing under his guidance, for which also broadened my horizons on “signal processing”.

Finally, I greatly appreciate the encouragement and love of my parents, my parents-in-law and my wife, Waan-Rur Lu. Their warm consideration and understanding have accompanied me through this long journey.

# Contents

<b>Chinese Abstract</b> .....	I
<b>English Abstract</b> .....	II
<b>Acknowledgement</b> .....	III
<b>Contents</b> .....	IV
<b>List of Figures</b> .....	VI
<b>List of Tables</b> .....	VII
<b>List of Acronyms</b> .....	VII

## Chapter 1

### Introduction

1.1 Review of Phase Estimation Method.....	1
1.2 Review of Code Phase Acquisition Method.....	2
1.3 Organization of Dissertation.....	4

## Chapter 2

### One-Bit Accurate Phase Estimation

2.1 System Model .....	5
2.2 Accurate One-Bit Phase Discriminator.....	11
2.2.1 High-SNR.....	12
2.2.2 Low-SNR.....	13
2.2.3 Moderate-SNR.....	18
2.3 SNR-Aided Phase Discriminator.....	20
2.3.1 Proposed method .....	20
2.3.2 Cramér-Rao bound .....	23
2.3.3 Stop criterion .....	25
2.3.4 Range of application.....	27
2.4 Summary.....	30

## Chapter 3

### Joint One-Bit Phase and SNR Estimation

3.1 System Model .....	31
3.2 Nonlinear Least-Square Algorithm.....	34
3.3 Simulation and Discussion .....	36
3.3.1 Monte Carlo simulation.....	36
3.3.2 Range of application.....	40
3.4 Summary.....	42

## **Chapter 4**

### **Code Phase Coherence Acquisition Method**

4.1 Motivation.....	43
4.2 Acquisition by Phasor .....	44
4.3 Phase Coherence Acquisition Algorithm.....	47
4.3.1 Segmentation .....	47
4.3.2 Acquisition by Phase .....	49
4.3.3 Multi-layer PCA .....	52
4.3.4 Error detection capability .....	55
4.4 Performance of PCA.....	57
4.5 Computation of PCA .....	66
4.6 Summary.....	67

## **Chapter 5**

### **Conclusions and Future Work**

.....	69
-------	----

### **Reference**

.....	71
-------	----

### **Appendix**

A. Derivation of mean and variance of I-Q channel outputs.....	75
B. Power series representation of mean and variance of I-Q channel outputs ..	76
C. Magnitude and phase distribution of $G_m$ .....	78

## List of Figures

<b>Fig. 2.1</b>	System structure of one-bit SDR.....	6
<b>Fig. 2.2</b>	Relationship between the mean values of the I-Q channel outputs (first quadrant).....	11
<b>Fig. 2.3</b>	Simulated results of NB-DPD regarding SNR.....	13
<b>Fig. 2.4</b>	Geometric representation of performance of APD on the I-Q plane.....	14
<b>Fig. 2.5</b>	Analytical and simulated results of APD regarding SNR.....	17
<b>Fig. 2.6</b>	Asymptotic performance of NB-DPD and APD regarding SNR.....	19
<b>Fig. 2.7</b>	Performance of SNRaPD regarding SNR.....	22
<b>Fig. 2.8</b>	MSE of SNRaPD (markers) and AvCRB (solid lines).....	24
<b>Fig. 2.9</b>	Comparison between RMSE of SNRaPD and that of NB-DPD and APD.....	28
<b>Fig. 3.1</b>	RMSE of phase estimation.....	38
<b>Fig. 3.2</b>	Normalized RMSE of SNR estimation.....	38
<b>Fig. 3.3</b>	Mean I-Q correlation outputs for SNR between 0 to 15dB in 1dB step.....	39
<b>Fig. 4.1</b>	Schematic plot of the phase resolution for phasors on the complex domain.....	46
<b>Fig. 4.2</b>	Schematic plot of two layer segmentation: (a) segmentation in the 1 <sup>st</sup> -layer; (b) segmentation of segment $\mathbf{A}_0$ in the 2 <sup>nd</sup> -layer.....	54
<b>Fig. 4.3</b>	Flow chart of the process of two-layer PCA.....	56
<b>Fig. 4.4</b>	Correct probability of $d_1$ in the 1 <sup>st</sup> -layer of PCA.....	60
<b>Fig. 4.5</b>	Joint correct probability of $d_1$ and $c_1$ in the 1 <sup>st</sup> -layer of PCA.....	61
<b>Fig. 4.6</b>	STD of $\hat{c}_1$ in the 1 <sup>st</sup> -layer of PCA when $\hat{d}_1 = d_1$ .....	62
<b>Fig. 4.7</b>	Correct probability of $d_2$ in the 2 <sup>nd</sup> -layer of PCA.....	65
<b>Fig. 4.8</b>	Joint correct probability of $d_2$ and $c_2$ in the 2 <sup>nd</sup> -layer of PCA.....	65
<b>Fig. 4.9</b>	STD of $\hat{c}_2$ in the 2 <sup>nd</sup> -layer of PCA when $\hat{d}_2 = d_2$ .....	66

## List of Tables

<b>Table 4.1</b>	Computations of the two-layer PCA and the FFT-based method.....67
------------------	---

## List of Acronyms

<b>ADC</b>	analog-to-digital conversion
<b>AGC</b>	automatic gain control
<b>APD</b>	arctangent phase discriminator
<b>AWGN</b>	additive white Gaussian noise
<b>C/A</b>	coarse/acquisition
<b>CRB</b>	Cramér-Rao bound
<b>DPD</b>	digital phase discriminator
<b>DSP</b>	digital signal processing
<b>FFT</b>	fast Fourier transform
<b>GNSS</b>	global navigation satellite system
<b>I-Q</b>	inphase-quadrature
<b>LEO</b>	low Earth orbit satellite
<b>LLN</b>	law of large numbers
<b>MLE</b>	maximum-likelihood estimation
<b>MSE</b>	mean-squared error
<b>NB-DPD</b>	noise-balanced digital phase discriminator
<b>PCA</b>	phase coherence acquisition
<b>PN</b>	pseudo-random
<b>POD</b>	precise orbit determination
<b>RMSE</b>	root mean-squared error
<b>SDR</b>	software-defined receiver
<b>SNR</b>	signal-to-noise power ratio
<b>SNRaPD</b>	SNR-aided phase discriminator
<b>STD</b>	standard deviation
<b>TEC</b>	total electron content
<b>WT</b>	Walsh transform



# Chapter 1

## Introduction

Carrier phase estimation and code phase acquisition are essential in various applications, such as the spread-spectrum system and the global navigation satellite system (GNSS) [1-2]. In modern applications, carrier phase estimation and code phase acquisition may be implemented by means of the software-defined receiver (SDR) so as to obtain more capability and flexibility in signal processing [3]. In SDR, more analog-to-digital conversion (ADC) bits are generally desired so as to avoid significant quantization error. For example, power degradation is at least 2dB for one-bit ADC [4-5]. On the other hand, because of the benefits of the one-bit scenario, such as efficient bitwise processing and the avoidance of automatic gain control (AGC), the one-bit ADC has still induced wide interest [6-11]. In this dissertation, we investigate the high-accuracy one-bit carrier phase estimation for the tracking process and propose a multiplication-free code phase acquisition method that uses much less computation than the FFT-based method for SDR.

### 1.1 Review of Phase Estimation Method

For the conventional phase estimation of a sinusoidal carrier, the arctangent phase discriminator (APD) is widely adopted since it achieves maximum-likelihood estimation (MLE) in additive white Gaussian noise (AWGN) [12, page 167]. With infinite ADC bits, the APD attains MLE irrespective of what the signal-to-noise ratio (SNR) is. However, this is not the case for realistic phase discriminators that have finite precision using a few-bit ADC, especially those with one-bit ADC. The problem of parameter estimation for a single sinusoid was previously investigated in [13-16]. In [16], Cramér-Rao bound (CRB) of one-bit quantization could be derived under the assumption of independence between quantized

samples. The effects of one-bit sampling and quantization were also discussed. Unfortunately, due to the lack of a closed form of probability mass function of samples [16, Eq. (10)], the derivation of MLE of the sinusoidal carrier is intractable. Next, the dithering techniques were used to improve the estimation performance. In [17] and [18], the asymptotic bias of one-bit quantized mean estimation problems was addressed. Other relevant studies fell in the field of the limiter phase detector [19][20, Chap. 10], which utilizes a limiter to prevent overload of the received signal. For high SNR, the asymptotic phase estimation bias of APD had been mentioned and an improved phase discriminator, called digital phase discriminator (DPD), was proposed in [21]. The DPD achieves much higher asymptotic accuracy than that of the traditional APD. However, the DPD does not perform well in low SNR environments due to its sensitivity to noise. A modified DPD, termed the noise-balanced digital phase discriminator (NB-DPD), incorporates the summation of noisy samples in phase estimation leading to an improved noise performance [22].

## **1.2 Review of Code Phase Acquisition Method**

Pseudo-random (PN) sequence acquisition is widely used in various applications. For example, the acquisition is implemented to search for the correct code phase so as to identify the transmitter in spread spectrum communications. Because of the limitations associated with the hardware techniques, conventional code acquisition could only be achieved by serially examining the possible code phase of the input sequence in the time-domain [23-24]. However, the time required for acquisition would be so long that limits the application of longer PN sequence in practice. With the improvements in hardware implementation, the parallel acquisition scheme, which employs a large amount of correlation circuits to examine all the code phases concurrently was then devised to significantly reduce the acquisition time [25]. A hybrid scheme had also been proposed to provide a compromise between the acquisition speed and hardware complexity for the serial and parallel schemes, respectively

[26]. In addition to the hybrid scheme, the acquisition schemes can employ auxiliary subsystems, such as an auxiliary signal generator and a phase estimator, to attain reasonable speed and complexity as well [27-28]. Owing to the recent development of digital signal processing (DSP) for software receivers, the exhaustive computation of the direct serial search between two sequences can be mitigated by fast Fourier transform (FFT) to reduce the computation by utilizing convolution theorem [29-31], which states that the convolution of two sequences can be derived from the pointwise product of corresponding Fourier transforms (i. e.,  $x[n] \otimes y[n] \xrightarrow{F} X(\omega) \cdot Y(\omega)$ , where  $\otimes$  denotes convolution and  $F$  represents Fourier transform). The theorem that facilitates FFT can be used in the PN sequence acquisition to efficiently search the code phase [32-33]. To further reduce the computational burden of FFT-based acquisition, the efficient split-radix FFT techniques rather than conventional radix-2 FFT could be used for transformation so that the number of multiplications, addition and memory access can thus be reduced [34]. In addition, by the fact that the more FFT points, the more computations are required, the acquisition with fewer FFT points, which is cheaper, was performed on the coarse/acquisition (C/A) codes with averaging up several samples of a code chip [35]. Instead of averaging the samples, the FFT points could also be reduced by removing the insignificant points. By examining the spectrum of input and local C/A sequences, it is found that most of the energy is contained in the low-frequency half of the spectrum. Hence the other half of the spectrum, which is comprised of very little information could be eliminated and thus the number points for FFT-based acquisition were decreased [36]. On the other hand, the multiplication operation in the FFT method generally requires many computational resources. Hence, a substitute method employing Walsh transform (WT) was implemented to calculate the convolution without the need for multiplications [37-38]. Specifically, as compared to the FFT-based method, the WT-based method requires fewer additions and no multiplications, but additional permutations of the input samples and the output results are needed.

### 1.3 Organization of Dissertation

The dissertation is organized as follows. In Chapter 2, we investigate the one-bit high-accuracy phase discriminator for three SNR ranges: low SNR, high SNR and moderate SNR. Unlike traditional approaches, this approach first distinguishes which SNR range an application falls into, and this SNR information is then utilized to select a proper phase discriminator for achieving high accuracy. For low-SNR applications, traditional APD is adopted. For high-SNR applications, NB-DPD is utilized to improve accuracy. Between them, for moderate-SNR applications, a novel SNR-aided phase discriminator (SNRaPD) developed using the nonlinear least-square method is proposed.

However, since the SNR information may be unavailable in many applications, the SNR should also be estimated so as to attain the accurate phase estimation. Hence, a nonlinear least-square algorithm for deriving the SNRaPD is further extended to jointly estimate the phase and SNR estimation in Chapter 3. Because of the avoidance of AGC by using one-bit ADC, the joint phase and SNR estimation method can accommodate signals with high dynamic range. Potential applications for the spaceborne measurements are also discussed.

Next, we propose a novel method, termed the Phase Coherence Acquisition (PCA), to search for the cross-correlation peak for pseudo-random (PN) sequence acquisition by using complex phasors in Chapter 4. The PCA requires only complex additions in the order of  $N$ , the length of the sequence, whereas the conventional method utilizing FFT requires complex multiplications and additions, both in the order of  $N \log_2 N$ . Specifically, the phase differences between pairs of input and local phasors are utilized for acquisition, and thus complex multiplications are avoided. The significant reduction of computational loads makes the PCA an attractive method, especially when the sequence length of  $N$  becomes extremely large which becomes intractable for the FFT-based acquisition. Finally, the conclusion of the dissertation is made in Chapter 5.

# Chapter 2

## One-Bit Accurate Phase Estimation

In this chapter, we clarify the accuracy of one-bit phase discriminators regarding SNR, such as the accuracy of APD and NB-DPD in low and high SNR, respectively. Moreover, we design an SNRaPD that utilizes the SNR information in phase estimation to enhance ultimate accuracy in moderate SNR. A high-accuracy phase estimation is critical to the successful tracking of carrier signals. In this study, the traditional inphase-quadrature (I-Q) structure using one-bit ADC is studied first and the SNR-dependent mean value of the I-Q channel output is derived. Note that, because the frequency of the received carrier can be captured by the acquisition process or a frequency locked loop [2], the frequency shift between input and local carrier can be regarded as a part of phase shift in steady-state tracking. Hence, the influence of frequency shift is omitted and the AWGN channel is considered in our analysis. Next, phase estimation with APD and NB-DPD are addressed. The SNRaPD is then introduced and the improvement in accuracy is simulated and compared with the average Cramér-Rao bound (CRB). In addition, an adequate stop criterion and the range of applications regarding the SNR of SNRaPD are also discussed. The high-accuracy phase information obtained with the proposed algorithm can potentially be applied to spaceborne measurements in GNSS and beacon receivers when the ambient SNR falls within the “moderate SNR” range and the multipath effect is mitigated.

### 2.1 System Model

The system model for phase estimation of sinusoidal carrier in the one-bit SDR is shown Fig. 2.1. The received signal is denoted by

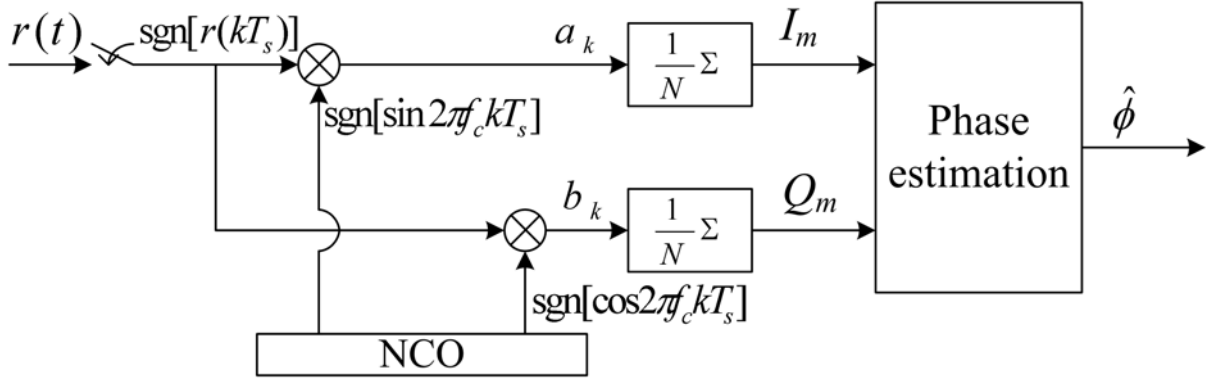


Fig. 2.1. System structure of one-bit SDR.

$$r(t) = \sin(2\pi f_c t + \phi) + \nu(t) \quad (2.1)$$

where  $f_c$  is the carrier frequency,  $\phi$  is an unknown phase, and  $\nu(t)$  is the AWGN.

For phase estimation, the output frequency of the numerically controlled oscillator (NCO) is assumed equal to the incoming carrier frequency. Let  $T_s$  be the sampling period. The discrete-time one-bit quantized  $r(t)$  is given by

$$r[k] = \text{sgn}[r(kT_s)] = \text{sgn}[\sin(2\pi f_c kT_s + \phi) + \nu(kT_s)] \quad (2.2)$$

where

$$\text{sgn}[x] = \begin{cases} 1 & \text{if } x \geq 0 \\ -1 & \text{if } x < 0. \end{cases}$$

In addition, let the sampling frequency be  $f_s = 1/T_s$ . We denote

$$\frac{f_c}{f_s} = h + \frac{q}{p} \quad (2.3)$$

where  $h$  is the greatest integer less than or equal to  $f_c/f_s$ , and  $p$  and  $q$  are mutually prime integers.

The mixer output of the inphase channel is given by

$$\begin{aligned} a_k &= \text{sgn}[r(kT_s)] \cdot \text{sgn}[\sin 2\pi f_c kT_s] \\ &= \text{sgn}[\sin(\Phi_k + \phi) + v_k] \cdot \text{sgn}[\sin \Phi_k] \end{aligned} \quad (2.4)$$

where  $\Phi_k = 2\pi f_c kT_s$  and  $v_k = v(kT_s)$  is a zero-mean Gaussian random variable with variance  $\sigma^2$ .

Consider  $p$  samples at  $t = kT_s$ ,  $k = 0, 1, 2, \dots, p-1$ . The normalized I-Q channel outputs are denoted by

$$I_p = \frac{1}{p} \sum_{k=0}^{p-1} \text{sgn}[\sin(\Phi_k + \phi) + v_k] \cdot \text{sgn}[\sin \Phi_k] \quad (2.5a)$$

$$Q_p = \frac{1}{p} \sum_{k=0}^{p-1} \text{sgn}[\sin(\Phi_k + \phi) + v_k] \cdot \text{sgn}[\cos \Phi_k]. \quad (2.5b)$$

It can be proved that the samples of phases  $\{\Phi_0, \Phi_1, \dots, \Phi_{p-1}\}$  are uniformly distributed over  $[0, 2\pi)$  with a separation of  $2\pi/p$  between neighboring  $\Phi_i$ 's [21]. Note that when we mention that  $p$  is “sufficiently” large later, it means that  $2\pi/p$  is significantly smaller than the accuracy required for the estimation. According to Appendix A, the mean values and variances of the I-Q channel outputs are given by

$$\mu_{I_p} = \frac{1}{p} \left[ \sum_{\Phi_k \in [0, \pi)} (1 - 2P_k) + \sum_{\Phi_k \in [\pi, 2\pi)} (2P_k - 1) \right] \quad (2.6a)$$

$$\mu_{Q_p} = \frac{1}{p} \left[ \sum_{\Phi_k \in [0, \pi/2) \cup [3\pi/2, 2\pi)} (1 - 2P_k) + \sum_{\Phi_k \in [\pi/2, 3\pi/2)} (2P_k - 1) \right] \quad (2.6b)$$

$$\sigma_{I_p}^2 = \sigma_{Q_p}^2 = \frac{4}{p^2} \sum_{k=0}^{p-1} P_k - P_k^2 \quad (2.7)$$

where

$$P_k = Q\left(\frac{\sin(\Phi_k + \phi)}{\sigma}\right)$$

$$Q(x) = \frac{1}{\sqrt{2\pi}} \int_x^{\infty} \exp\left(-\frac{z^2}{2}\right) dz.$$

Note that the range of summation is defined according to the value of  $\Phi_k$  in Eq. (2.6), and  $P_k$  is a function of  $\Phi_k$ . In Eq. (2.7), the variance of the one-bit quantized I-Q outputs consists of the effect of channel noise and quantization noise. Since  $\{\Phi_0, \Phi_1, \dots, \Phi_{p-1}\}$  are uniformly distributed over  $[0, 2\pi)$ , the mean value of I-channel output in Eq. (2.6a) can be further derived by

$$\begin{aligned} \mu_{I_p} &= \frac{1}{p} \left[ \frac{p}{2} - \sum_{\Phi_k \in [0, \pi)} 2Q\left(\frac{\sin(\Phi_k + \phi)}{\sigma}\right) + \sum_{\Phi_k \in [\pi, 2\pi)} 2Q\left(\frac{\sin(\Phi_k + \phi)}{\sigma}\right) - \frac{p}{2} \right] \\ &= \frac{1}{p} \left[ \sum_{\Phi_k \in [\pi, 2\pi)} 2Q\left(\frac{\sin(\Phi_k + \phi)}{\sigma}\right) - \sum_{\Phi_k \in [0, \pi)} 2Q\left(\frac{\sin(\Phi_k + \phi)}{\sigma}\right) \right]. \end{aligned} \quad (2.8)$$

From Eq. (2.1), the SNR of the sinusoidal signal is given by

$$\text{SNR} = \frac{1}{2\sigma^2}. \quad (2.9)$$

Eq. (2.8) can then be written as



$$\mu_{I_p} = \frac{1}{P} \left[ \sum_{\Phi_k \in [\pi, 2\pi)} 2Q(\gamma \sin(\Phi_k + \phi)) - \sum_{\Phi_k \in [0, \pi)} 2Q(\gamma \sin(\Phi_k + \phi)) \right] \quad (2.10)$$

where  $\gamma = \sqrt{2\text{SNR}}$ .

Suppose we choose  $f_s$  such that  $p$  is sufficiently large in Eq. (2.3). According to Appendix B, the mean value of I-channel output of Eq. (2.10) can be represented as a power series, which is given by

$$\mu_{I_p} = A \sum_{m=0}^{\infty} \frac{\gamma^{2m+1}}{m! 2^{3m} (2m+1)} \left[ \sum_{l=0}^m (-1)^l \binom{2m+1}{l} \frac{\cos(2m+1-2l)\phi}{2m+1-2l} \right] \quad (2.11)$$

where  $A = \frac{4}{\sqrt{2\pi^{3/2}}}$ .

Similarly, the mean value of Q-channel output of Eq. (2.6b) is denoted by

$$\mu_{Q_p} = \frac{1}{P} \left[ \sum_{\Phi_k \in [0, \pi/2) \cup [3\pi/2, 2\pi)} -2Q(\gamma \sin(\Phi_k + \phi)) + \sum_{\Phi_k \in [\pi/2, 3\pi/2)} 2Q(\gamma \sin(\Phi_k + \phi)) \right]. \quad (2.12)$$

By a similar derivation of Eq. (2.11), the power series representation of  $\mu_{Q_p}$  is given by

$$\mu_{Q_p} = A \sum_{m=0}^{\infty} \frac{(-1)^m \gamma^{2m+1}}{m! 2^{3m} (2m+1)} \left[ \sum_{l=0}^m \binom{2m+1}{l} \frac{\sin(2m+1-2l)\phi}{2m+1-2l} \right]. \quad (2.13)$$

In addition, according to Appendix B, the power series of the variances of the I-Q channel outputs of Eq. (2.7) are represented by

$$\begin{aligned}
\sigma_{I_p}^2 &= \sigma_{Q_p}^2 \\
&= \frac{1}{p} - \frac{2}{p\pi} \left[ \sum_{m=0}^{\infty} \binom{4m+2}{2m+1} \frac{\gamma^{4m+2}}{(m!2^{3m+1}(2m+1))^2} \right. \\
&\quad \left. + 2 \sum_{x=0}^{\infty} \sum_{y=x+1}^{\infty} \binom{2x+2y+2}{x+y+1} \frac{(-1)^{x+y} \gamma^{2(x+y)+2}}{x!y!2^{3(x+y)+2}(2x+1)(2y+1)} \right].
\end{aligned} \tag{2.14}$$

The above results are obtained for  $p$  samples. When the mean values and variances are generalized to  $N = mp$  samples, where  $m$  is an integer, the normalized I-Q channel outputs are given by

$$I_m = \frac{1}{N} \sum_k \text{sgn}[\sin(\Phi_k + \phi) + v_k] \cdot \text{sgn}[\sin \Phi_k] \tag{2.15a}$$

$$Q_m = \frac{1}{N} \sum_k \text{sgn}[\sin(\Phi_k + \phi) + v_k] \cdot \text{sgn}[\cos \Phi_k]. \tag{2.15b}$$

The mean values of the I-Q channel outputs are the same as Eq. (2.11) and Eq. (2.13), respectively. The variance can be expressed as

$$\begin{aligned}
\sigma_I^2 &= \sigma_Q^2 \\
&= \frac{1}{N} - \frac{2}{N\pi} \left[ \sum_{m=0}^{\infty} \binom{4m+2}{2m+1} \frac{\gamma^{4m+2}}{(m!2^{3m+1}(2m+1))^2} \right. \\
&\quad \left. + 2 \sum_{x=0}^{\infty} \sum_{y=x+1}^{\infty} \binom{2x+2y+2}{x+y+1} \frac{(-1)^{x+y} \gamma^{2(x+y)+2}}{x!y!2^{3(x+y)+2}(2x+1)(2y+1)} \right].
\end{aligned} \tag{2.16}$$

The relationship between the mean values of the I-Q channel outputs is shown in Fig. 2.2. Here, only the relationship in the 1st quadrant is illustrated because of the symmetry of the trigonometric function. As can be seen in Fig. 2.2, the relationship between the I-Q channel outputs varies with the SNR.

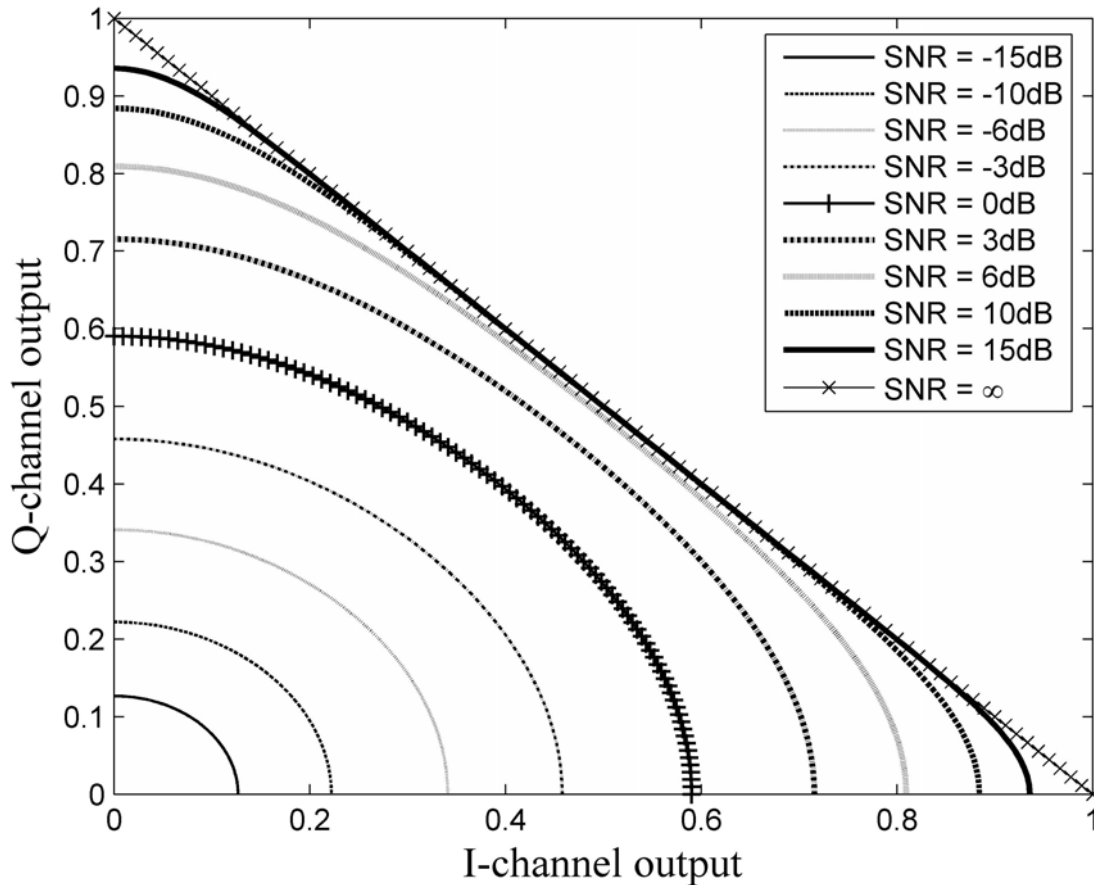


Fig. 2.2. Relationship between the mean values of the I-Q channel outputs (first quadrant).

The relationship approximates a circle when the SNR is low, but deviates from a circle with increasing SNR. When  $\text{SNR} \rightarrow \infty$ , the relationship becomes a straight line. Since the phase is estimated from the I-Q channel outputs in Fig. 2.1, the phase estimation should be adjusted according to the SNR to achieve high accuracy. In the following sections, accurate phase estimations regarding SNR are introduced. Note that, in order to evaluate the achievable phase accuracy, the assumption of zero frequency offset is inherently applied to the following analyses and simulations.

## 2.2 Accurate One-Bit Phase Discriminator

In this section, we introduce phase discriminators that have been proposed in the literature, i.e., DPD [21], NB-DPD [22], and APD, for one-bit quantized data and discuss their performance regarding SNR.

### 2.2.1 High-SNR

When  $\text{SNR} \rightarrow \infty$ ,  $v_k$  in Eq. (2.15) can be neglected. Moreover, when the number of samples  $N$  is large, by the law of large numbers (LLN), the I-Q channel outputs, denoted as  $(I_m, Q_m)$ , approximate their mean values, i.e.,  $I_m \rightarrow \mu_I$  and  $Q_m \rightarrow \mu_Q$ . The relationship between the I-Q channel outputs is then denoted by

$$\mu_I + \mu_Q = 1. \quad (2.17)$$

The relationship is a straight line as shown in Fig. 2.2. In this situation, the phase can be estimated by DPD, resulting in higher accuracy than that of APD [21]. Applying the system model of Fig. 2.1 in [21], the phase estimation according to  $(I_m, Q_m)$  is given by

$$\hat{\phi}_{\text{DPD}} = \text{sgn}(Q_m) \frac{\pi}{2} (1 - I_m). \quad (2.18)$$

The mean-squared error (MSE) of DPD will be negligible with a sufficiently large  $N$ .

However, in the high SNR environment, small noise variance still exists in the I-Q channel outputs, and the relationship between the mean I-Q outputs deviates from a straight line as shown in Fig. 2.2. Since DPD is sensitive to noise, the modified DPD, called NB-DPD, is provided to improve phase estimation in this situation. The phase estimated by NB-DPD is given by [22]

$$\hat{\phi}_{\text{NB-DPD}} = \text{sgn}(Q_m) \frac{\pi}{2} \left( 1 - \frac{I_m}{|I_m| + |Q_m|} \right). \quad (2.19)$$

Let the root mean-squared error (RMSE) of NB-DPD be denoted by

$\varepsilon_{\text{NB-DPD}} = \sqrt{E[(\hat{\phi}_{\text{NB-DPD}} - \phi)^2]}$ . Using Monte Carlo simulation methods for 100 trials,  $\varepsilon_{\text{NB-DPD}}$  regarding SNR is shown in Fig. 2.3. As expected,  $\varepsilon_{\text{NB-DPD}}$  decreases with increasing SNR. In addition, it decreases slightly with  $N$  in high SNR. Apparently, the NB-DPD can achieve high phase estimation accuracy in high SNR.

### 2.2.2 Low-SNR

When the SNR is low, we have  $\gamma \ll 1$  in Eq. (2.11) and Eq. (2.13). Thus, the mean values of the I-Q channel outputs are approximated by

$$\mu_I = \frac{4\gamma}{\sqrt{2\pi^{3/2}}} \cos \phi, \quad (2.20a)$$

$$\mu_Q = \frac{4\gamma}{\sqrt{2\pi^{3/2}}} \sin \phi. \quad (2.20b)$$

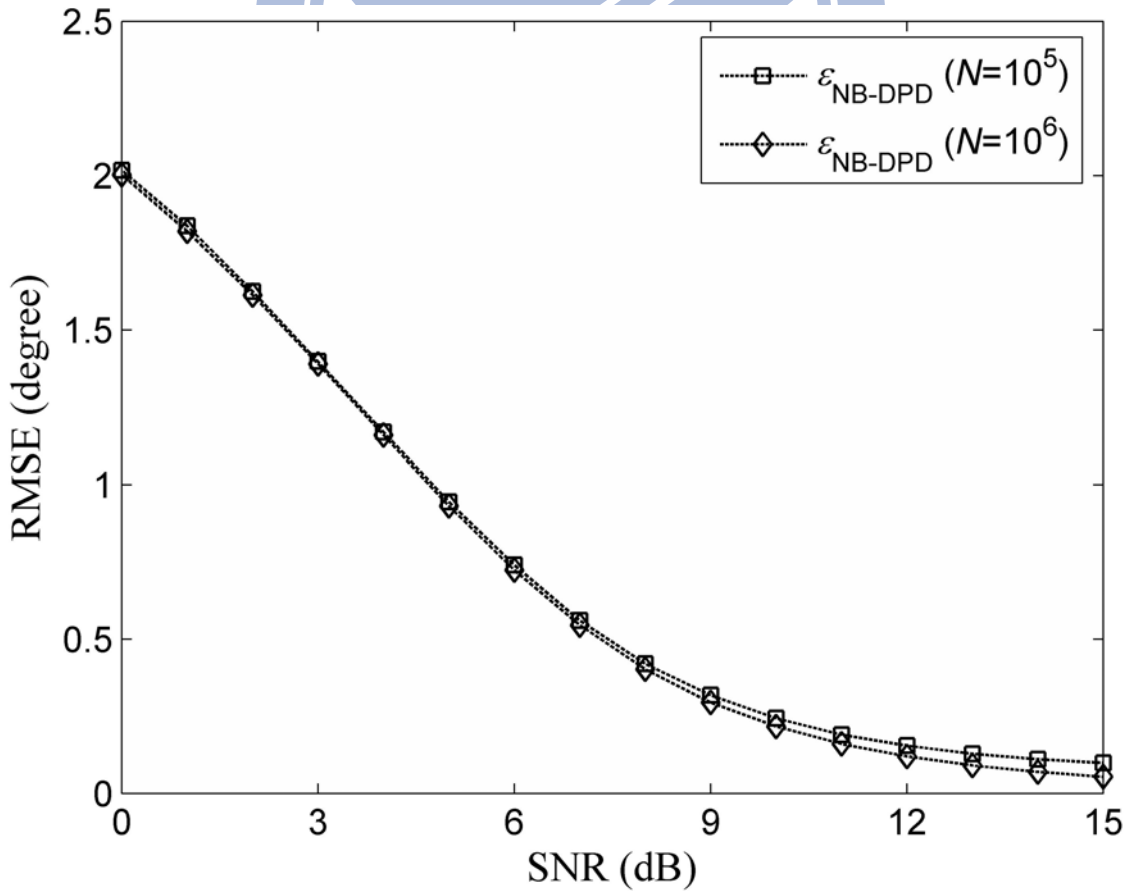


Fig. 2.3. Simulated results of NB-DPD regarding SNR.

This proves the circular relationship of the I-Q channel output in the low SNR environment as shown in Fig. 2.2. The result is also consistent with Pouzet's conclusion, when we consider a limiter as a binary quantizer with an infinite number of samples [19][20, Chap. 10]. Since the mean I-Q channel outputs have an approximately circular relationship, APD is a good choice in low SNR. In addition, the variances of the I-Q channel outputs of Eq. (2.16) are approximated by

$$\begin{aligned}\sigma_I^2 &= \sigma_Q^2 \\ &= \frac{1}{N} \left( 1 - \frac{\gamma^2}{\pi} \right) \\ &\approx \frac{1}{N^2}\end{aligned}\tag{2.21}$$

when the SNR is low.

The performance of APD in low SNR is analyzed using geometry as shown in Fig. 2.4.

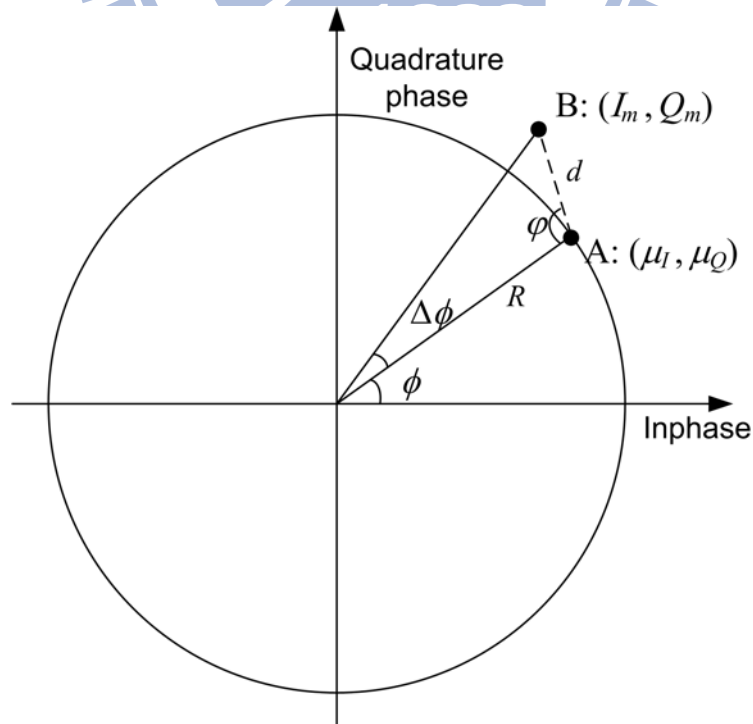


Fig. 2.4. Geometric representation of performance of APD on the I-Q plane.

First, let point A:  $(\mu_I, \mu_Q)$  denote the mean values of the I-Q outputs on a circle with radius  $R$  and polar phase  $\phi$ . According to Eq. (2.20), the radius  $R$  is given by

$$\begin{aligned} R &= \sqrt{\mu_I^2 + \mu_Q^2} \\ &= \frac{4\gamma}{\sqrt{2\pi}^{3/2}} \\ &= \frac{4\sqrt{\text{SNR}}}{\pi^{3/2}}. \end{aligned} \quad (2.22)$$

Next, let B:  $(I_m, Q_m)$  be the measured I-Q channel outputs. The distance between A and B is denoted by

$$d = \sqrt{(I_m - \mu_I)^2 + (Q_m - \mu_Q)^2}. \quad (2.23)$$

The sinusoidal carrier phase estimated from  $(I_m, Q_m)$  with APD is given by

$$\hat{\phi}_{\text{APD}} = \text{atan2}\left(\frac{Q_m}{I_m}\right) = \phi + \Delta\phi \quad (2.24)$$

where  $\text{atan2}(x)$  denotes the arctangent-2 function and  $\Delta\phi$  is the phase estimation error.

Without loss of generality, let  $\Delta\phi \geq 0$ . From the law of sines, we have

$$\frac{d}{\sin \Delta\phi} = \frac{R}{\sin(\pi - \phi - \Delta\phi)}. \quad (2.25)$$

Assume  $\Delta\phi \ll 1$ . Then  $\sin \Delta\phi \approx \Delta\phi$ , and  $\sin(\pi - \phi - \Delta\phi) \approx \sin(\pi - \phi)$ . Eq. (2.25) is approximated by

$$\Delta\phi \approx \frac{d}{R} \sin(\pi - \varphi). \quad (2.26)$$

Suppose  $\varphi$  is uniformly distributed over  $[0, \pi)$ . For a fixed  $d$ , the expected value of  $\Delta\phi^2$  with respect to  $\varphi$  is denoted by

$$\begin{aligned} E_{\varphi}[\Delta\phi^2] &= \frac{1}{\pi} \int_0^{\pi} \frac{d^2}{R^2} \sin^2(\pi - \varphi) d\varphi \\ &= \frac{d^2}{2R^2}. \end{aligned} \quad (2.27)$$

Assume  $d$  and  $\varphi$  are mutually independent. According to the definition of variance and Eq. (2.21), the expected value of  $d^2$  is given by

$$\begin{aligned} E_d[d^2] &= E[(I_m - \mu_I)^2 + (Q_m - \mu_Q)^2] \\ &= \sigma_I^2 + \sigma_Q^2 \\ &= \frac{2}{N}. \end{aligned} \quad (2.28)$$

From Eq. (2.27) and Eq. (2.28), the MSE of phase estimation is denoted by

$$\begin{aligned} E_d[E_{\varphi}[\Delta\phi^2]] &= \frac{E_d[d^2]}{2R^2} \\ &= \frac{1}{NR^2} \\ &= \frac{\pi^3}{16N \cdot \text{SNR}}. \end{aligned} \quad (2.29)$$

In addition, the RMSE of APD is given by



$$\begin{aligned}
\varepsilon_{\text{APD}} &= \sqrt{E_d [E_\varphi [\Delta\phi^2]]} \\
&= \frac{\pi^{3/2}}{4\sqrt{N \cdot \text{SNR}}} \quad (\text{radian}) \\
&= \frac{80^\circ}{\sqrt{N \cdot \text{SNR}}}. \quad (\text{degree})
\end{aligned} \tag{2.30}$$

From Eq. (2.30),  $\varepsilon_{\text{APD}}$  is inversely proportional to the square root of the product of SNR and  $N$ . The analytical and simulated  $\varepsilon_{\text{APD}}$  are shown in Fig. 2.5. The simulated results are obtained by Monte Carlo simulation for 100 trials. From Fig. 2.5, the simulated results approach the analytical values in low SNR. Note that the analytical  $\varepsilon_{\text{APD}}$  is provided in part since the result is valid only when low SNR is assumed. From Fig. 2.5, a minimal  $\varepsilon_{\text{APD}}$  exists at the specific SNR in the simulated cases. Below that SNR,  $\varepsilon_{\text{APD}}$  increases with decreasing SNR, whereas  $\varepsilon_{\text{APD}}$  increases when the SNR is above that SNR.

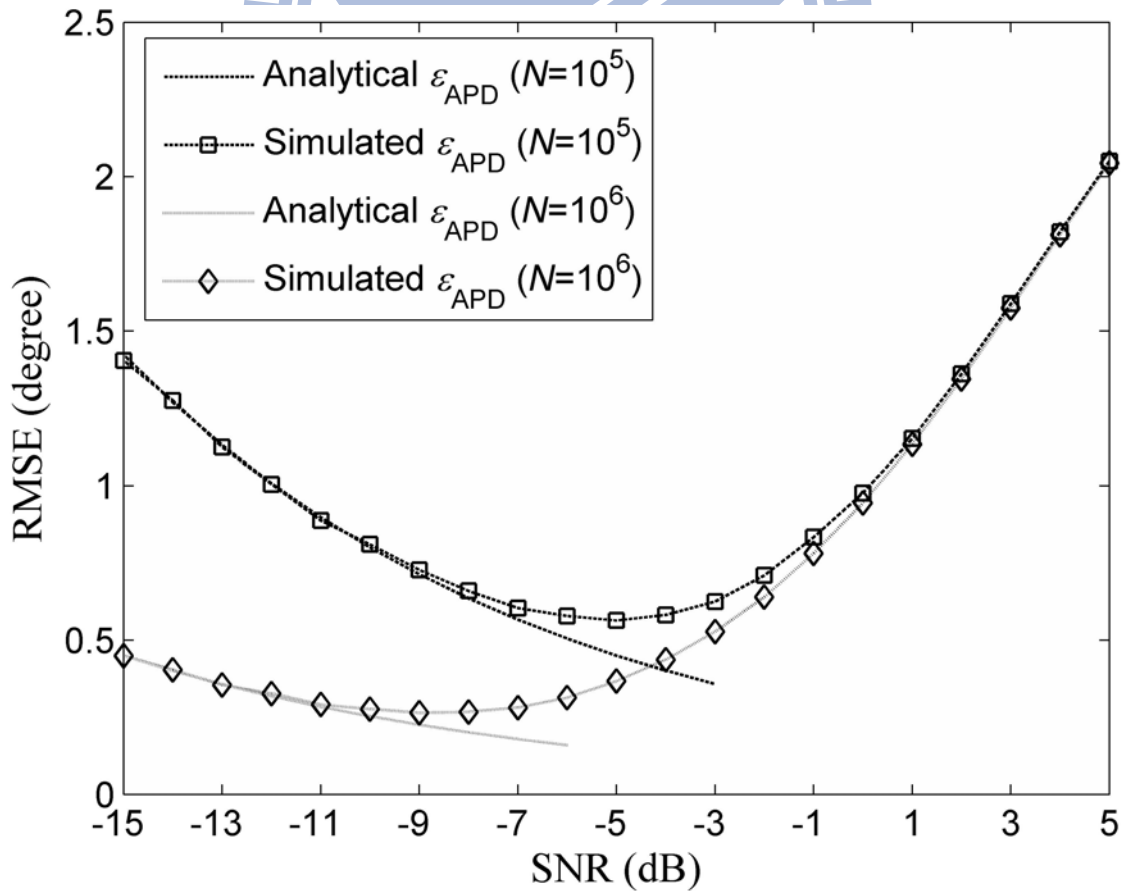


Fig. 2.5. Analytical and simulated results of APD regarding SNR.

According to Fig. 2.2, since the relationship of the mean values of the I-Q outputs deviates from a circle with increasing SNR, the increase in  $\varepsilon_{\text{APD}}$  is due to the estimation bias of the APD, which will be shown below.

### 2.2.3 Moderate-SNR

Between the high SNR and the low SNR, the relationship between the mean I-Q outputs is complicated, as indicated in Fig. 2.2. The estimation bias of NB-DPD and APD is examined by means of the asymptotic performance. Suppose  $N$  is sufficiently large. By LLN, the I-Q channel outputs of Eq. (2.15) approach their mean values, i.e.,  $I_m \rightarrow \mu_I$  and  $Q_m \rightarrow \mu_Q$ . The asymptotic performance of NB-DPD and APD are defined by

$$\hat{\phi}_{\text{AsNB-DPD}}^{\Delta} = \text{sgn}(\mu_Q) \frac{\pi}{2} \left( 1 - \frac{\mu_I}{|\mu_I| + |\mu_Q|} \right), \quad (2.31)$$

$$\hat{\phi}_{\text{AsAPD}}^{\Delta} = \text{atan2} \left( \frac{\mu_Q}{\mu_I} \right). \quad (2.32)$$

The corresponding squared phase errors are given by  $e_{\text{ND}} = (\hat{\phi}_{\text{AsNB-DPD}} - \phi)^2$  and  $e_{\text{A}} = (\hat{\phi}_{\text{AsAPD}} - \phi)^2$ , respectively. We further denote the asymptotic estimation error by

$$\varepsilon_{\text{AsNB-DPD}} = (\bar{e}_{\text{ND}})^{1/2} \quad (2.33)$$

and

$$\varepsilon_{\text{AsAPD}} = (\bar{e}_{\text{A}})^{1/2}. \quad (2.34)$$

Note that the averaged values of  $e_{\text{ND}}$  and  $e_{\text{A}}$ , i.e.,  $\bar{e}_{\text{ND}}$  and  $\bar{e}_{\text{A}}$ , are used in Eq. (2.33) and Eq. (2.34), since they are functions of  $\phi$ . The  $\varepsilon_{\text{AsNB-DPD}}$  and  $\varepsilon_{\text{AsAPD}}$  regarding SNR are shown in Fig. 2.6. From Fig. 2.6,  $\varepsilon_{\text{AsNB-DPD}}$  and  $\varepsilon_{\text{AsAPD}}$  are small in high and low SNR, respectively. That is,  $\varepsilon_{\text{AsNB-DPD}} < 0.1$  degrees if  $\text{SNR} > 12$  dB, and  $\varepsilon_{\text{AsAPD}} < 0.1$  degrees when  $\text{SNR} < -10$  dB. However,  $\varepsilon_{\text{AsNB-DPD}}$  becomes significant when the SNR decreases whereas  $\varepsilon_{\text{AsAPD}}$  becomes significant when the SNR increases. Here, the range of SNR in which both  $\varepsilon_{\text{AsNB-DPD}}$  and  $\varepsilon_{\text{AsAPD}}$  are not negligible is considered “moderate” SNR. For example, SNR between -10 dB and 12 dB in this case (phase accuracy requirement  $< 0.1$  degrees) is denoted as the moderate SNR. Obviously, for the moderate SNR, the accuracy of NB-DPD and APD are degraded and bounded by estimation bias, even though  $N$  is sufficiently large.

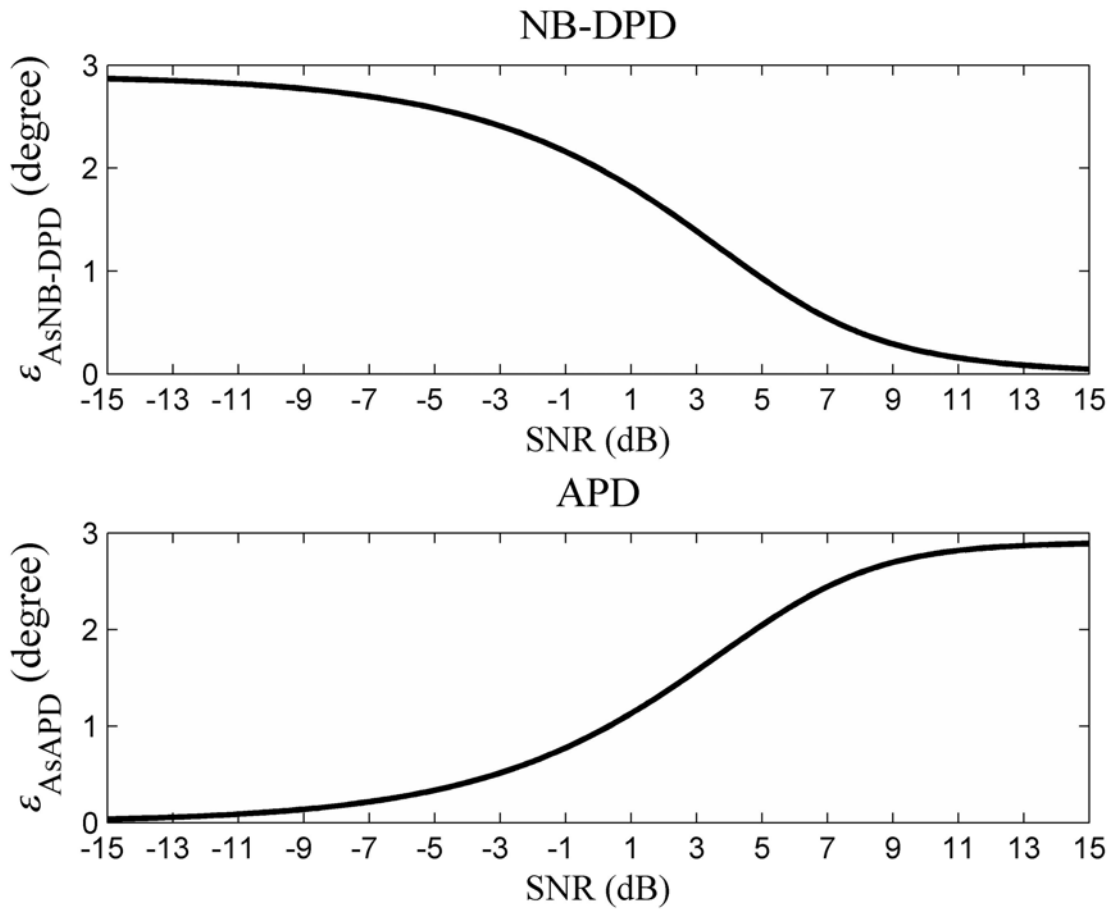


Fig. 2.6. Asymptotic performance of NB-DPD and APD regarding SNR.

Note that, even though the estimation error due to noise variance decreases with the square root of the SNR in APD, as indicated in Eq. (2.30), the accuracy of APD is degraded because of the estimation bias in moderate SNR. This result explains the degradation of  $\varepsilon_{\text{APD}}$  in moderate SNR as shown in Fig. 2.5. Above all, although NB-DPD and APD perform well in high and low SNR, respectively, their performance is degraded by the estimation bias in moderate SNR. Focusing on the moderate SNR, we develop an approach for reducing the estimation bias and thus improving the accuracy in the following section.

## 2.3 SNR-Aided Phase Discriminator

### 2.3.1 Proposed method

Since the mean I-Q outputs vary with the SNR as shown in Fig. 2.2, the SNR should be taken into consideration in achieving high-accuracy phase estimation. Therefore, the SNRaPD is developed to improve the accuracy by using the SNR information. Let  $(\mu_I, \mu_Q)$  be the mean values of the I-Q output and  $(I_m, Q_m)$  be the measured I-Q channel output. In SNRaPD, we define a measure by

$$\begin{aligned} L(\phi) &= (I_m - \mu_I)^2 + (Q_m - \mu_Q)^2 \\ &= (\lambda_1(\phi))^2 + (\lambda_2(\phi))^2 \end{aligned} \quad (2.35)$$

where  $\lambda_1(\phi) = I_m - \mu_I$ ,  $\lambda_2(\phi) = Q_m - \mu_Q$ , and  $\phi$  is the unknown phase to be estimated. In addition, let  $\Lambda(\phi) = [\lambda_1(\phi), \lambda_2(\phi)]^T$ , where ‘T’ denotes transpose and  $L(\phi) = \Lambda(\phi)^T \Lambda(\phi)$ .

When the SNR information is given,  $\gamma$  is known, and the relationship of  $(\mu_I, \mu_Q)$  with respect to phase angle can be uniquely determined. When  $(I_m, Q_m)$  are given, suppose the most likely phase is what minimizes  $L(\phi)$  as follows:

$$\hat{\phi}_{\text{SNRaPD}} = \arg \min \{L(\phi)\}. \quad (2.36)$$

This is the main idea of SNRaPD.

In optimization theory, the foregoing descriptions are known as *the nonlinear least-square problem*. Newton's method can be used to search  $\hat{\phi} = \arg \min \{L(\phi)\}$  [40]. The vector of the first derivatives of  $\lambda_1(\phi)$  and  $\lambda_2(\phi)$  is given by

$$\mathbf{J}(\phi) = \begin{bmatrix} \frac{d\lambda_1(\phi)}{d\phi} & \frac{d\lambda_2(\phi)}{d\phi} \end{bmatrix}^T. \quad (2.37)$$

In addition, let

$$H(\phi) = \lambda_1(\phi)h_1(\phi) + \lambda_2(\phi)h_2(\phi) \quad (2.38)$$

where

$$h_1(\phi) = \frac{d^2\lambda_1(\phi)}{d\phi^2}$$

$$h_2(\phi) = \frac{d^2\lambda_2(\phi)}{d\phi^2}.$$

Then using Newton's method,  $\phi$  is updated iteratively by

$$\phi_i = \phi_{i-1} - (\mathbf{J}(\phi_{i-1})^T \mathbf{J}(\phi_{i-1}) + H(\phi_{i-1}))^{-1} \mathbf{J}(\phi_{i-1})^T \Lambda(\phi_{i-1}) \quad (2.39)$$

where the  $\phi_i$  denotes the phase obtained after the  $i$ -th iteration.

In SNRaPD, depending on the available SNR information, the initial phase  $\phi_0$  can be estimated by NB-DPD or APD, and accuracy can then be improved iteratively by Eq. (2.39). The iteration will stop when  $|\phi_i - \phi_{i-1}| < \delta$ , where  $\delta$  is a small number. In the one-bit SDR

shown in Fig. 2.1, let the carrier frequency  $f_c = 15.421111$  MHz, the sampling frequency  $f_s = 4.096$  MHz, and  $N = 10^5$ . In this case, according to Eq. (2.3), we have  $p = 4096000$  and  $2\pi/p$  will be significantly smaller than the estimation accuracy described below. The performance of SNRaPD is evaluated by Monte Carlo simulation. In the simulation, the stop criterion is  $\delta = 10^{-3}$  degrees, and the estimated phase is given by  $\hat{\phi}_{\text{SNRaPD}} = \phi_i$ . The RMSE defined by  $\varepsilon_{\text{SNRaPD}} = \sqrt{E[(\hat{\phi}_{\text{SNRaPD}} - \phi)^2]}$  is the average of 100 trials as shown in Fig. 2.7. From Fig. 2.7, the errors by NB-DPD and APD are reduced with SNRaPD. For example, at SNR = 0dB, the RMSE of NB-DPD is 2.017 degrees and that of SNRaPD is 0.2625 degrees. A 7.7 times improvement is achieved. At SNR = 10dB, the RMSE of APD is 2.769 degrees and that of SNRaPD is 0.119 degrees, resulting in a 23 times improvement. The SNRaPD greatly improves the accuracy of phase estimation, especially in moderate SNR.

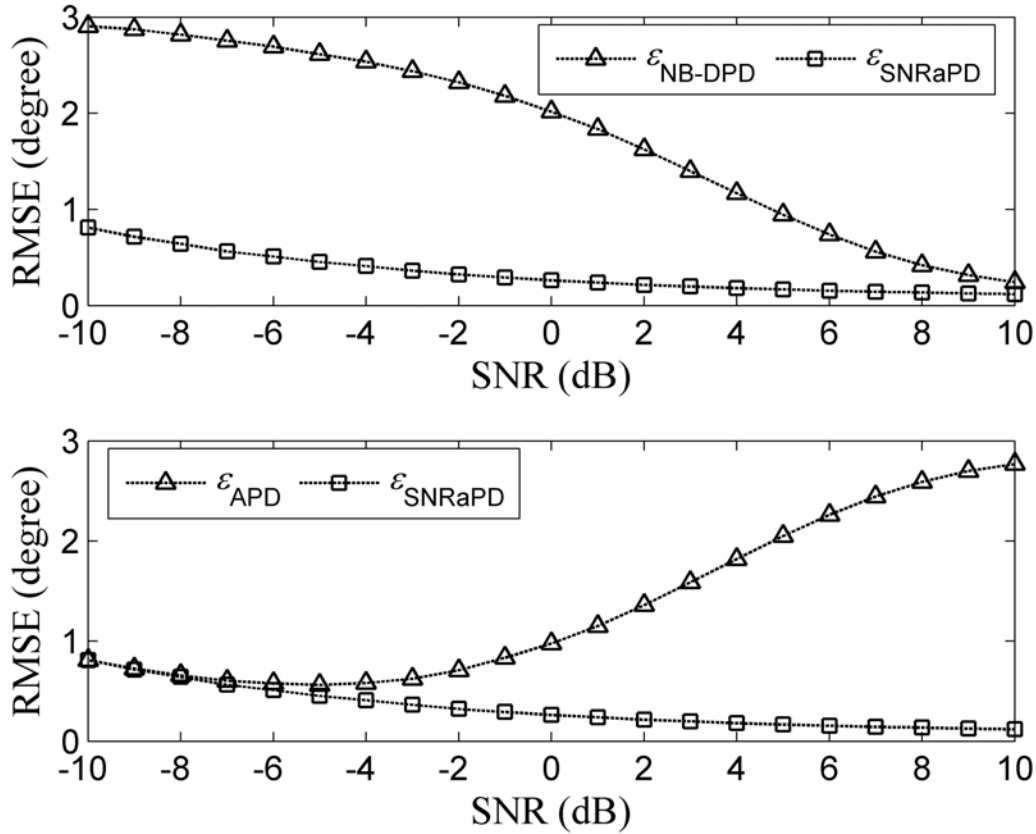


Fig. 2.7. Performance of SNRaPD regarding SNR.

Regarding the number of iterations of Newton's method in SNRaPD, normally less than four iterations are required based on our simulation results. In addition, as mentioned in Section 2.2, NB-DPD and APD perform well in high and low SNR, respectively. Hence, fewer iterations are required in SNRaPD when the initial phase is estimated by NB-DPD in high SNR and by APD in low SNR.

### 2.3.2 Cramér-Rao bound

The CRB for one-bit quantized complex-valued signals was derived in [16]. The performance of SNRaPD is compared with the CRB of the estimated phase. For simplicity, only the real-value case is considered. The probability mass function of  $r[k]$  in Eq. (2.2) is given by

$$f_r(q; \phi) = \text{Prob}(q \cdot r[k] > 0; \phi) = \frac{1}{\sqrt{2\pi}\sigma} \int_0^\infty \exp\left(-\frac{(r - q \cdot \sin(\Phi_k + \phi))^2}{2\sigma^2}\right) dr. \quad (2.40)$$

The Fisher information is then obtained by

$$\begin{aligned} \mathbf{I}(\phi) &= \sum_{k=0}^{N-1} \sum_{q=\pm 1} \frac{1}{f_r(q; \phi)} \frac{\partial f_r}{\partial \phi}(q; \phi) \frac{\partial f_r}{\partial \phi}(q; \phi)^T \\ &= \frac{1}{2\pi\sigma^2} \sum_{k=0}^{N-1} \psi(\Phi_k + \phi; 1/\sigma) \end{aligned} \quad (2.41)$$

where

$$\psi(\Phi_k + \phi; 1/\sigma) = \frac{4 \cos^2(\Phi_k + \phi) \cdot \exp\left(-\frac{1}{\sigma^2} \sin^2(\Phi_k + \phi)\right)}{1 - \text{erf}((1/\sqrt{2}\sigma) \cdot \sin(\Phi_k + \phi))^2}$$

$$\text{erf}(x) = \frac{2}{\sqrt{\pi}} \int_0^x \exp(-t^2) dt.$$

To investigate the achievable performance of SNRaPD, we assume that the frequency in Eq. (2.41) is zero, i.e.  $\Phi_k = 0$ , and the phase is a uniform random variable. We define the average Fisher information by averaging Eq. (2.41) over phases, which is denoted by

$$\begin{aligned}\bar{I} &= \frac{1}{2\pi} \int_0^{2\pi} I(\varphi) d\varphi \\ &= \frac{N}{2\pi\sigma^2} \bar{\psi}(1/\sigma)\end{aligned}\quad (2.42)$$

where  $\bar{\psi}(1/\sigma) = \frac{1}{2\pi} \int_0^{2\pi} \psi(\varphi; 1/\sigma) d\varphi$ .

Taking the inverse of the average Fisher information, we have the average CRB given by

$$\text{AvCRB} = \frac{\pi}{N \cdot \text{SNR} \cdot \bar{\psi}(1/\sigma)} \quad (2.43)$$

where SNR is defined by Eq. (2.9)

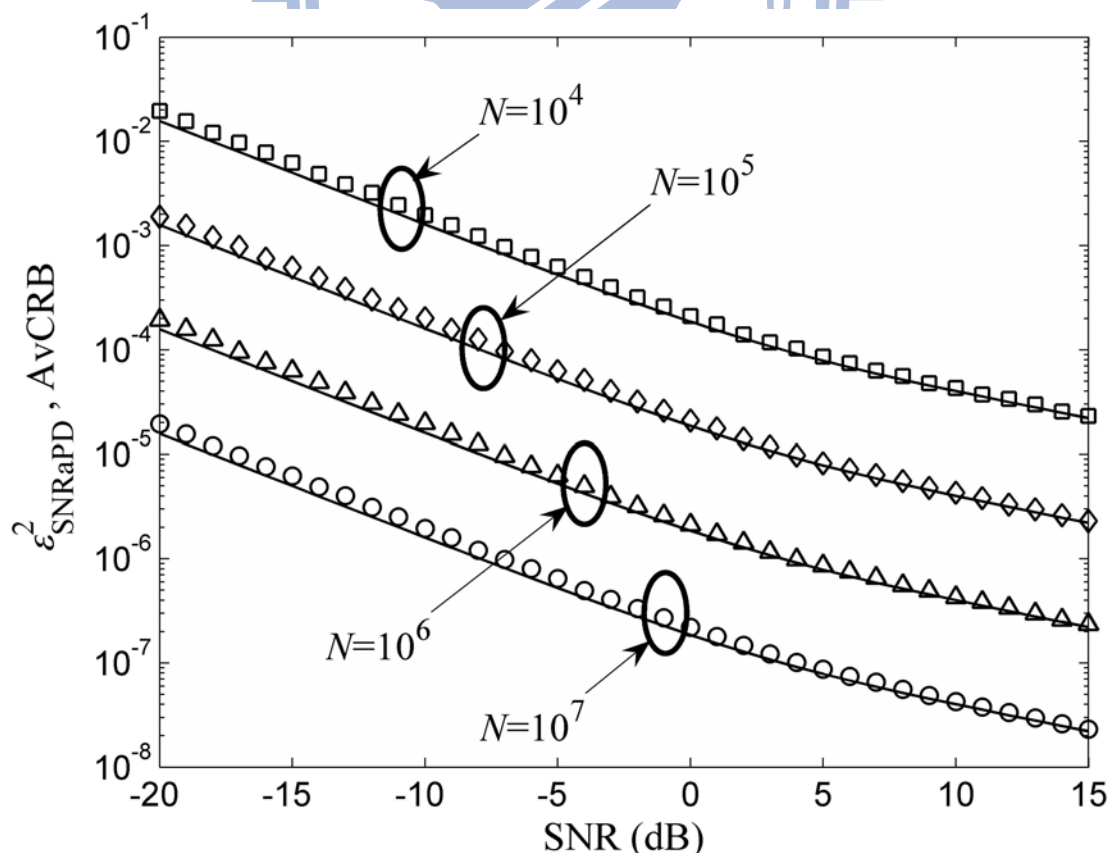


Fig. 2.8. MSE of SNRaPD (markers) and AvCRB (solid lines).



The MSE of SNRaPD defined by  $\varepsilon_{\text{SNRaPD}}^2 = E[(\hat{\phi}_{\text{SNRaPD}} - \phi)^2]$  is compared with the AvCRB in Fig. 2.8. The AvCRB is plotted with solid lines, and the  $\varepsilon_{\text{SNRaPD}}^2$  is denoted by markers. The performance of SNRaPD is obtained from Monte Carlo simulation using 100 trials. In Fig. 2.8,  $\varepsilon_{\text{SNRaPD}}^2$  is close to AvCRB and their difference approaches zero with increasing SNR. Thus the accuracy of SNRaPD is validated. Note that the difference between AvCRB and  $\varepsilon_{\text{SNRaPD}}^2$  is similar for different values of  $N$ .

### 2.3.3 Stop criterion

As mentioned at the end of Section 2.3.1, although estimation bias is reduced by SNRaPD, and  $\hat{\phi}_{\text{SNRaPD}} = \arg \min \{L(\phi)\}$  is achieved by Newton's method, noise variance still exists in  $\hat{\phi}_{\text{SNRaPD}}$ . As a result, the strict criterion  $|\phi_i - \phi_{i-1}| < 10^{-3}$  (degrees) may result in the need for extra iterations, but the performance cannot be improved. From Eq. (2.35), the first derivative of  $L(\phi)$  is given by

$$\begin{aligned} \frac{dL(\phi)}{d\phi} &= 2 \left[ \lambda_1(\phi) \frac{d\lambda_1(\phi)}{d\phi} + \lambda_2(\phi) \frac{d\lambda_2(\phi)}{d\phi} \right] \\ &= 2\mathbf{J}^T(\phi) \mathbf{\Lambda}(\phi). \end{aligned} \quad (2.44)$$

Note that the original criterion  $|\phi_i - \phi_{i-1}| < 10^{-3}$  is consistent with  $dL(\hat{\phi}_{\text{SNRaPD}})/d\phi = 0$ , since  $\hat{\phi}_{\text{SNRaPD}} = \arg \min \{L(\phi)\}$ . As we consider the noise variance with Eq. (2.44), a new stop criterion is defined for SNRaPD as follows. Let  $\phi = \phi_c + \Delta\phi_c$  in Eq. (2.44), where  $\phi_c$  is the true phase, and  $\Delta\phi_c$  is the phase error due to noise variance. Since the AvCRB of Eq. (2.43) is the theoretical bound of variance, let  $\Delta\phi_c = \sqrt{\text{AvCRB}}$ . The new stop criterion is defined by

$$|2\mathbf{J}(\phi_i)^T \mathbf{\Lambda}(\phi_i)| < |2\mathbf{J}(\phi_c + \Delta\phi_c)^T \mathbf{\Lambda}(\phi_c + \Delta\phi_c)|. \quad (2.45)$$

Note that the absolute value is used since the same result but with opposite polarity is obtained by  $\phi = \phi_c - \Delta\phi_c$ . In addition, the criterion  $|2\mathbf{J}(\phi_c + \Delta\phi_c)^T \mathbf{\Lambda}(\phi_c + \Delta\phi_c)|$  is a function of  $\phi_c$ , and the minimal value occurs when  $\phi_c = k\pi/2$ . Hence, the criterion is further defined by  $|2\mathbf{J}(\phi_c + \Delta\phi_c)^T \mathbf{\Lambda}(\phi_c + \Delta\phi_c)|_{\phi_c=k\pi/2}$  to guarantee that the criterion is valid for all phases.

*Example—Determination of the stop criterion:* Let  $\text{SNR} = 6\text{dB}$ ,  $N = 10^5$ , and  $\phi_c = 0^\circ$ .

According to Eq. (2.43),  $\Delta\phi_c = \sqrt{\text{AvCRB}} = 0.12215^\circ$ . Applying  $\phi = \phi_c + \Delta\phi_c = 0.12215^\circ$  to Eq. (2.44), we have  $|2\mathbf{J}(0.12215^\circ)^T \mathbf{\Lambda}(0.12215^\circ)| = 0.001712$ . Hence, the iteration will stop when  $|2\mathbf{J}(\phi_i)^T \mathbf{\Lambda}(\phi_i)| < 0.001712$ .

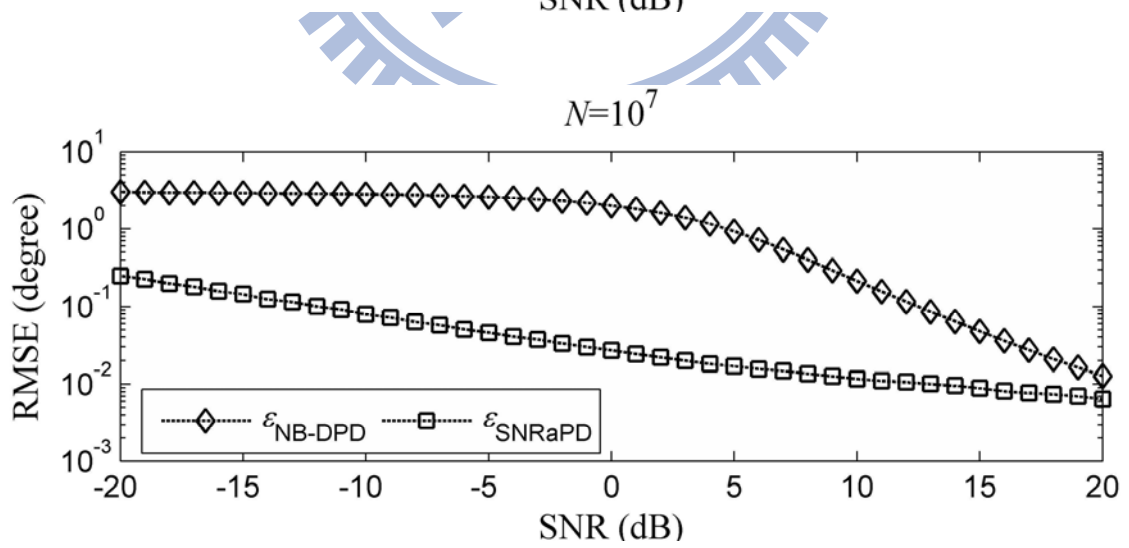
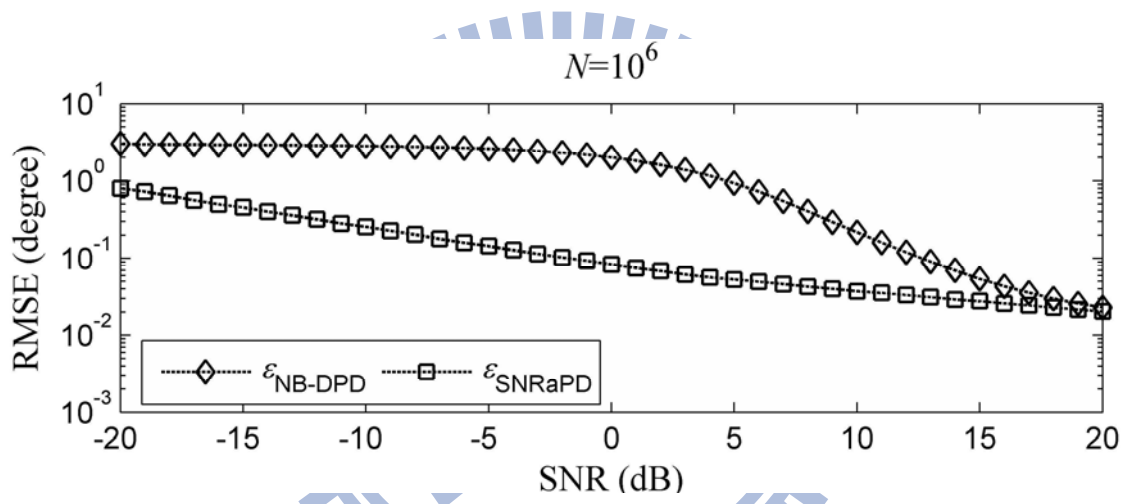
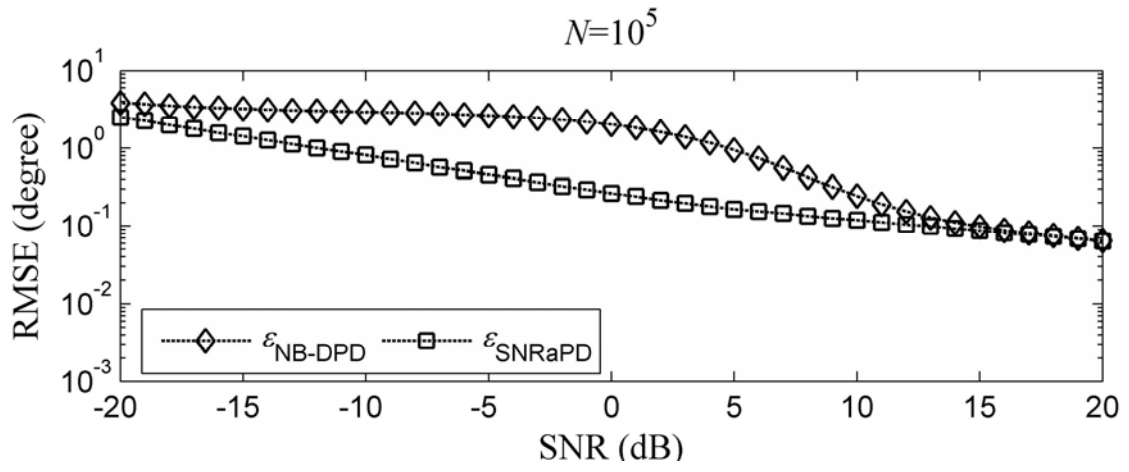
A similar RMSE is achieved with the new stop criterion according to the simulation results, which confirms our supposition. Moreover, the number of iterations is reduced with the new criterion. Recall that the original criterion is consistent with  $dL(\hat{\phi}_{\text{SNRaPD}})/d\phi = 0$ . Since Newton's method will reach the criterion of  $dL(\phi)/d\phi = 2|\mathbf{J}^T(\phi_c + \Delta\phi_c)\mathbf{\Lambda}(\phi_c + \Delta\phi_c)|$  before that of  $dL(\hat{\phi}_{\text{SNRaPD}})/d\phi = 0$ , the number of iterations is reduced accordingly.

Finally, most computational loads of SNRaPD fall in computing  $\lambda_1(\phi)$  and  $\lambda_2(\phi)$  as well as their derivatives, which involve  $\mu_I$  and  $\mu_Q$  of Eq. (2.11) and Eq. (2.13), respectively. In practice, we use  $M$  terms to approximate  $\mu_I$  and  $\mu_Q$  rather than infinite sums. Moreover, we can calculate and store coefficients in a table in order to further mitigate the computational burdens. For applications with SNR less than 0 dB,  $M = 8$  is sufficient to well approximate  $\mu_I$  and  $\mu_Q$  with RMSE smaller than  $10^{-6}$ . In addition, less than four

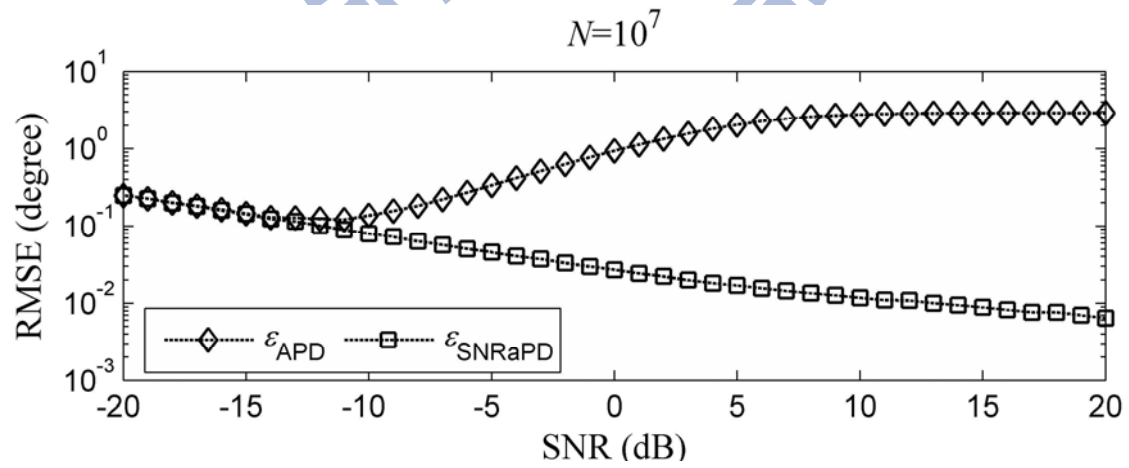
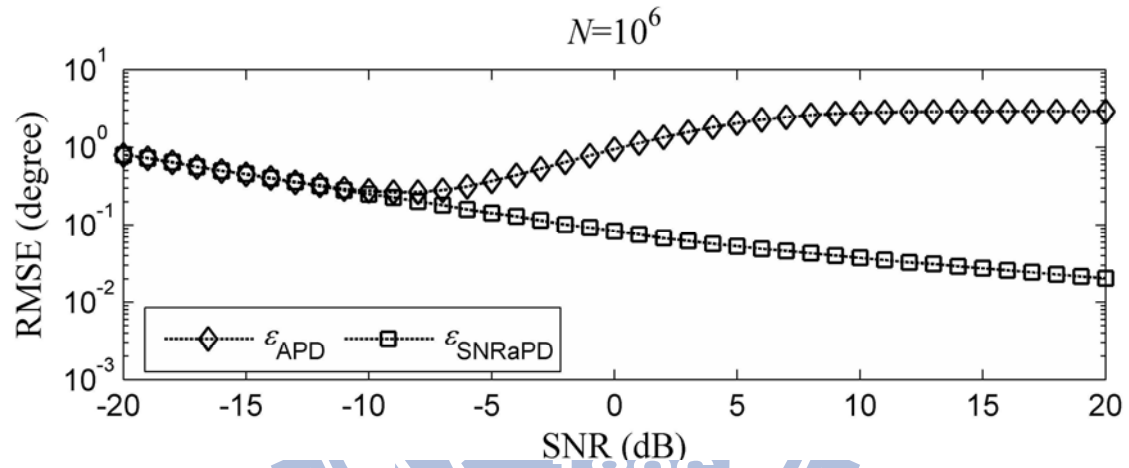
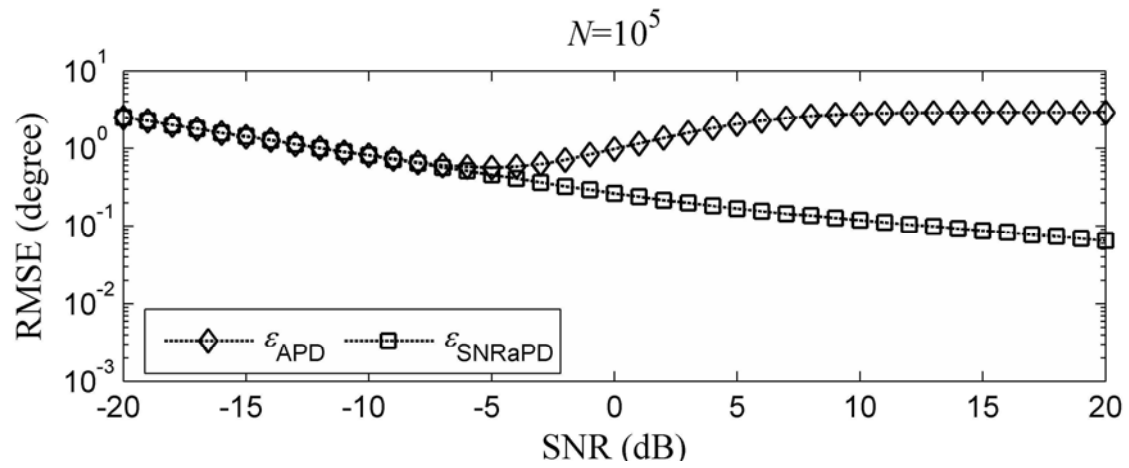
iterations are normally required from our simulation results. Therefore the computational burden of SNRaPD is feasible, given today's fast processors.

### 2.3.4 Range of application

The range of application of SNRaPD is studied by comparing  $\varepsilon_{\text{SNRaPD}}$  with  $\varepsilon_{\text{NB-DPD}}$  and  $\varepsilon_{\text{APD}}$ . The simulated results regarding SNR and  $N$  are illustrated in Fig. 2.9. From Fig. 2.9(a), compared with NB-DPD, the improvement in the accuracy of SNRaPD is significant in moderate SNR. Note that the range of the moderate SNR may vary according to  $N$  and the required phase accuracy for different applications. Moreover, in  $N=10^5$  and  $N=10^6$  cases, the improvement is negligible when the SNR is above 12 dB and 17 dB, respectively. As  $N$  increases to  $10^7$ , SNRaPD can consistently improve the accuracy to some degree for SNR below 20 dB. Similarly, in comparing SNRaPD with APD, the accuracy is greatly improved in moderate to high SNR as shown in Fig. 2.9(b). The improvement is negligible when the SNR is below -4 dB, -8 dB, and -12 dB, respectively. The above discussion illustrates the superiority of the proposed SNRaPD in “moderate” SNR. As the ambient SNR is increased to the “moderate” range, SNRaPD can potentially be used and provide improved accuracy in spaceborne measurement techniques, such as the total electron content (TEC) measurements on a beacon receiver or the precise orbit determination (POD) on a GNSS receiver [41-45]. For example, when  $N=10^6$  and SNR = 0dB on the 400 MHz beacon signal, the phase error is 0.08 degrees and 0.94 degrees for SNRaPD and APD, respectively. The estimation error of SNRaPD is approximately an order better than that of APD. If more samples are utilized, the superiority of SNRaPD over APD remains significant even when the SNR is lower than 0 dB as shown in Fig. 2.9(b).



(a)



(b)

Fig. 2.9. Comparison between RMSE of SNRaPD and that of NB-DPD and APD.

## 2.4 Summary

In this chapter, the high-accuracy phase estimation for one-bit SDR is investigated. We propose the SNRaPD using the SNR information to reduce the estimation bias and achieve the high-accuracy phase estimation. The mean values and variances of the I-Q channel outputs in one-bit SDR are given by Eq. (2.11), Eq. (2.13) and Eq. (2.16), and the SNR-dependent relationship of the mean I-Q channel outputs is explicitly shown in Fig. 2.2. For high-accuracy phase estimation, NB-DPD can be used in high SNR as shown in Fig. 2.3. For the low SNR, APD is selected according to Eq. (2.20), and its performance is illustrated in Fig. 2.5. However, according to the asymptotic performance of NB-DPD and APD as shown in Fig. 2.6, the estimation bias becomes significant and can have a negative impact on the accuracy in moderate SNR. Focusing on this SNR range, we proposed SNRaPD using Newton's method to reduce bias and improve the resulting accuracy as shown in Fig. 2.7. The accuracy of SNRaPD is certified by comparing the MSE with the AvCRB in Fig. 2.8. In order to conserve computation time, an adequate stop criterion for SNRaPD with respect to the noise variance is also defined by Eq. (2.45). Finally, the range of the application of SNRaPD is investigated by comparing the associated RMSE with that of NB-DPD and APD as shown in Fig. 2.9. Potential applications of SNRaPD and the corresponding performance on  $\text{SNR} = 0\text{dB}$  are also discussed. Nevertheless, the proposed SNRaPD requires the knowledge of SNR which is not available in many applications. Hence the joint phase and SNR estimation is proposed and introduced in the next chapter.

# Chapter 3

## Joint One-Bit Phase and SNR Estimation

Generally, the SNR information is crucial for the quality control of the observed data [2,5]. Moreover, according to the results of chapter 2, the accurate SNR information enables the accurate phase estimation. Since the SNR information may be unavailable in many applications, we extend the algorithm for SNRaPD to jointly estimate of the phase and SNR. Because the signals are one-bit quantized, the designed method can accommodate high dynamic range applications.

In the following, the signal model of one-bit quantized sinusoidal carrier and the I-Q correlation structure are revisited and adopted for joint phase and SNR estimation first. Next, the nonlinear least-square algorithm of SNRaPD is extended to iteratively derive the phase and SNR estimation. The performance of the proposed method is then verified by Monte Carlo simulations. In addition, the feasibility of the proposed method for applications in GNSS and beacon receivers is also discussed.

### 3.1 System Model

Consider a carrier with amplitude  $A$ , frequency  $f_c$  and phase  $\phi$ . When the signal is disturbed by AWGN, the observed wave is denoted by

$$x(t) = A \sin(2\pi f_c t + \phi) + n(t) \quad (3.1)$$

where  $n(t)$  is AWGN with zero mean and variance  $\sigma^2$ .

The SNR of  $x(t)$  is given by

$$\rho = \frac{A^2}{2\sigma^2}. \quad (3.2)$$

Note that Eq. (3.1) and Eq. (3.2) are different from their counterparts in chapter 2, i.e. Eq. (2.1) and Eq. (2.9), respectively, only on the amplitude  $A$ . When  $x(t)$  is one-bit quantized and sampled with period  $T_s$ , we have

$$\begin{aligned} x[k] &= \text{sgn}[A \sin(2\pi k f_c T_s + \phi) + n(kT_s)] \\ &= \text{sgn}[A \sin(\psi_k + \phi) + n_k] \end{aligned} \quad (3.3)$$

where  $\psi_k = 2\pi k f_c T_s$  and sampling frequency follows the property of Eq. (2.3).

For parameter estimation, assume that the frequency  $f_c$  is known and the local I-Q components are  $\text{sgn}[\sin \psi_k]$  and  $\text{sgn}[\cos \psi_k]$ , respectively. After one-bit quantization,  $x[k]$  is then multiplied by local I-Q components, and summed to have the I-Q correlation outputs denoted by

$$I = \sum_k x[k] \cdot \text{sgn}[\sin \psi_k] \quad (3.4)$$

$$Q = \sum_k x[k] \cdot \text{sgn}[\cos \psi_k]. \quad (3.5)$$

Similar to Eq. (2.5), we consider  $p$  samples at  $t = kT_s$ ,  $k = 0, 1, 2, \dots, p-1$  in I-Q correlation outputs, where  $p$  is specified in Eq. (2.3). The normalized I-Q outputs from these samples are expressed by

$$I_p = \frac{1}{p} \sum_{k=0}^{p-1} \text{sgn}[A \sin(\psi_k + \phi) + n_k] \cdot \text{sgn}[\sin \psi_k] \quad (3.6)$$



$$Q_p = \frac{1}{p} \sum_{k=0}^{p-1} \text{sgn}[A \sin(\psi_k + \phi) + n_k] \cdot \text{sgn}[\cos \psi_k]. \quad (3.7)$$

According to Appendix A, the mean values of Eq. (3.6) and Eq. (3.7) are denoted by

$$\mu_{I_p} = \frac{2}{p} \left[ \sum_{\psi_k \in [\pi, 2\pi)} Q(\sqrt{2\rho} \sin(\psi_k + \phi)) - \sum_{\psi_k \in [0, \pi)} Q(\sqrt{2\rho} \sin(\psi_k + \phi)) \right] \quad (3.8)$$

$$\mu_{Q_p} = \frac{2}{p} \left[ \sum_{\psi_k \in [\pi/2, 3\pi/2)} Q(\sqrt{2\rho} \sin(\psi_k + \phi)) - \sum_{\psi_k \in [0, \pi/2) \cup [3\pi/2, 2\pi)} Q(\sqrt{2\rho} \sin(\psi_k + \phi)) \right] \quad (3.9)$$

where

$$Q(x) = \frac{1}{\sqrt{2\pi}} \int_x^{\infty} \exp\left(-\frac{z^2}{2}\right) dz.$$

In addition, the variance of I-Q correlation outputs is given by

$$\begin{aligned} \sigma_{I_p}^2 &= \sigma_{Q_p}^2 \\ &= \frac{4}{p^2} \left[ \sum_{k=0}^{p-1} Q(\sqrt{2\rho} \sin(\psi_k + \phi)) - Q(\sqrt{2\rho} \sin(\psi_k + \phi))^2 \right]. \end{aligned} \quad (3.10)$$

When the number of samples is generalized to  $N = m \cdot p$  and  $m$  is an integer, the I-Q outputs are denoted as  $I_m$  and  $Q_m$ , respectively. Let their mean value be  $\mu_I$  and  $\mu_Q$ , respectively. It is easily proved that  $I_m$  and  $Q_m$  have the same mean values as  $I_p$  and  $Q_p$ , i.e.  $\mu_I = \mu_{I_p}$  and  $\mu_Q = \mu_{Q_p}$ . In addition, the variance of  $I_m$  and  $Q_m$  is given by

$$\begin{aligned} \sigma_I^2 &= \sigma_Q^2 \\ &= \frac{4}{N^2} \left[ \sum_{k=0}^{N-1} Q(\sqrt{2\rho} \sin(\psi_k + \phi)) - Q(\sqrt{2\rho} \sin(\psi_k + \phi))^2 \right]. \end{aligned} \quad (3.11)$$

### 3.2 Nonlinear Least-Square Algorithm

After deriving the mean value of the I-Q correlation outputs, the nonlinear least-square algorithm is utilized to estimate the phase and SNR of the carrier. Let  $I_m$  and  $Q_m$  be the I-Q outputs of one-bit quantized sinusoidal carrier. The phase and SNR of the carrier are denoted by  $\boldsymbol{\theta} = [\phi, \rho]^T$ , where the superscript 'T' denotes the transpose operation. Let  $\mu_I(\boldsymbol{\theta})$  and  $\mu_Q(\boldsymbol{\theta})$  be the mean values of  $I_m$  and  $Q_m$  regarding parameter  $\boldsymbol{\theta}$ , respectively. When the sampling frequency is carefully selected to have a large  $u$ ,  $I_m$  and  $Q_m$  can be expressed by

$$I_m = \mu_I(\boldsymbol{\theta}) + \xi_I \quad (3.12)$$

$$Q_m = \mu_Q(\boldsymbol{\theta}) + \xi_Q \quad (3.13)$$

where  $\xi_I$  and  $\xi_Q$  are random variables in I-Q correlation outputs with variance given by Eq. (3.11).

To estimate the parameter  $\boldsymbol{\theta}$ , we construct a cost function as

$$\begin{aligned} f(\boldsymbol{\theta}) &= (I_m - \mu_I(\boldsymbol{\theta}))^2 + (Q_m - \mu_Q(\boldsymbol{\theta}))^2 \\ &= (y_1(\boldsymbol{\theta}))^2 + (y_2(\boldsymbol{\theta}))^2 \\ &= \mathbf{y}(\boldsymbol{\theta})^T \mathbf{y}(\boldsymbol{\theta}) \end{aligned} \quad (3.14)$$

where  $\mathbf{y}(\boldsymbol{\theta}) = [y_1(\boldsymbol{\theta}), y_2(\boldsymbol{\theta})]^T$ .

The estimation of  $\boldsymbol{\theta}$  is denoted by

$$\hat{\boldsymbol{\theta}} = \arg \min f(\boldsymbol{\theta}). \quad (3.15)$$

Equation (3.14) and Eq. (3.15) form a nonlinear least-square problem. According to Eq. (3.14), the gradient of  $f(\boldsymbol{\theta})$  is given by

$$\nabla f(\boldsymbol{\theta}) = 2\mathbf{J}(\boldsymbol{\theta})^T \mathbf{y}(\boldsymbol{\theta}) \quad (3.16)$$

where  $\mathbf{J}(\boldsymbol{\theta})$  is the Jacobian matrix of  $\mathbf{y}(\boldsymbol{\theta})$ .

In addition, the Hessian matrix of  $f(\boldsymbol{\theta})$  is denoted by

$$\mathbf{F}(\boldsymbol{\theta}) = 2(\mathbf{J}(\boldsymbol{\theta})^T \mathbf{J}(\boldsymbol{\theta}) + \mathbf{H}(\boldsymbol{\theta})) \quad (3.17)$$

where  $\mathbf{H}(\boldsymbol{\theta})$  is the matrix whose  $(p, q)$ -th element is given by

$$\sum_{j=1}^2 y_j \cdot \frac{\partial^2 y_j}{\partial \theta_p \partial \theta_q}.$$

The nonlinear least-square problem of Eq. (3.15) can then be solved, and  $\hat{\boldsymbol{\theta}}$  is iteratively estimated by [40]

$$\boldsymbol{\theta}^{(i)} = \boldsymbol{\theta}^{(i-1)} - (\mathbf{F}(\boldsymbol{\theta}))^{-1} \nabla f(\boldsymbol{\theta}). \quad (3.18)$$

The iteration of Eq. (3.18) is stopped when  $\|\boldsymbol{\theta}^{(i)} - \boldsymbol{\theta}^{(i-1)}\| < \varepsilon$ , where  $\varepsilon$  is a small number.

When the stop criterion is reached after the  $i$ -th iteration, the estimated result is given by

$$\hat{\boldsymbol{\theta}} = \boldsymbol{\theta}^{(i)}. \quad (3.19)$$

The initial phase and SNR of  $\boldsymbol{\theta}^{(0)}$  for Eq. (3.18) are determined as follows.

### 1) Initial value of phase

It is known that APD achieves MLE for discrete-time samples in a multi-bit scenario [12]. For one-bit quantized data, although the accuracy may be degraded to some degree, the initial phase of our approach can be readily determined by APD, which is denoted by

$$\phi_0 = \tan^{-1}\left(\frac{Q_m}{I_m}\right). \quad (3.20)$$

### 2) Initial value of SNR

After the initial phase is determined, let  $\phi = \phi_0$  for  $\mu_I(\boldsymbol{\theta})$  and  $\mu_Q(\boldsymbol{\theta})$  in Eq. (3.14). Then Eq. (3.14) is degenerated to be a function of  $\rho$ . Subsequently, the initial SNR can be determined by searching the minimum value with respect to  $\rho$  in Eq. (3.14). The one-dimensional search technique, the Golden section method [40], is used to find the initial SNR, i.e.  $\rho_0$ . Note that the accuracy of  $\rho_0$  is affected by the variance of  $\phi_0$ . Hence a loose stop criterion is used in the Golden section method to find the coarse  $\rho_0$ , and the computation time can be conserved.

## 3.3 Simulation and Discussion

### 3.3.1 Monte Carlo simulation

The Monte Carlo simulations are used to verify the joint phase and SNR estimation method, wherein each case of different SNR and  $N$  is tested for 1000 trials. Let  $f_c = 1.157\text{MHz}$  and  $f_s = 4.096\text{MHz}$  in the simulation, then  $p = 4096$  according to Eq. (2.3). Assume  $\hat{\phi}_j$  is the estimated phase of the  $j$ -th trial, and  $\phi$  is the true phase. The root mean-squared error (RMSE) of phase estimation is defined by

$$\text{RMSE}(\hat{\phi}) = \left[ \frac{1}{1000} \sum_{j=1}^{1000} (\hat{\phi}_j - \phi)^2 \right]^{1/2}. \quad (3.21)$$

For SNR estimation, the RMSE is normalized to clarify the performance, which is denoted by

$$\text{nRMSE}(\hat{\rho}) = \frac{1}{\rho} \left[ \frac{1}{1000} \sum_{j=1}^{1000} (\hat{\rho}_j - \rho)^2 \right]^{1/2}. \quad (3.22)$$

where  $\hat{\rho}_j$  is the estimated SNR of the  $j$ -th trial, and  $\rho$  is the actual SNR.

In the nonlinear least-square algorithm of Eq. (3.18), the stop criterion is given by  $\varepsilon = 0.0001$ . In addition, for using the Golden section method to determine the initial SNR, a coarse resolution of 0.5 dB is used for the stop criterion. The one-bit ADC is commonly used in low-power satellite applications. For potential applications on GNSS receivers, the proposed method will be simulated for SNR as low as  $-30$  dB. On the other hand, to illustrate wide applicable range of our method, SNR up to 15 dB is also considered.

The performance of phase and SNR estimation are illustrated in Fig. 3.1 and Fig. 3.2, respectively. Note that the RMSE of SNR is normalized and denoted by percentages. In Fig. 3.1, the RMSE of the phase is improved with increasing SNR and  $N$ . The phase RMSE's are below one degree when SNR is higher than  $-12$  dB and  $-22$  dB for  $N = 10^5$  and  $N = 10^6$  cases, respectively. Moreover, the accuracy of 0.1 degrees phase RMSE is achieved when SNR is higher than 12dB and  $-2$ dB in each case. According to Fig. 3.2, the SNR estimation performs well in moderate SNR. Accurate SNR information can be used to learn the achieved accuracy of phase estimation in this range. Specifically, the nRMSE is less than 10% for  $-21 \text{ dB} \leq \text{SNR} \leq 13 \text{ dB}$  when  $N = 10^5$  and for  $-30 \text{ dB} \leq \text{SNR} \leq 14 \text{ dB}$  when  $N = 10^6$ . Moreover, the estimation of SNR can be very accurate, i.e.  $\text{nRMSE} \leq 1\%$ , when  $N = 10^6$  and  $-11 \text{ dB} \leq \text{SNR} \leq 9 \text{ dB}$ .

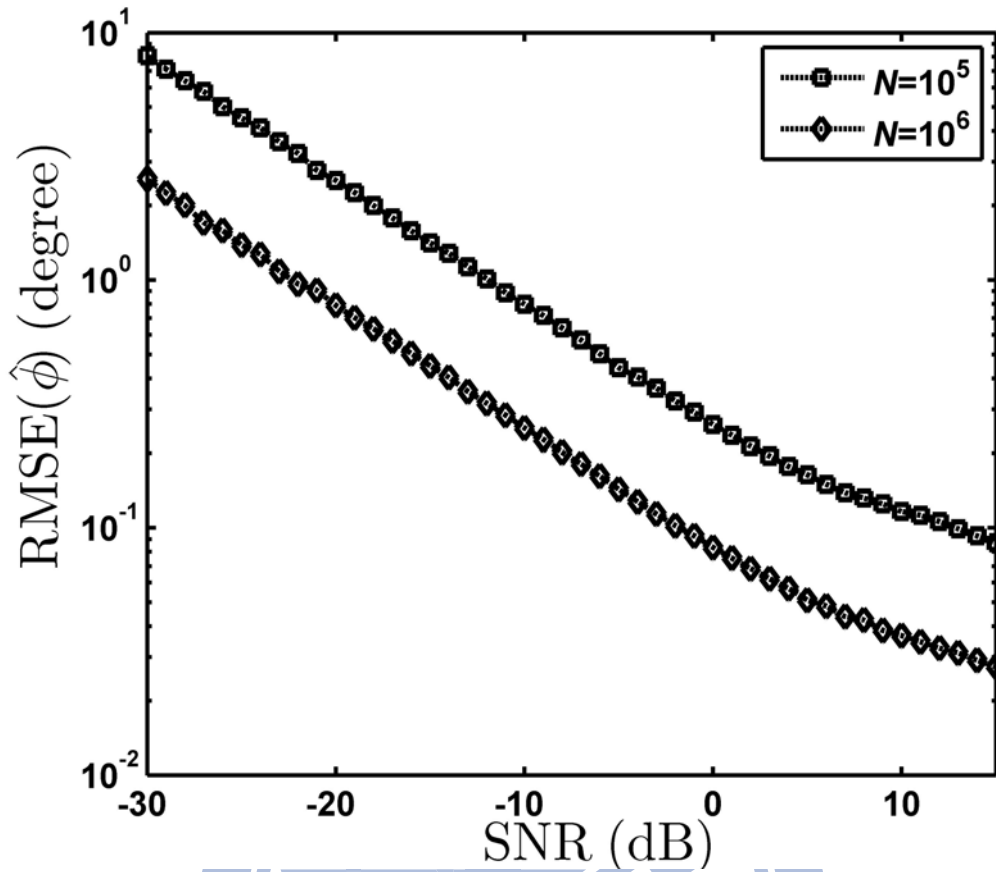


Fig. 3.1. RMSE of phase estimation.

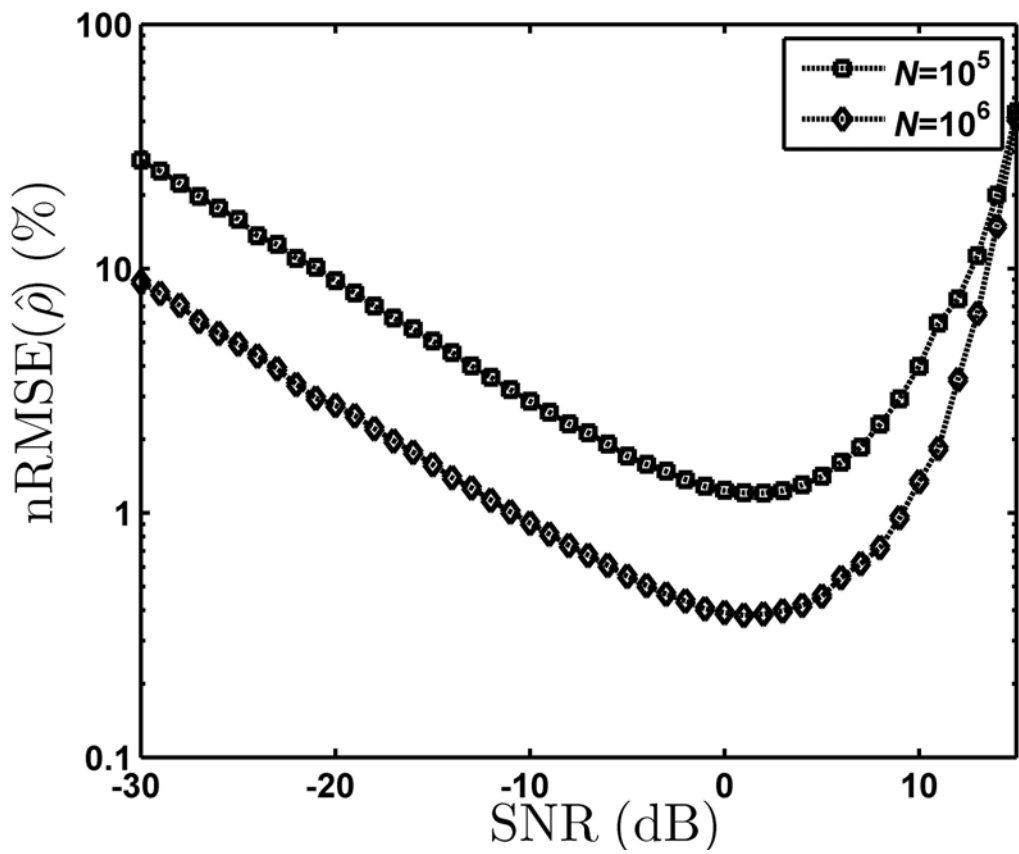


Fig. 3.2. Normalized RMSE of SNR estimation.

Note that the nRMSE attains the lower bound when SNR is around 4 dB, and increases in higher SNR. This phenomenon is investigated by plotting the mean I-Q outputs for  $0 \text{ dB} \leq \text{SNR} \leq 15 \text{ dB}$  as shown in Fig. 3.3. When SNR increases, the distance between neighboring curves becomes smaller and the distinction between them is little. Specifically, for  $\text{SNR} \leq 4 \text{ dB}$  (dotted lines), the separations between the curves are recognizable. However, the distinction between curves becomes closer when  $\text{SNR} > 4 \text{ dB}$  (solid lines). Consequently, when slight variance occurs in the obtained I-Q correlation outputs for SNR higher than 4 dB, the obtained  $I_m$  and  $Q_m$  will be fitted to  $\mu_I(\theta)$  and  $\mu_Q(\theta)$  with significant SNR error in the cost function of Eq. (3.14). Therefore, the performance of SNR estimation becomes degraded. Especially, when  $\text{SNR} \geq 10 \text{ dB}$ , the curves are nearly overlapped, and the error in SNR estimation increases rapidly.

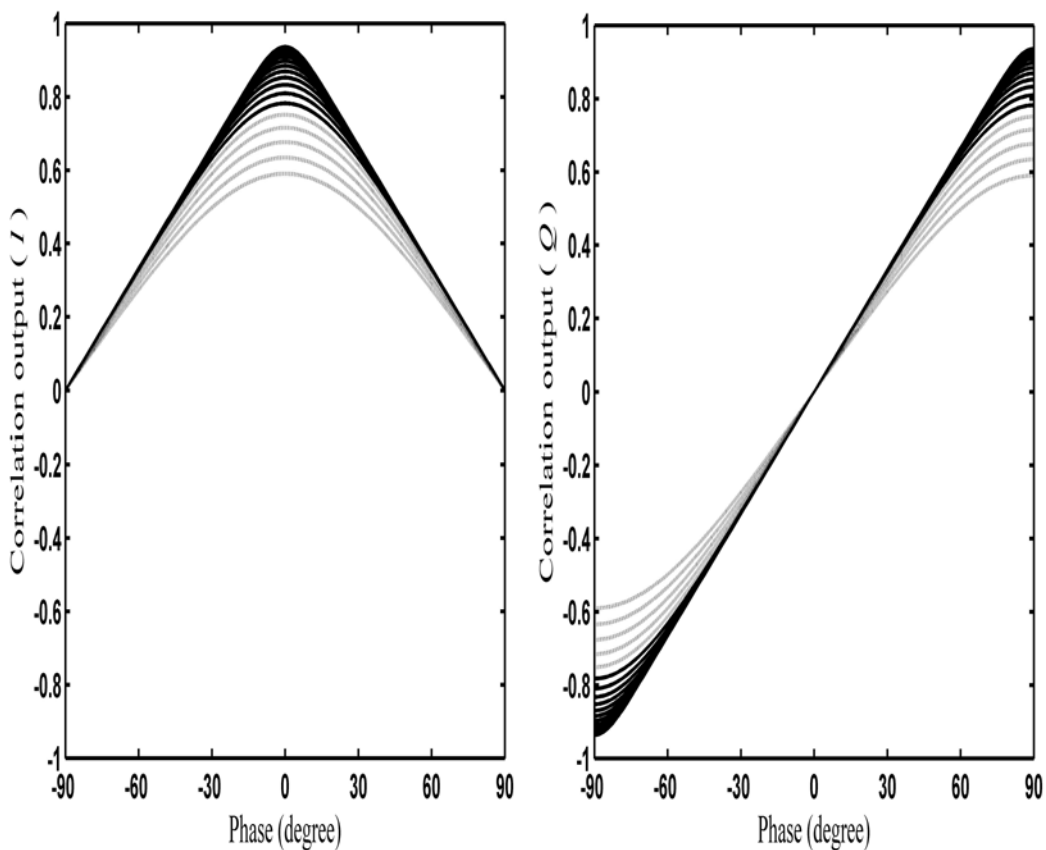


Fig. 3.3. Mean I-Q correlation outputs for SNR between 0 to 15dB in 1dB step.

Recalling that the variance of I-Q correlation outputs is approximately inversely proportional to  $N$ , the standard deviation (STD) will decrease with  $\sqrt{N}$ . Hence, the performance of the nonlinear least-square algorithm can be improved with  $\sqrt{N}$ . This is consistent with the simulation results shown in Fig. 3.1 and Fig. 3.2. The results suggest that  $N$  can be increased to compensate for the loss of amplitude information due to one-bit quantization and the desired accuracy can be achieved.

### 3.3.2 Range of applications

*GNSS receiver:* For applications using carrier phase in GNSS receivers, the signal bandwidth is assumed to be 2 MHz concerning the coarse/acquisition (C/A) code. According to the measured results of [46], when the elevation angles between  $20^\circ$  and  $90^\circ$  are of interest, SNR from  $-30\text{dB}$  to  $-10\text{ dB}$  will be considered for different applications. According to the simulation results of  $N=10^6$ , the phase RMSE's of our method are 2.5545 and 0.25203 degrees for SNR of  $-30\text{dB}$  and  $-10\text{ dB}$ , respectively. For L1 carrier (1575.42 MHz), these errors correspond to 1.35 mm and 0.13 mm in length, and 1.73 mm to 0.17 mm for L2 carrier (1227.6 MHz). Such performances are close to those of high-quality receivers [44, 46]. Note that C/A code synchronization is assumed to be achieved before carrier phase estimation. In addition, the nRMSE of SNR is less than 9% when  $N=10^6$  and SNR is between  $-30\text{dB}$  and  $-10\text{ dB}$ . Regarding the potential application of POD in low Earth orbit satellites (LEO), the accuracy of the orbit will be influenced by the satellite center variation, the attitude error, and the antenna phase variation, which are at the centimeter level [47]. Our achieved phase RMSE is much smaller than these variations. In addition, the phase RMSE is also insignificant with respect to the ultimate accuracy after the orbit determination algorithm reported in [47-49]. Hence, even though the proposed one-bit processing method is adopted, the reported accuracy of POD in literatures can still be achieved. Furthermore, the quality of data can be controlled by the estimated SNR. When the quality of data deteriorates owing to



the low elevation angle, the cycle slip or the multipath, the unfavorable low-SNR can be detected immediately. These data can be omitted to enhance the accuracy of POD.

*Beacon receiver:* For the tri-band radio beacon (150 MHz, 400 MHz and 1067 MHz) signals now on board of several LEO's, the received power on ground is at least  $-140$  dBm [50]. Assume the noise floor is  $-173$  dBm/Hz, and the bandwidth is 20 KHz concerning the Doppler shift [51]. The minimum input SNR of the beacon receiver is then  $-10$  dB. Suppose the LEO is at an altitude of 450 Km above the sea level. The variation in signal strength is approximately 15 dB. Hence, SNR's between  $-10$  dB and 5 dB are considered at the receiver. When  $N = 10^5$ , the corresponding phase RMSE of the proposed method is from 0.80765 to 0.16384 degrees for SNR between  $-10$  dB and 5 dB. Meanwhile, the nRMSE of SNR is less than 3%. For measuring the TEC of the ionosphere in the beacon receiver, the relationship between the accumulated carrier phase and the TEC is given by [51-52]

$$\phi = \frac{2\pi f}{c} L + \frac{80.6\pi}{cf} N_T, \quad (3.23)$$

where  $L$  is the traveling distance,  $c$  is the speed of light,  $N_T$  is the TEC.

When carrier signals with frequency of  $f_1 = 150$  MHz and  $f_2 = 400$  MHz are used in beacon receiver, letting  $f_r = 50$  MHz,  $q_1 = 3$  and  $q_2 = 8$ , we have  $f_1 = q_1 f_r$  and  $f_2 = q_2 f_r$ . The term related to travelling distance in Eq. (3.23) can be eliminated by means of a differential phase technique. The phase difference measured on the frequency  $f_r$  is then denoted by

$$\begin{aligned} \Delta\phi &= \frac{\phi_1}{q_1} - \frac{\phi_2}{q_2} \\ &= \frac{1}{q_1} \left( \frac{2\pi f}{c} L + \frac{80.6\pi}{cf_1} N_T \right) - \frac{1}{q_2} \left( \frac{2\pi f}{c} L + \frac{80.6\pi}{cf_2} N_T \right) \\ &= \frac{80.6\pi}{cf_r} N_T \left( \frac{1}{q_1^2} - \frac{1}{q_2^2} \right). \end{aligned} \quad (3.24)$$

When the proposed method with  $N = 10^5$  and  $\text{SNR} = -10$  dB is applied to TEC measurements, according to Eq. (3.24), the resulting measurement error is  $8.75 \times 10^{-4}$  TECU (TECU:  $10^{16}$  electrons/m<sup>2</sup>). The achieved accuracy is sufficient for science requirement, i.e. 0.003 TECU [53].

From the above discussion, the use of one-bit ADC cooperated with the proposed joint phase and SNR estimation can achieve high accuracy comparable to conventional approaches. Since one-bit signal processing is simple, fast and without AGC, the proposed approach is feasible for various high precision applications.

### 3.4 Summary

In this chapter, the method utilizing the nonlinear least-square algorithm to accurately estimate both the phase and SNR of sinusoidal carriers is proposed. From simulation results, the phase RMSE decreases with SNR, as shown in Fig. 3.1. The phase RMSE is less than 0.1 degrees when SNR is higher than 12dB and -2dB in the cases of  $N = 10^5$  and  $N = 10^6$ , respectively. In addition, SNR estimation performs well in the middle range, as shown in Fig. 3.2. In particular, the nRMSE is less than 1% for  $N = 10^6$  and SNR between -11dB and 9dB. The nRMSE increases in high SNR region because of the tiny distinction between I-Q correlation outputs as shown in Fig. 3.3. Furthermore, since the STD of the I-Q correlation outputs decreases with  $\sqrt{N}$ , the accuracy of the estimated phase and SNR can be improved by increasing the number of samples, as verified in Fig. 3.1 and Fig. 3.2. Finally, potential applications for the proposed efficient one-bit processing method in GNSS and beacon receivers have been illustrated with respect to the high accuracy of the phase estimation.

# Chapter 4

## Code Phase Coherence Acquisition Method

In this chapter, a computationally-efficient code phase acquisition method, termed the Phase Coherence Acquisition (PCA), is proposed. The method requires much less computation than the FFT-based acquisition to search for the cross-correlation peak between two PN sequences. This superiority becomes evident when the sequence length  $N$  is very large such that the FFT-based approach is difficult to be implemented. For instance, the acquisition of precision code (P code) with extremely long length in the GNSS system would be one of the potential applications. We describe the motivation behind our work first. We then develop our approach in the noiseless case and provide the essential idea in our development. To achieve noise-robustness, we incorporate a novel segmentation scheme and propose the PCA method. Simulation results are provided to verify the analysis and demonstrate the performance of the proposed method. Finally, the computations involved in PCA and the FFT-based method are discussed. Note that the PN sequence with length of  $2^{20} - 1$  is used to demonstrate the two-layer PCA, which is a good compromise between the simulation burden and performance illustration.

### 4.1 Motivation

The convolution theorem states that under general conditions the Fourier transform of a convolution between two sequences is the pointwise product of the Fourier transforms of these two sequences. The theorem can be represented by

$$F \{x[n] \otimes y[n]\} = F \{x[n]\} \cdot F \{y[n]\} \quad (4.1)$$

where  $F$  denotes Fourier transform.

By applying the inverse Fourier transform  $F^{-1}$ , we have

$$x[n] \otimes y[n] = F^{-1} \{ F \{ x[n] \} \cdot F \{ y[n] \} \}. \quad (4.2)$$

In many applications, the code phase search between two sequences is usually implemented by FFT and its inverse due to the efficient computation compared with the exhaustive direct serial search method. The computation of FFT of  $N$  points involves complex multiplications and additions of order  $N \log_2 N$ . Due to the diverse need for applications and the increasing complexity of modern algorithms, a more computationally efficient method is needed when the length of a processed sequence becomes so large that implementation using the FFT method becomes difficult. Our proposal for the code phase acquisition that involves much less computation is developed as follows.

## 4.2 Acquisition by Phasor

Let  $S_{IN} = \{x_0, x_1, \dots, x_{N-1}\}$  and  $S_{LO} = \{y_0, y_1, \dots, y_{N-1}\}$  be the input and local PN sequence of length  $N$ , respectively, where  $x_n, y_n \in \{1, -1\}$ . In noiseless condition, the cross-correlation between  $\{x_n\}$  and  $\{y_n\}$  is denoted by

$$C(m) = \sum_{k=0}^{N-1} x_{k+m} y_k \quad (4.3)$$

where  $m = 0, 1, \dots, N-1$ .

Let the code phase shift between  $S_{IN}$  and  $S_{LO}$  be  $q$ , where  $q \in \{0, 1, \dots, N-1\}$ . We first map the input and local sequences into phasors as given by

$$X = \sum_{n=0}^{N-1} x_n \gamma^{-n} \quad (4.4)$$

$$Y = \sum_{n=0}^{N-1} y_n \gamma^{-n} \quad (4.5)$$

where  $\gamma = e^{j\frac{2\pi}{N}}$  and  $j = \sqrt{-1}$ .

We then calculate

$$\begin{aligned} \Pi &= X^* \cdot Y \\ &= \left( \sum_{n=0}^{N-1} x_n \gamma^n \right) \cdot \left( \sum_{k=0}^{N-1} y_k \gamma^{-k} \right) \\ &= \left( \sum_{m=0}^{N-1} x_{k+m} \gamma^{k+m} \right) \cdot \left( \sum_{k=0}^{N-1} y_k \gamma^{-k} \right) \\ &= \sum_{m=0}^{N-1} \sum_{k=0}^{N-1} x_{k+m} y_k \gamma^m \\ &= \sum_{m=0}^{N-1} \gamma^m C(m). \end{aligned} \quad (4.6)$$

In order to present our concept in a direct and effective manner, the maximal-length sequence (MLS) is considered for sequence acquisition. The correlation between  $\{x_n\}$  and  $\{y_n\}$  is given by

$$C(m) = \begin{cases} N, & \text{if } m = q, \\ -1, & \text{if } m \neq q. \end{cases} \quad (4.7)$$

Hence, Eq. (4.6) becomes

$$\begin{aligned} \Pi &= \sum_{m=0}^{N-1} \gamma^m C(m) \\ &= C(q) \gamma^q + \sum_{m=0, m \neq q}^{N-1} \gamma^m C(m) \\ &= (N+1) \gamma^q - \sum_{m=0}^{N-1} \gamma^m \\ &= (N+1) \gamma^q \\ &= (N+1) e^{j\frac{2\pi}{N}q} \end{aligned} \quad (4.8)$$

where the equality  $\sum_{m=0}^{N-1} \gamma^m = 0$  is applied in the above derivation.

Let the phase of  $\Pi$  be  $\Psi$  as denoted by

$$\Psi = \frac{2\pi}{N} q. \quad (4.9)$$

The acquisition of the sequence can then be achieved by

$$q = \frac{N}{2\pi} \Psi. \quad (4.10)$$

Since the input sequence consists of  $+1$  and  $-1$ , the complex phasor of Eq. (4.4) is obtained by simply  $N$  additions (subtractions). Note that the computations of the phasor regarding the local sequence can be omitted by calculating Eq. (4.5) in advance.

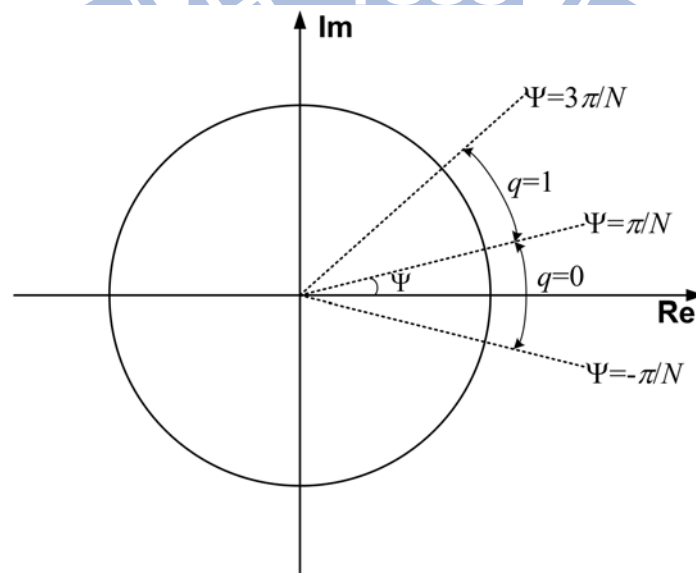


Fig. 4.1. Schematic plot of the phase resolution for phasors on the complex domain.

In the above derivation, when the phasor of the input sequence is obtained by Eq. (4.4), very few computations are needed to determine the shift  $q$ , much fewer than those required in the FFT-based approach. However, the phase accuracy of the complex phasor is sensitive to noise. The phase resolution is  $2\pi/N$  according to Eq. (4.9). As shown in Fig. 4.1, when  $N$  is large, the distance between adjacent phases is rather small which can easily lead to errors in phase estimation under a noisy environment. Hence, it becomes necessary to design an algorithm that permits the distance between adjacent phases to be increased, so as to resist the affect of noise.

### 4.3 Phase Coherence Acquisition Algorithm

#### 4.3.1 Segmentation

Suppose the input sequence  $S_{IN}$  has the length of  $N = K \cdot M$ . In the PCA,  $S_{IN}$  is first partitioned into  $K$  disjointed segments of length  $M$  as denoted by

$$\begin{aligned}
 \mathbf{A}_0 &= \{x_0, x_K, x_{2K}, \dots, x_{(M-1)K}\} \\
 \mathbf{A}_1 &= \{x_1, x_{K+1}, x_{2K+1}, \dots, x_{(M-1)K+1}\} \\
 &\vdots \\
 \mathbf{A}_{K-1} &= \{x_{K-1}, x_{2K-1}, x_{3K-1}, \dots, x_{MK-1}\} \\
 &= \{x_{K-1}, x_{2K-1}, x_{3K-1}, \dots, x_{N-1}\}.
 \end{aligned} \tag{4.11}$$

Similarly, the local sequence  $S_{LO}$  is also partitioned into  $K$  disjointed segments as below:

$$\begin{aligned}
 \mathbf{B}_0 &= \{y_0, y_K, y_{2K}, \dots, y_{(M-1)K}\} \\
 \mathbf{B}_1 &= \{y_1, y_{K+1}, y_{2K+1}, \dots, y_{(M-1)K+1}\} \\
 &\vdots \\
 \mathbf{B}_{K-1} &= \{y_{K-1}, y_{2K-1}, y_{3K-1}, \dots, y_{MK-1}\} \\
 &= \{y_{K-1}, y_{2K-1}, y_{3K-1}, \dots, y_{N-1}\}.
 \end{aligned} \tag{4.12}$$

Suppose the code phase shift between the input and the local sequences is  $q = cK + d$ , where  $0 \leq c < M$  and  $0 \leq d < K$ . We then have  $y_i = x_{i+q} = x_{i+cK+d}$  and the following relationships:

$$\begin{aligned}
\mathbf{B}_0 &= \{y_0, y_K, y_{2K}, \dots, y_{(M-1)K}\} \\
&= \{x_{cK+d}, x_{(c+1)K+d}, \dots, x_{(M-1)K+d}, x_d, \dots, x_{(c-1)K+d}\} \\
&= \mathbf{A}_d(c) \\
\mathbf{B}_1 &= \mathbf{A}_{d+1}(c) \\
&\vdots \\
\mathbf{B}_{K-d-1} &= \mathbf{A}_{K-1}(c)
\end{aligned} \tag{4.13}$$

where  $\mathbf{A}_d(c)$  denotes the circular shift of  $\mathbf{A}_d$  with  $c$  chips to left.

Note that the remaining  $\mathbf{B}_{K-d}, \mathbf{B}_{K-d+1}, \dots, \mathbf{B}_{K-1}$  can be derived by using the same logics but with adjustments as given by

$$\begin{aligned}
\mathbf{B}_{K-d} &= \{y_{K-d}, y_{2K-d}, y_{3K-d}, \dots, y_{MK-d}\} \\
&= \{x_{(K-d)+cK+d}, x_{(2K-d)+cK+d}, \dots, x_{MK+d+cK+d}\} \\
&= \{x_{(c+1)K}, x_{(c+2)K}, \dots, x_0, \dots, x_{cK}\} \\
&= \mathbf{A}_0(c+1) \\
\mathbf{B}_{K-d+1} &= \mathbf{A}_1(c+1) \\
&\vdots \\
\mathbf{B}_{K-1} &= \mathbf{A}_{d-1}(c+1).
\end{aligned} \tag{4.14}$$

From Eq. (4.13) and Eq. (4.14), the relationships between  $\mathbf{A}_i$  and  $\mathbf{B}_i$  can be generalized as follows:

$$\begin{aligned}
\mathbf{B}_i &= \mathbf{A}_{d+i}(c), & 0 \leq i \leq K-d-1 \\
&= \mathbf{A}_{(d+i) \bmod K}(c+1), & K-d \leq i \leq K-1.
\end{aligned} \tag{4.15}$$



### 4.3.2 Acquisition by phase

In each segment of Eq. (4.11) and Eq. (4.12), we map the sequences into the complex phasors by

$$X_i = \sum_{n=0}^{M-1} x_{nK+i} \alpha^{-n} \quad (4.16)$$

$$Y_i = \sum_{n=0}^{M-1} y_{nK+i} \alpha^{-n} \quad (4.17)$$

where  $\alpha = e^{j\frac{2\pi}{M}}$  and  $i = 0, 1, 2, \dots, K-1$ .

Let  $A_i(m)$  be the segment  $A_i$  with  $m$  circular shifts to left, denoted by

$$A_i(m) = \{x_{mK+i}, x_{(m+1)K+i}, \dots, x_i, \dots, x_{(m-1)K+i}\}. \quad (4.18)$$

Accordingly, the complex phasor pertaining to  $A_i(m)$  is given by

$$\begin{aligned} X_i(m) &= \sum_{n=0}^{M-1} x_{(m+n)K+i} \alpha^{-n} \\ &= \sum_{n=0}^{M-1} x_{(m+n)K+i} \alpha^{-(m+n)} \cdot \alpha^m \\ &= \alpha^m \sum_{u=0}^{M-1} x_{uK+i} \alpha^{-u} \\ &= \alpha^m X_i. \end{aligned} \quad (4.19)$$

According to Eq. (4.19) and Eq. (4.15), the complex phasors  $Y_i$  are derived by

$$\begin{aligned} Y_i &= \alpha^c \cdot X_{d+i} \\ &= e^{j\frac{2\pi}{M}c} \cdot X_{d+i}, \quad 0 \leq i \leq K-d-1 \end{aligned} \quad (4.20)$$

$$\begin{aligned}
Y_i &= \alpha^{c+1} \cdot X_{d+i} \\
&= e^{j\frac{2\pi}{M}(c+1)} \cdot X_{d+i}, \quad K-d \leq i \leq K-1.
\end{aligned} \tag{4.21}$$

Furthermore, the complex phasors  $X_i$  and  $Y_i$  can be expressed by

$$X_i = |X_i| e^{j\theta_i} \tag{4.22}$$

$$Y_i = |Y_i| e^{j\phi_i} \tag{4.23}$$

where  $\theta_i$  and  $\phi_i$  denote the phases of  $X_i$  and  $Y_i$ , respectively.

From Eq. (4.20) to Eq. (4.23), we have the following phase relationship:

$$\begin{aligned}
\phi_i &= \theta_{i+d} + \frac{2\pi}{M} \cdot c, \quad 0 \leq i \leq K-d-1 \\
&= \theta_{i+d} + \frac{2\pi}{M} \cdot (c+1), \quad K-d \leq i \leq K-1.
\end{aligned} \tag{4.24}$$

Let  $G_m$  be the sum of the  $K$  complex phasors, defined as

$$G_m = \sum_{i=0}^{K-m-1} e^{j(\phi_i - \theta_{i+m})} + \sum_{i=K-m}^{K-1} e^{j(\phi_i - \theta_{i+m} - \frac{2\pi}{M})} \tag{4.25}$$

where  $m = 0, 1, 2, \dots, K-1$ .

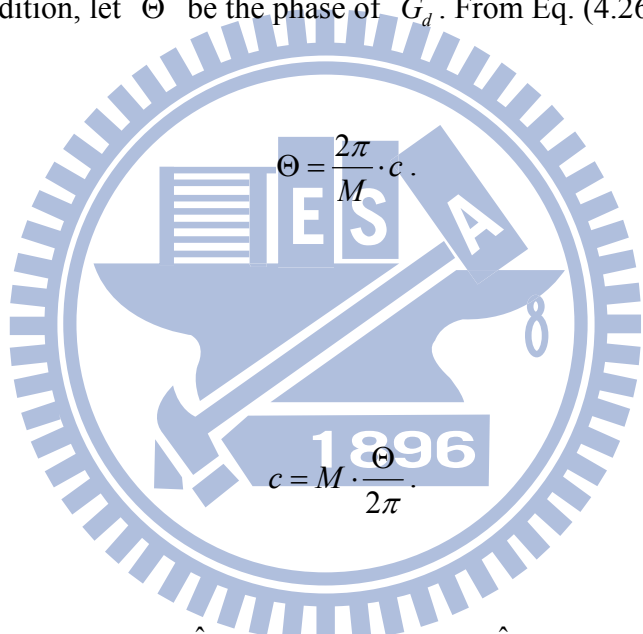
According to the relationship in Eq. (4.24), when  $m = d$ , we have

$$\begin{aligned}
G_d &= \sum_{i=0}^{K-m-1} e^{j(\phi_i - \theta_{i+d})} + \sum_{i=K-m}^{K-1} e^{j(\phi_i - \theta_{i+d} - \frac{2\pi}{M})} \\
&= \sum_{i=0}^{K-m-1} e^{j\frac{2\pi}{M}c} + \sum_{i=K-m}^{K-1} e^{j\frac{2\pi}{M}c} \\
&= K \cdot e^{j\frac{2\pi}{M}c}.
\end{aligned} \tag{4.26}$$

Apparently,

$$|G_d| = K. \quad (4.27)$$

Note that we have a peak magnitude given by Eq. (4.27) when the  $K$  complex phasors are coherently added for  $G_d$ . On the other hand, when  $m \neq d$ ,  $G_m$  is the sum of the  $K$  phasors of non-coherent phases, and the resultant magnitude would be expected to be much smaller than  $K$ . Hence, the value of  $d$  can be obtained by finding the peak magnitude among  $\{|G_m|\}$ . In addition, let  $\Theta$  be the phase of  $G_d$ . From Eq. (4.26), we have

$$\Theta = \frac{2\pi}{M} \cdot c. \quad (4.28)$$


Thus  $c$  is given by

$$c = M \cdot \frac{\Theta}{2\pi}. \quad (4.29)$$

Let the estimates of  $(c, d)$  be  $(\hat{c}, \hat{d})$ . Practically, when  $\hat{d} = d$  and  $\hat{c}$  is equal to  $c$ , the shift  $q = \hat{c}K + \hat{d}$  can be determined correctly.

In PCA, the input sequence is one-bit quantized, partitioned and transformed into phasors as given by Eq. (4.16). The phase differences between phasors of the input and local sequences are then utilized for the acquisition as given by Eq. (4.25). When the phase differences between phasors are coherently added, we can have a large peak ( $|G_d|$ ) to determine the correct segment for code phase acquisition. These processes simply require complex additions and eliminate the need for complex multiplications which are the major advantages

of the PCA method. The segmentation process confers noise-robustness in the PCA method since the distance between adjacent phases is enlarged from  $2\pi/N$  to  $2\pi/M$  as compared to Eq. (4.9) with Eq. (4.28). The acquisition by phase thus becomes more robust to noise. However, the estimated  $(\hat{c}, \hat{d})$  could be erroneous when the SNR is very low, especially  $\hat{c}$ . In such situations, the multi-layer scheme can be applied to enhance noise resistance in the PCA method.

### 4.3.3 Multi-layer PCA

In the multi-layer PCA, the 1<sup>st</sup>-layer process is identical to the method described above. First, the input and local sequences of length  $N$  are partitioned into  $K_1$  segments of length  $M_1$ , where  $N = K_1 M_1$ . Assume the shift is denoted as  $q = c_1 K_1 + d_1$ . In the 1<sup>st</sup>-layer, only  $d_1$  is estimated by finding the peak of  $|G_m^{(1)}|$  in Eq. (4.25), and  $c_1$  is left undetermined owing to the sensitivity to the effect of noise. Note that the superscripts “(1)” and “(2)” in  $G_m$  indicate the 1<sup>st</sup>-layer and the 2<sup>nd</sup>-layer, respectively. After completion of the 1<sup>st</sup>-layer, we assume  $\hat{d}_1 = d_1$  and

$$\begin{aligned} \mathbf{B}_i &= \mathbf{A}_{\hat{d}_1+i}(c_1), & 0 \leq i \leq K_1 - \hat{d}_1 - 1 \\ &= \mathbf{A}_{\hat{d}_1+i}(c_1 + 1), & K_1 - \hat{d}_1 \leq i \leq K_1 - 1 \end{aligned} \quad (4.30)$$

where  $c_1$  is still undetermined.

We rewrite Eq. (4.30) by

$$\mathbf{B}_i = \mathbf{A}'_{\hat{d}_1+i}(c_1), \quad 0 \leq i \leq K_1 - 1 \quad (4.31)$$

where

$$\mathbf{A}'_{\hat{d}_1+i}(c_1) = \begin{cases} \mathbf{A}_{\hat{d}_1+i}(c_1), & 0 \leq i \leq K_1 - \hat{d}_1 - 1 \\ \mathbf{A}_{\hat{d}_1+i}(c_1 + 1), & K_1 - \hat{d}_1 \leq i \leq K_1 - 1. \end{cases}$$

From Eq. (4.31), all of the pairs of  $(\mathbf{A}'_{\hat{a}_i}, \mathbf{B}_i)$  have the same shift of  $c_1$  chips between them, which is the key for the following derivation in the 2<sup>nd</sup>-layer.

The process of the 2<sup>nd</sup>-layer is next introduced. For simplicity, the pair  $(\mathbf{A}'_{\hat{a}_1}, \mathbf{B}_0)$  is taken as an example, where each  $\mathbf{A}'_{\hat{a}_1}$  and  $\mathbf{B}_0$  contains  $M_1$  elements and their relative shift is  $c_1$ , i.e.  $\mathbf{B}_0 = \mathbf{A}'_{\hat{a}_1}(c_1)$ . Let  $M_1 = K_2 \cdot M_2$  and assume  $c_1 = c_2 K_2 + d_2$ , where  $0 \leq c_2 \leq M_2$  and  $0 \leq d_2 \leq K_2$ . First,  $\mathbf{A}'_{\hat{a}_1}$  and  $\mathbf{B}_0$  are partitioned into  $K_2$  disjointed segments of length  $M_2$  as before. The two-layer segmentation scheme in PCA is illustrated in Fig 4.2. Note that the elements of Segment  $\mathbf{A}_0$  are further denoted by  $u_i$ ,  $i = 0, 1, \dots, M_1 - 1$  in Fig 4.2(b). Each of the 1<sup>st</sup>-layer segments will be further partitioned like that in Fig. 4.2(b) in the 2<sup>nd</sup>-layer. Following the same calculation as Eq. (4.25), the sum of the  $K_2$  complex phasors is obtained for  $(\mathbf{A}'_{\hat{a}_1}, \mathbf{B}_0)$ , given as

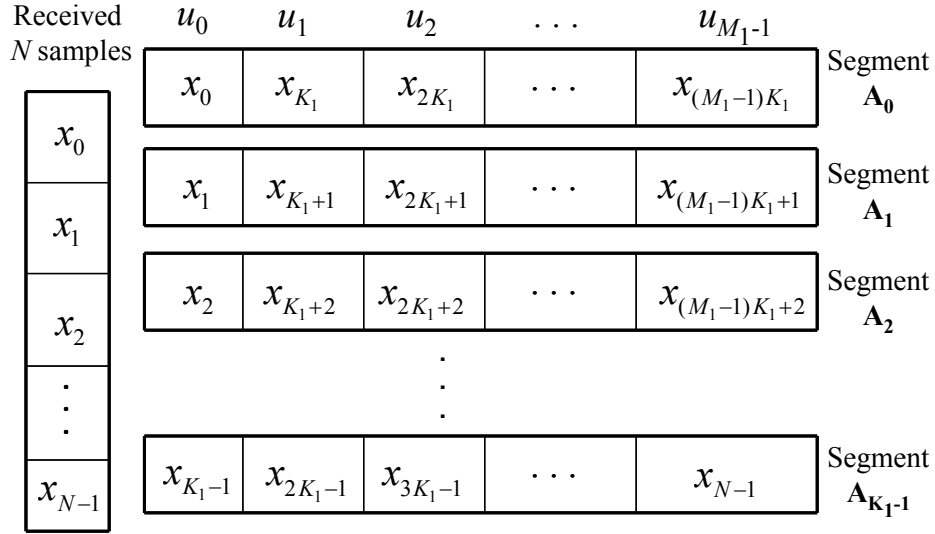
$$H_{r,0} = \sum_{s=0}^{K_2-r-1} e^{j(\phi'_s - \theta'_{s+r})} + \sum_{s=K_2-r}^{K_2-1} e^{j(\phi'_s - \theta'_{s+r} - \frac{2\pi}{M_2})} \quad (4.32)$$

where  $r = 0, 1, \dots, K_2 - 1$  and  $(\phi'_s, \theta'_s)$  are the corresponding phases involved in the calculation. When  $r = d_2$ , we have  $H_{d_2,0} = K_2 \cdot e^{j\frac{2\pi}{M_2}c_2}$  under the noiseless condition, which has the maximum magnitude among  $\{H_{r,0}\}$ .

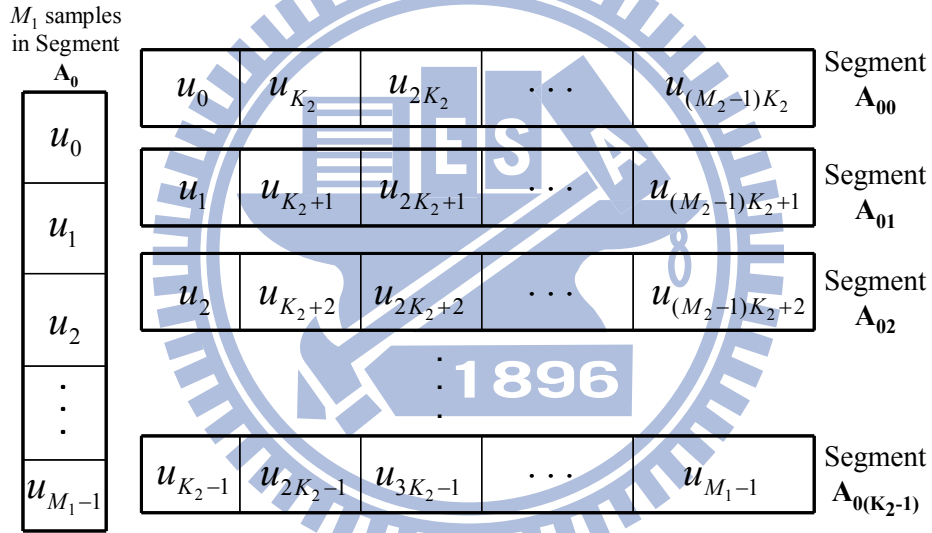
When the similar calculation is applied to the other pairs  $(\mathbf{A}'_{\hat{a}_{i+1}}, \mathbf{B}_i)$ ,  $i = 1, 2, \dots, K_1 - 1$ , their associated  $H_{r,i}$  can then be obtained. Afterwards, all of the  $H_{r,i}$ 's are used to calculate

$$G_r^{(2)} = \sum_{i=0}^{K_1-1} H_{r,i} \quad (4.33)$$

where  $r = 0, 1, \dots, K_2 - 1$ .



(a)



(b)

Fig. 4.2. Schematic plot of two-layer segmentation: (a) segmentation in the 1<sup>st</sup>-layer; (b) segmentation of segment  $\mathbf{A}_0$  in the 2<sup>nd</sup>-layer.

Since all the pairs  $(\mathbf{A}'_{\hat{a}_i+i}, \mathbf{B}_i)$  have the same shift of  $c_1$  chips in between and  $c_1 = c_2 K_2 + d_2$ ,  $G_{d_2}^{(2)}$  will have a peak magnitude among  $\{G_r^{(2)}\}$ . Specifically, in noiseless condition, we have

$$\begin{aligned}
G_{d_2}^{(2)} &= \sum_{i=0}^{K_1-1} H_{d_2,i} \\
&= \sum_{i=0}^{K_1-1} K_2 \cdot e^{j \frac{2\pi}{M_2} c_2} \\
&= K_1 K_2 \cdot e^{j \frac{2\pi}{M_2} c_2}
\end{aligned} \tag{4.34}$$

where the peak magnitude is  $K_1 K_2$ .

Similar to the 1<sup>st</sup>-layer, by finding the peak magnitude among  $\{|G_r^{(2)}|\}$ , we can estimate  $d_2$ , which is denoted by  $\hat{d}_2$ . Let  $\Phi$  be the phase of  $G_{\hat{d}_2}^{(2)}$  as given by

$$\Phi = \frac{2\pi}{M_2} \cdot c_2. \tag{4.35}$$

Similar to Eq. (4.29), the estimate of  $c_2$ , denoted by  $\hat{c}_2$ , is obtained by

$$\hat{c}_2 = M_2 \cdot \frac{\Phi}{2\pi}. \tag{4.36}$$

Note that the separation between adjacent phases is further enlarged from  $2\pi/M_1$  to  $2\pi/M_2$  according to Eq. (4.35), which results in the significant increase in noise resistance. Note that  $c_2$  can also be left undetermined after the 2<sup>nd</sup>-layer and determined by the 3<sup>rd</sup>-layer, if necessary. Nevertheless, from our simulation results, two layers appear to be sufficient for most applications. Finally, the estimate of  $q$ , denoted as  $\hat{q}$ , is calculated as

$$\begin{aligned}
\hat{q} &= \hat{c}_1 K_1 + \hat{d}_1 \\
&= (\hat{c}_2 K_2 + \hat{d}_2) K_1 + \hat{d}_1.
\end{aligned} \tag{4.37}$$

#### 4.3.4 Error detection capability

When the segment of the 1<sup>st</sup>-layer is correctly estimated, i.e.  $\hat{d}_1 = d_1$ , we obtain a much

larger peak in the 2<sup>nd</sup>-layer for  $\hat{d}_2 = d_2$ . Taking the noiseless case for example, we have the peak of  $K_1$  in  $|G_{d_1}^{(1)}|$  according to Eq. (4.26). In contrast, a much larger peak of  $K_1K_2$  is obtained from  $|G_{d_2}^{(2)}|$  using Eq. (4.34). As a result, the existence of a significant peak in  $|G_r^{(2)}|$  of the 2<sup>nd</sup>-layer can be used to verify the correctness of  $\hat{d}_1$ , which shows the inherent error detection capability of PCA. Accordingly, the correct  $\hat{d}_1$  can be obtained with some recursive algorithms by utilizing such error detection properties and the performance of the multi-layer PCA can be further improved. This special feature has been verified in our simulations. The processes of two-layer PCA are illustrated in Fig. 4.3.

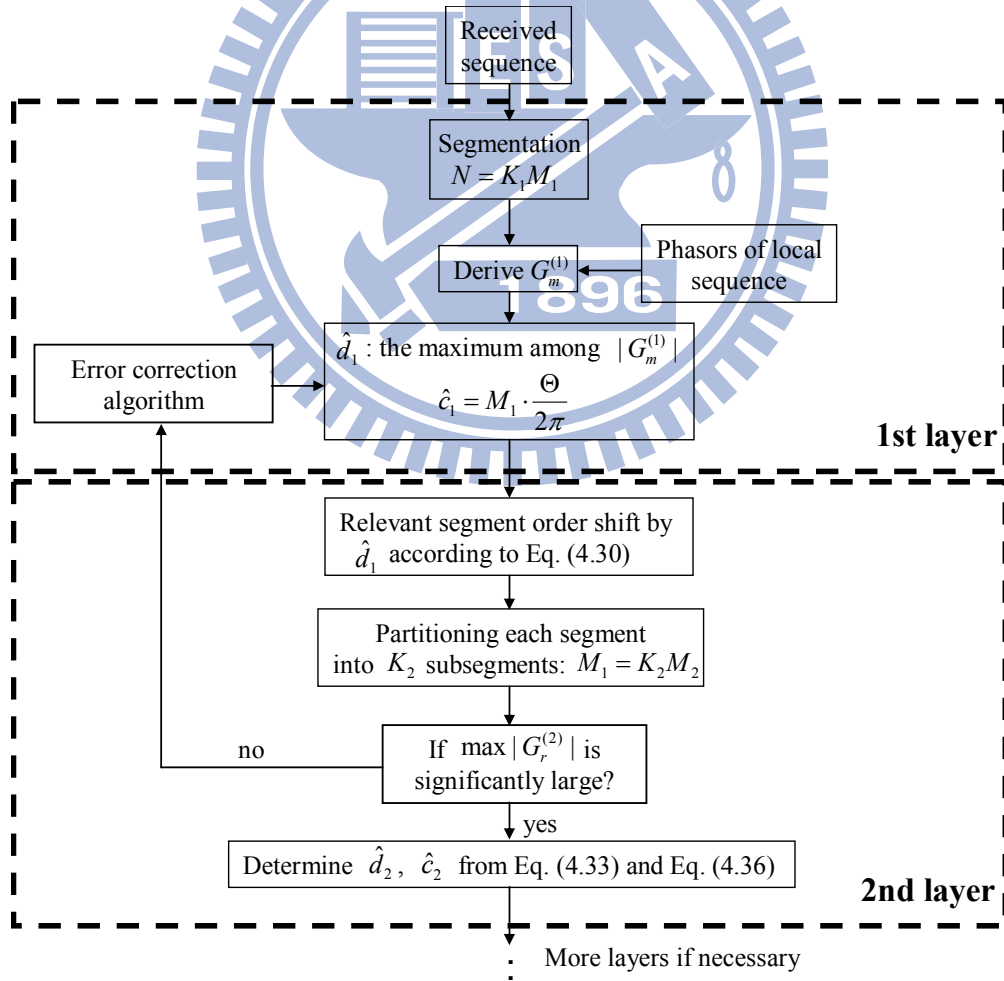


Fig. 4.3. Flow chart of the process of two-layer PCA.



## 4.4 Performance of PCA

Let the input PN sequence be  $\{x_n\}$ . Assume the sequence is distorted by zero-mean Gaussian noise  $\zeta_n$  with variance  $\sigma_\zeta^2$ , and is one-bit quantized as denoted by

$$w_n = \text{sign}(x_n + \zeta_n) \quad (4.38)$$

where  $n = 0, 1, \dots, N-1$ ,  $\text{sign}(z) = 1$  if  $z \geq 0$  and  $\text{sign}(z) = -1$  if  $z < 0$ .

In the 1<sup>st</sup>-layer, the input and local sequences,  $\{w_n\}$  and  $\{y_n\}$ , are partitioned into  $K_1$  segments of length  $M_1$ , as denoted by

$$\mathbf{A}_i = \{w_i, w_{K_1+i}, w_{2K_1+i}, \dots, w_{(M-1)K_1+i}\} \quad (4.39)$$

$$\mathbf{B}_i = \{y_i, y_{K_1+i}, y_{2K_1+i}, \dots, y_{(M-1)K_1+i}\} \quad (4.40)$$

where  $i = 0, 1, \dots, K_1 - 1$ .

Similar to Eq. (4.16) and Eq. (4.17), the complex phasors are defined by

$$\begin{aligned} W_i &= \sum_{n=0}^{M_1-1} w_{nK_1+i} \alpha^{-n} \\ &= |W_i| e^{j\theta_i} \end{aligned} \quad (4.41)$$

$$\begin{aligned} Y_i &= \sum_{n=0}^{M_1-1} y_{nK_1+i} \alpha^{-n} \\ &= |Y_i| e^{j\phi_i}. \end{aligned} \quad (4.42)$$

Moreover, according to Eq. (4.25), the sum of complex phasors is given by

$$\begin{aligned}
G_m^{(1)} &= \sum_{i=0}^{K_1-m-1} e^{j(\phi_i - \theta_{i+m})} + \sum_{i=K_1-m}^{K_1-1} e^{j(\phi_i - \theta_{i+m} - \frac{2\pi}{M_1})} \\
&= \sum_{i=0}^{K_1-1} e^{j\psi_{i,m}}
\end{aligned} \tag{4.43}$$

where  $\psi_{i,m}$  denotes the phase difference between the complex phasors  $W_{i+m}$  and  $Y_i$ ,  $-\pi \leq \psi_{i,m} \leq \pi$  and  $m = 0, 1, \dots, K_1$ .

Let the shift between  $\{w_n\}$  and  $\{y_n\}$  be  $q = c_1 K_1 + d_1$ . As derived in the Appendix C, the magnitude of  $|G_m^{(1)}|$  with  $m \neq d_1$ , i.e. the sidelobe, is a random variable with the Rayleigh distribution given by

$$f(r_s) = \frac{r_s}{K_1/2} e^{-r_s^2/K_1} \tag{4.44}$$

where  $f(r_s)$  is the probability density function of  $|G_m^{(1)}|$  and  $r_s \geq 0$ .

In addition,  $|G_m^{(1)}|$  with  $m = d_1$ , i.e.  $|G_{d_1}^{(1)}|$ , has the Rice distribution given by

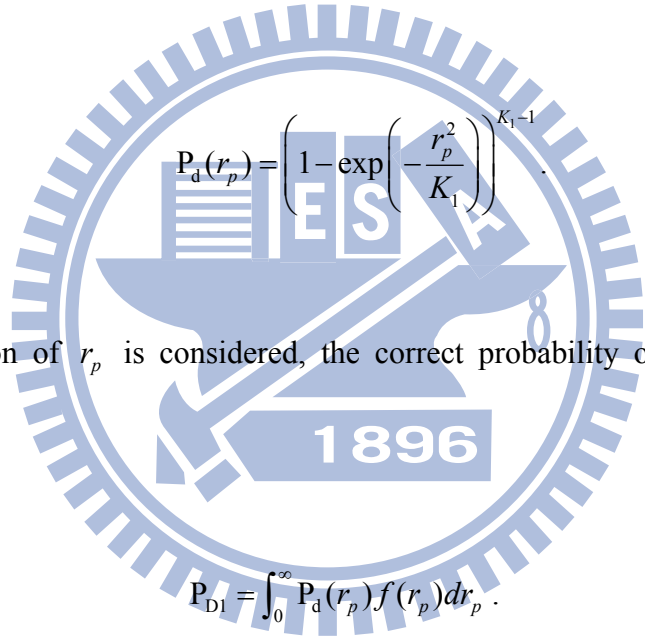
$$f(r_p) = \frac{r_p}{\sigma_{p1}^2} e^{-(r_p^2 + \mu_{\text{Re1}}^2)/2\sigma_{p1}^2} \cdot I_0\left(\frac{r_p \mu_{\text{Re1}}}{\sigma_{p1}^2}\right) \tag{4.45}$$

where  $r_p \geq 0$ .

For a given  $r_p$ , the probability of  $r_p > r_s$  is denoted by

$$\begin{aligned}
\Pr(r_p > r_s) &= \int_0^{r_p} f(r_s) dr_s \\
&= \int_0^{r_p} \frac{2r_s}{K_1} \exp\left(-\frac{r_s^2}{K_1}\right) dr_s \\
&= 1 - \exp\left(-\frac{r_p^2}{K_1}\right).
\end{aligned} \tag{4.46}$$

Because there are  $K_1 - 1$  sidelobes in the  $G_m^{(1)}$ , the correct  $d_l$  is obtained when  $|G_{d_l}^{(1)}|$  is greater than all of the other  $K_1 - 1$  sidelobes. Hence, for a given  $r_p$ , the correct probability of detecting  $d_l$  is given by

$$P_d(r_p) = \left(1 - \exp\left(-\frac{r_p^2}{K_1}\right)\right)^{K_1-1}. \tag{4.47}$$


When the distribution of  $r_p$  is considered, the correct probability of  $d_l$ , i.e.  $\hat{d}_1 = d_1$ , is denoted by

$$P_{D1} = \int_0^\infty P_d(r_p) f(r_p) dr_p. \tag{4.48}$$

Furthermore, the probability of correct  $c_1$  shall be considered for the correct acquisition in the one-layer PCA. According to Eq. (4.29),  $c_1$  is obtained from the phase of  $G_{d_1}^{(1)}$  and, thus, the probability of detecting  $c_1$  can be derived in light of the phase distribution of  $G_{d_1}^{(1)}$ . Specifically, let the phase of  $G_{d_1}^{(1)}$  be  $\varphi$ . For simplicity, assume  $c_1 = 0$ . According to the schematic concept shown in Fig. 4.1,  $c_1$  is correct if  $|\varphi| \leq \frac{\pi}{M_1}$ . Utilizing the joint magnitude and phase distribution of  $G_{d_1}^{(1)}$  derived in the Appendix C, we have

$$f(r_p, \varphi) = \frac{r_p}{2\pi\sigma_{p1}^2} \exp\left(-\frac{r_p^2 + \mu_{\text{Re1}}^2 - 2r_p\mu_{\text{Re1}} \cos \varphi}{2\sigma_{p1}^2}\right) \quad (4.49)$$

where  $-\pi \leq \varphi < \pi$ .

The joint probability of the correct  $d_1$  and  $c_1$  is then denoted by

$$\begin{aligned} P_{C1} &= \Pr\left(\hat{d}_1 = d_1, \mid \varphi \mid \leq \frac{\pi}{M_1}\right) \\ &= \int_0^{\frac{\pi}{M_1}} \int_0^\infty P_d(r_p) f(r_p, \varphi) dr_p d\varphi. \end{aligned} \quad (4.50)$$

We use the MLS of length  $N = 2^{20} - 1$  to verify the analysis. Let  $K_1 = 2^{10} + 1$  and  $M_1 = 2^{10} - 1$ . The mentioned correct probabilities above are simulated by the Monte Carlo method with 10000 trials. The correct probabilities of  $P_{D1}$  and  $P_{C1}$  are shown in Fig. 4.4 and Fig. 4.5, respectively.

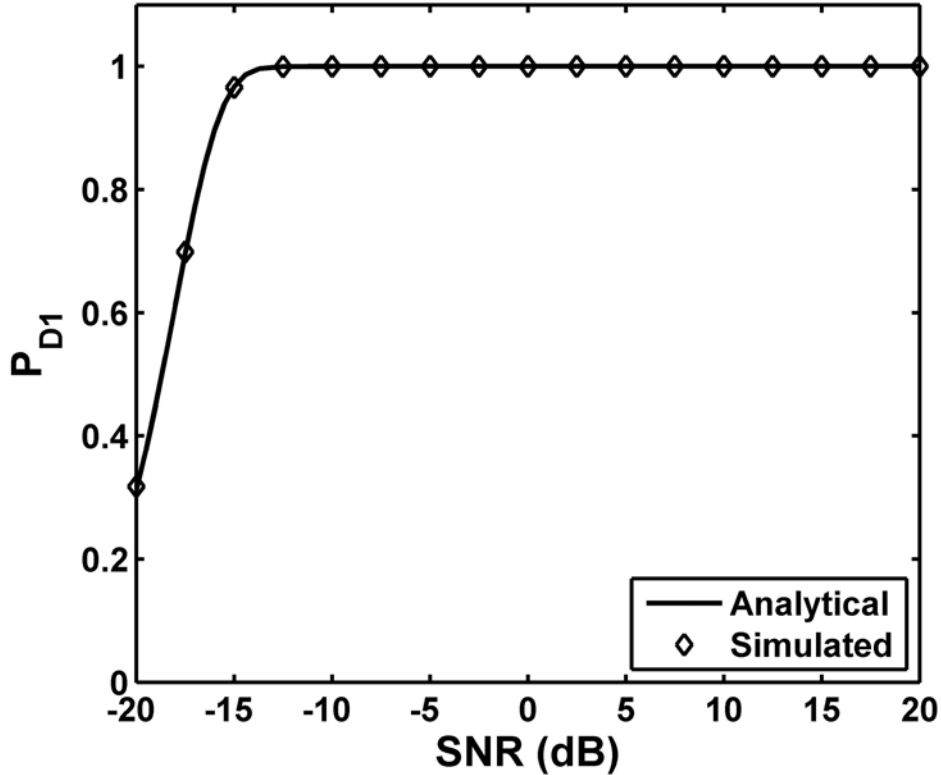


Fig. 4.4. Correct probability of  $d_1$  in the 1<sup>st</sup>-layer of PCA.

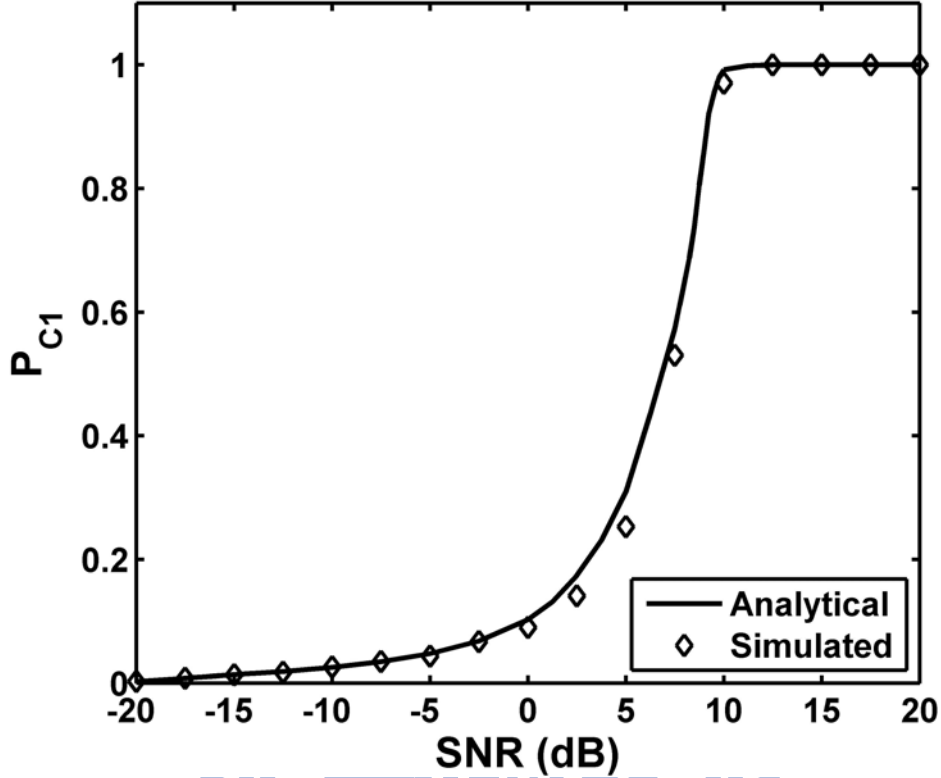


Fig. 4.5. Joint correct probability of  $d_1$  and  $c_1$  in the 1<sup>st</sup>-layer of PCA.

In both figures, the analytical and simulated results well agree with each other, which justifies the validity of our analysis. The correct probability of  $d_1$  approaches one when  $\text{SNR} > -15\text{dB}$  and begins to degrade with decreasing SNR. Note that the probability of  $d_1$  is critical to the PCA performance. The acquisition process will fail if  $d_1$ , i.e. the correct segment, cannot be correctly detected. On the other hand, the correct probability of  $P_{C1}$  is worse than  $P_{D1}$ , which approaches one when  $\text{SNR} > 10\text{dB}$  but drops to below 0.1 if  $\text{SNR} < 0\text{dB}$ . Besides the correct probability, the standard deviation (STD) of  $\hat{c}_1$  is also derived in order to study the deviation in code phase shift. We consider the STD of  $\hat{c}_1$  with the condition that  $\hat{d}_1 = d_1$ , which is denoted by

$$\sigma_\varphi = \left[ \frac{1}{P_{D1}} \int_{-\pi}^{\pi} \varphi^2 \cdot \int_0^\infty P_d(r_p) f(r_p, \varphi) dr_p d\varphi \right]^{1/2}. \quad (4.51)$$

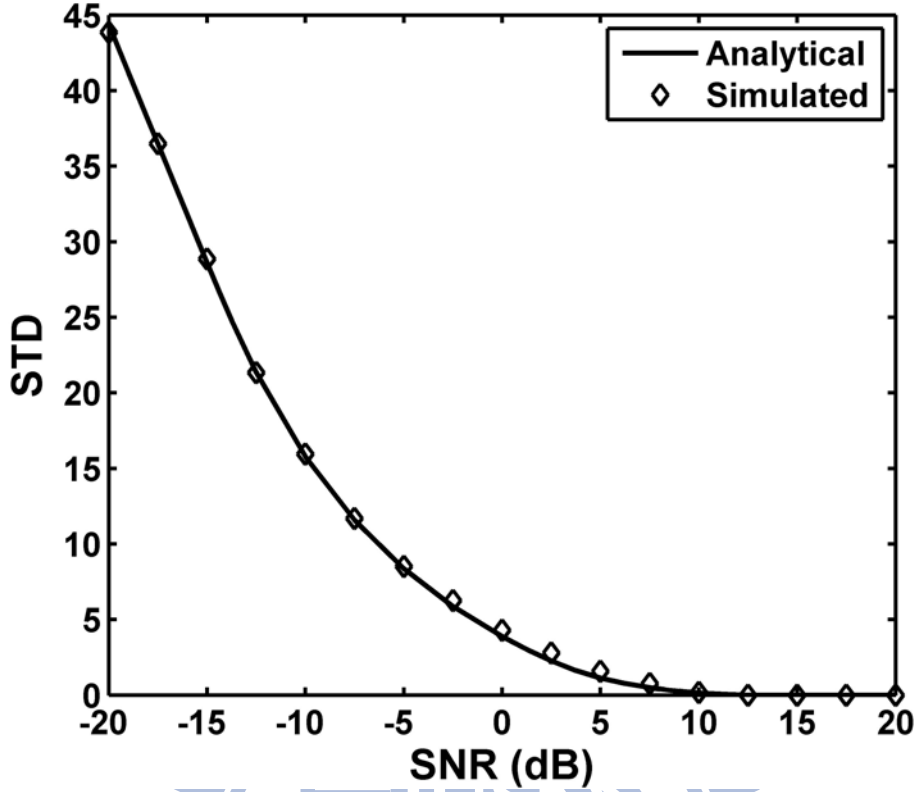


Fig. 4.6. STD of  $\hat{c}_1$  in the 1<sup>st</sup>-layer of PCA when  $\hat{d}_1 = d_1$ .

In Fig. 4.6, the STD decreases with SNR. Specifically, the STD of  $\hat{c}_1$  is about 4 chips when SNR = 0dB and decreases to within one chip for SNR  $\geq$  6dB. According to the STD of  $\hat{c}_1$ , the one-layer PCA performs well only in the case of the high SNR. For applications in low SNR, the 2<sup>nd</sup>-layer is needed to improve the performance of PCA.

Let  $M_1 = K_2 M_2$  and  $c_1 = c_2 K_2 + d_2$  in the 2<sup>nd</sup>-layer of PCA. According to Eq. (4.32) and Eq. (4.33), the sum of complex phasors is given by

$$\begin{aligned}
 G_n^{(2)} &= \sum_{i=0}^{K_1-1} \left( \sum_{t=0}^{K_2-n-1} e^{j(\phi_{i,t} - \theta_{i,t+n})} + \sum_{t=K_2-n}^{K_2-1} e^{j(\phi_{i,t} - \theta_{i,t+n} - \frac{2\pi}{M_2})} \right) \\
 &= \sum_{i=0}^{K_1-1} \sum_{t=0}^{K_2-1} e^{j\psi_{i,t+n}}
 \end{aligned} \tag{4.52}$$

where  $n = 0, 1, \dots, K_2$ .

For simplicity, we assume  $\hat{d}_1 = d_1$  for the analysis of the 2<sup>nd</sup>-layer. According to Appendix C, the magnitude distribution of the sidelobe of  $|G_n^{(2)}|$  with  $n \neq d_2$  is given by

$$f(l_s) = \frac{l_s}{K_1 K_2 / 2} e^{-l_s^2 / K_1 K_2} \quad (4.53)$$

where  $l_s \geq 0$ .

On the other hand, the magnitude distribution of  $|G_n^{(2)}|$  with  $n = d_2$  is denoted by

$$f(l_p) = \frac{l_p}{\sigma_{p2}^2} e^{-(l_p^2 + \mu_{Re2}^2) / 2\sigma_{p2}^2} \cdot I_0\left(\frac{l_p \mu_{Re2}}{\sigma_{p2}^2}\right) \quad (4.54)$$

where  $l_p \geq 0$ .

Similarly, for a given  $l_p$ , the correct probability of  $d_2$  is the probability that  $l_p$  is greater than all the other  $K_2 - 1$  sidelobes, which is denoted by

$$P_d(l_p) = \left(1 - \exp\left(-\frac{l_p^2}{K_1 K_2}\right)\right)^{K_2 - 1}. \quad (4.55)$$

Considering the distribution of  $l_p$ , the correct probability of  $d_2$ , i.e.  $\hat{d}_2 = d_2$ , is given by

$$P_{D2} = \int_0^\infty P_d(l_p) f(l_p) dl_p. \quad (4.56)$$

Furthermore, the joint distribution of the magnitude and phase of  $G_{d_2}^{(2)}$  is given by

$$f(l_p, \mathcal{G}) = \frac{l_p}{2\pi\sigma_{p^2}} \exp\left(-\frac{l_p^2 + \mu_{\text{Re}2}^2 - 2l_p\mu_{\text{Re}2} \cos \mathcal{G}}{2\sigma_{p^2}^2}\right) \quad (4.57)$$

where  $-\pi \leq \mathcal{G} \leq \pi$ .

Hence, the joint probability of the correct  $d_2$  and  $c_2$  is denoted by

$$P_{C_2} = \int_0^{\frac{\pi}{M_2}} \int_0^{\infty} P_d(l_p) f(l_p, \mathcal{G}) dl_p d\mathcal{G}. \quad (4.58)$$

The correct probabilities of  $P_{D_2}$  and  $P_{C_2}$  are shown in Fig. 4.7 and Fig. 4.8, respectively.

We use the same parameters for the 1<sup>st</sup>-layer and take  $K_2 = 2^5 + 1$  and  $M_2 = 2^5 - 1$  in the 2<sup>nd</sup>-layer. Still, the analytical results are consistent with the simulated values in both figures. The improvement brought by the 2<sup>nd</sup>-layer is significant, since the correct probability of  $d_2$  approaches one for SNR from  $-20$  to  $20$  dB in Fig. 4.7. Moreover, the joint correct probability of  $d_2$  and  $c_2$  is greater than 0.9 when  $\text{SNR} \geq -20$  dB in Fig. 4.8.

Similarly, the STD of  $\hat{c}_2$  with the condition that  $\hat{d}_2 = d_2$  is derived by

$$\sigma_{\mathcal{G}} = \left[ \frac{1}{P_{D_2}} \int_{-\pi}^{\pi} \mathcal{G}^2 \cdot \int_0^{\infty} P_d(l_p) f(l_p, \mathcal{G}) dl_p d\mathcal{G} \right]^{1/2}. \quad (4.59)$$

In Fig.4.9, the STD is much less than one chip for  $\text{SNR} \geq -20$  dB and approaches zero when  $\text{SNR} \geq 5$  dB. The noise-robustness of the multi-layer PCA is thus verified, especially in the case of low SNR, comparing Fig. 4.6 with Fig. 4.9. Note that the performance of PCA is actually related to the chip error probability. Hence, the varying SNR due to fading in the long PN sequence will not significantly degrade the performance of PCA. The non-uniform SNR can be approximated by a nominal SNR, which is associated with the actual chip error probability of the sequence, such that our analysis is still applicable.



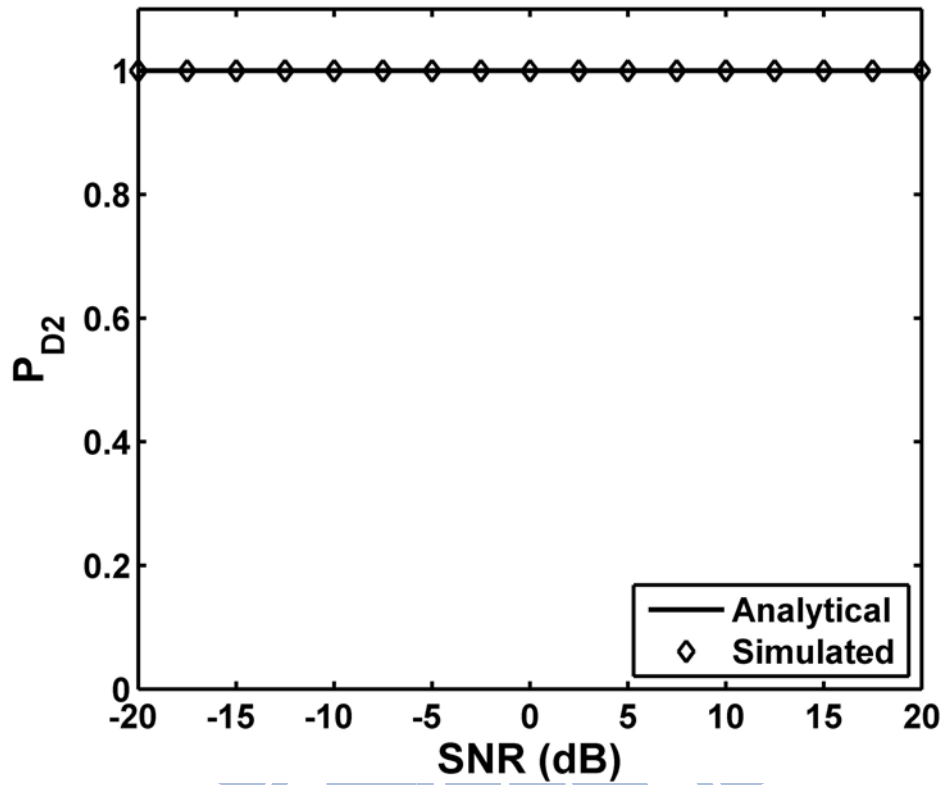


Fig. 4.7. Correct probability of  $d_2$  in the 2<sup>nd</sup>-layer of PCA.

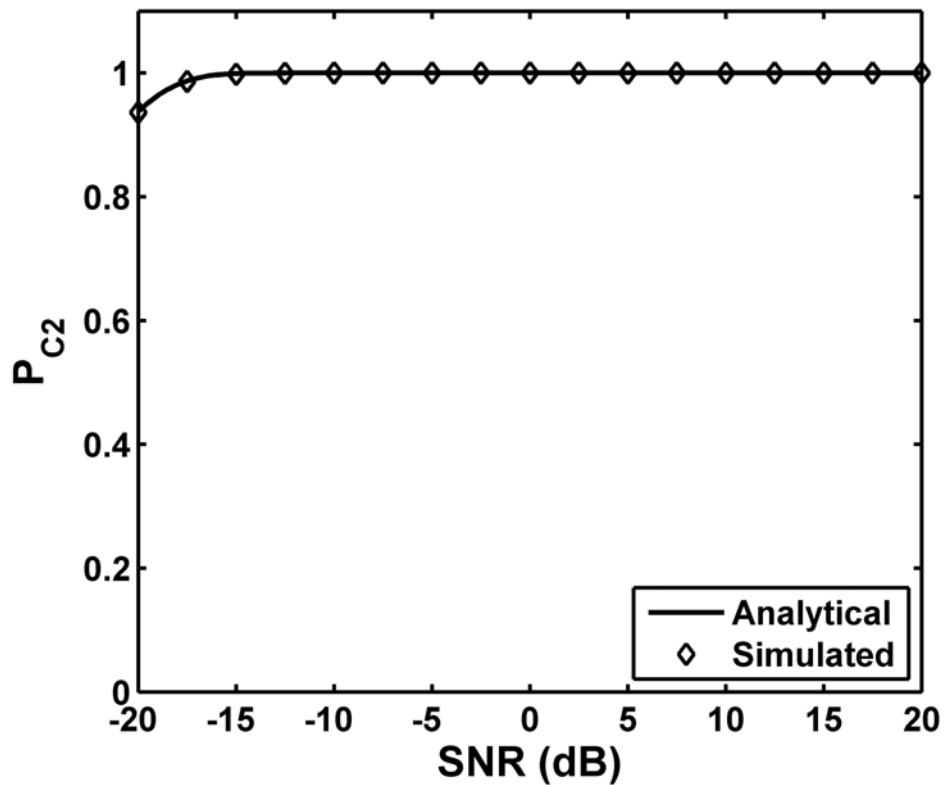


Fig. 4.8. Joint correct probability of  $d_2$  and  $c_2$  in the 2<sup>nd</sup>-layer of PCA.

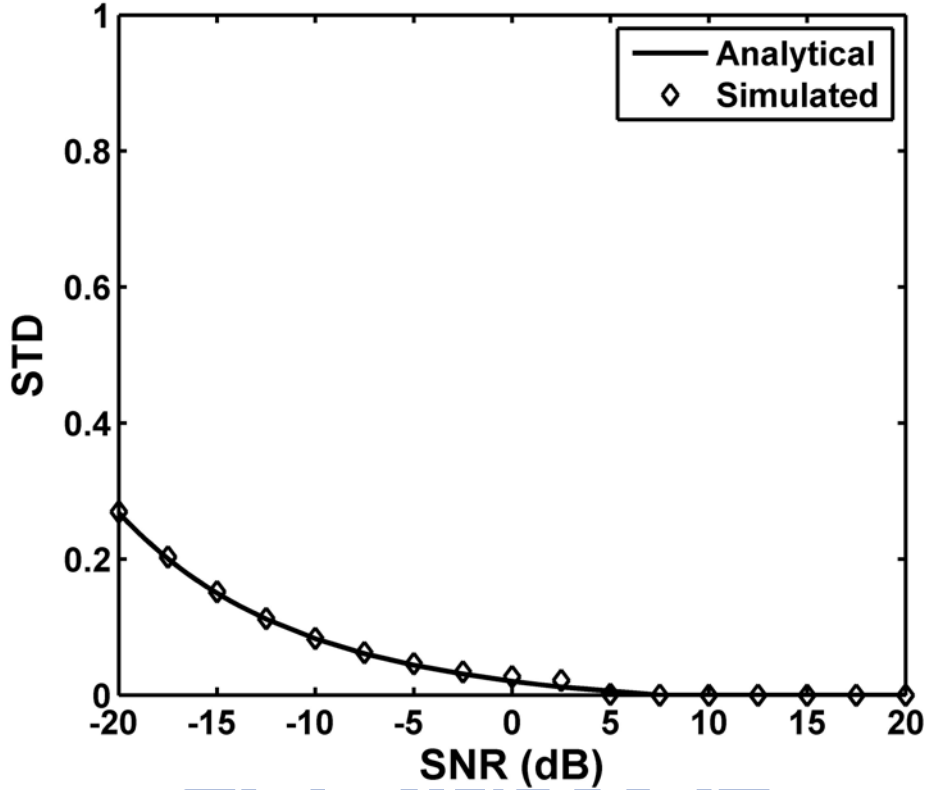


Fig. 4.9. STD of  $\hat{c}_2$  in the 2<sup>nd</sup>-layer of PCA when  $\hat{d}_2 = d_2$ .

## 4.5 Computation of PCA

The computation of PCA is studied and compared with that of FFT-based acquisition. Here we assume that the computations regarding the local sequence are omitted, since it can be calculated in advance. For the 1<sup>st</sup>-layer process of PCA, the derivation of the phasors of the input sequence as shown in Eq. (4.16) requires  $K_1 \cdot (M_1 - 1)$  additions. In addition, the calculation of  $G_m^{(1)}$  in Eq. (4.25) requires  $K_1 \cdot K_1$  additions (subtractions) for phase difference and  $K_1(K_1 - 1)$  additions for the sum of phasors. Regarding the computation of the complex phase in Eq. (4.22), CORDIC computing using shifts and additions can be utilized [54]. In CORDIC, let  $P_1$  denote the parameter associated with the required phase resolution in the 1<sup>st</sup>-layer, i.e.  $\tan^{-1} \frac{1}{2^{P_1}} \leq \frac{2\pi}{M_1}$  for Eq. (4.28). For example, when  $P_1 = 8$ , the phase resolution is sufficient for  $M_1 = 2^{10} - 1$ . As a result,  $3K_1P_1$  additions are needed for

computing the complex phases in Eq. (4.22). Hence, the overall addition in the 1<sup>st</sup>-layer is  $K_1 \cdot (M_1 + 2K_1 - 2 + 3P_1)$ . For the 2<sup>nd</sup>-layer process,  $K_1K_2 \cdot (M_2 - 1)$  additions are needed for the input phasor, and  $K_1 \cdot K_2^2 + K_1K_2(K_2 - 1)$  additions for computing Eq. (4.32) and Eq. (4.33). In addition, assume that the required phase resolution in the 2<sup>nd</sup>-layer is  $\tan^{-1} \frac{1}{2^{P_2}} \leq \frac{2\pi}{M_2}$ , we then need  $3K_1K_2P_2$  additions for the complex phase using the CORDIC computing. Therefore,  $K_1K_2 \cdot (M_2 + 2K_2 - 2 + 3P_2)$  additions are required in the 2<sup>nd</sup>-layer. When  $N$  is very large,  $K_1$  and  $K_2$  are correspondingly large. The computations for the phase then become relatively insignificant in PCA. In addition, as we consider the case with  $K_1 \approx M_1 \approx \sqrt{N}$  and  $K_2 \approx M_2 \approx \sqrt{M_1}$ , approximately  $3N$  additions are required for both the 1<sup>st</sup>- and the 2<sup>nd</sup>-layer. Note that the number of computations is almost the same in each layer, which is an inherent advantage of the multi-layer PCA. The comparison of the computational load between the two-layer PCA and the FFT-based method is shown in Table 4.1. The computational burden is significantly reduced in PCA, and the efficiency of PCA is thus clarified.

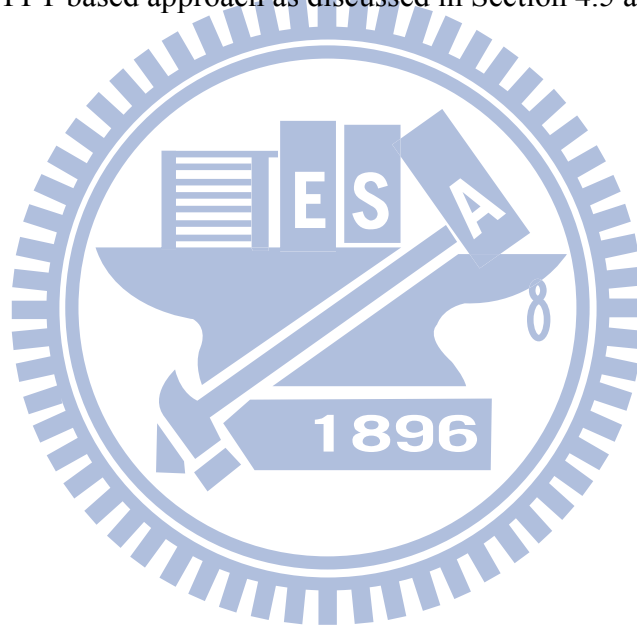
Table 4.1. Computations of the two-layer PCA and the FFT-based method

Method \ Operation	Multiplications	Additions
PCA	0	$6N$
FFT-base method	$2N \log_2 N$	$2N \log_2 N$

## 4.6 Summary

In this chapter, the PCA utilizing complex phasors for the PN sequence acquisition is proposed. Particularly, the PCA requires only complex additions but no complex multiplications. In addition, the acquisition performance can be improved via the use of the multi-layer scheme that also provides an inherent error detection capability. In the

demonstrated case using MLS of length  $N = 2^{20} - 1$  in the two-layer PCA, the correct segment of the 1<sup>st</sup>-layer is obtained with probability approaching one when  $\text{SNR} > -15\text{dB}$  as shown in Fig. 4.4. In addition, with the correct segment, the acquisition performance with correct probability greater than 0.9 can be attained for  $\text{SNR} \geq -20\text{dB}$  after the 2<sup>nd</sup>-layer as shown in Fig. 4.8. Note that, because the performance of PCA is determined by the chip error probability, the fading effect as well as the varying SNR can be represented by a nominal SNR that is associated with the actual chip error probability of the sequence, and the analysis results can thus be used appropriately. It is noteworthy that the PCA requires much less computation than the FFT-based approach as discussed in Section 4.5 and Table 4.1.



# Chapter 5

## Conclusions and Future Work

In this dissertation, the one-bit high-accuracy phase estimation for the tracking process is investigated. The traditional APD and the NB-DPD accurately estimate carrier phase in low and high SNR, respectively. However, the estimation bias becomes significant and their accuracy deteriorates in moderate SNR. Focusing on this SNR range, we propose the SNRaPD using the nonlinear least-square algorithm with the aid of SNR information to improve the accuracy. Because SNR information is critical to the phase accuracy and may be unavailable in many applications, the nonlinear least-square algorithm of SNRaPD is further developed to jointly estimate the accurate phase and SNR. Potential applications for the one-bit estimation method in GNSS and beacon receivers are illustrated regarding the attainable phase and SNR accuracy. It is worthwhile to mention that, owing to the efficient one-bit processing, the range of applications of the proposed method can be easily expanded by increasing the number of data and can accommodate signals with a high dynamic range.

On the other hand, we also propose the PCA method that applies the coherence phase of complex phasors to the PN sequence acquisition. Since the PCA simply utilizes the phase differences rather than the amplitude, the PCA requires only complex additions but no complex multiplications. Segmentation, phasor acquisition and the multi-layer scheme are designed in the PCA to enhance the noise-robustness capability. In particular, the multi-layer scheme also provides an inherent error detection capability. For applications having extra SNR margin, such as the high-SNR applications or the processing of de-noised signals, the use of PCA will require much less computation than the FFT-based method. The superior performance on the computation grants the PCA an efficient method when the length of a

sequence is so large that the FFT-based acquisition is infeasible.

Future works related to this dissertation involve two parts. First, concerning the carrier phase estimation, we assume that frequencies of the input and local carriers are identical throughout the work of one-bit phase and SNR estimation, which may not be the case in realistic applications. In practice, the Doppler shift may increase the error associated with the carrier phase estimation and the receiver may thus lose track of the incoming carrier signal. In order to broaden the scope of this work, the effect of Doppler shift should be considered and the tolerance of the frequency shift in the phase estimation algorithm needs additional study. Consequently, the associated influence on accuracy requires further investigation and clarification. Second, although the computational burden is significantly reduced in the PCA comparing with the FFT-based method, the performance of the FFT method is superior to that of PCA, i.e.  $P_{D1}$ , when the SNR is low. Therefore, new algorithms should be designed to enhance its noise-robustness of the method, such that  $P_{D1}$  could approach one in lower SNR. Once the 1<sup>st</sup>-layer detection is correct, it is almost assured that the detection of the further layer will also be correct.

## References

- [1] V. P. Ipatov, *Spread-spectrum and CDMA: Principles and Applications*, Hoboken, NJ: Wiley, 2005.
- [2] E. D. Kaplan and C. J. Hegarty, *Understanding GPS: Principles and Applications*, Norwood, MA: Artech House, 2006.
- [3] M. Dillinger, K. Madani and N. Alonistioti, *Software Defined Radio: Architectures, Systems and Functions*, Hoboken, NJ: Wiley, 2003.
- [4] H. Chang, "Presampling Filtering, Sampling and Quantization Effects on the Digital Matched Filter Performance," *Proceedings of International Telemetering Conference*, pp. 889–915, 1982.
- [5] B. W. Parkinson and J. J. Spilker, *Global Positioning System: Theory and Applications, Volume I*, Washington DC: AIAA, 1996.
- [6] H. C. Papadopoulos, G. W. Wornell, and A. V. Oppenheim, "Low-Complexity Digital Encoding Strategies for Wireless Sensor Networks," *Proceedings of the IEEE International Conference on Acoustic, Speech and Signal*, vol. 6, pp. 3273-3276, 1998.
- [7] P. H. Wu, "The Optimal BPSK Demodulator with a 1-bit A/D Front-end," *Proceedings of the Military Communications Conference of the IEEE*, vol. 3, pp. 730-735, 1998.
- [8] A. Brown and B. Wolt, "Digital L-Band Receiver Architecture with Direct RF Sampling," *IEEE Position Location and Navigation Symposium*, pp. 209-216, 1994.
- [9] R. H. Walden, "Analog-to-Digital Converter Survey and Analysis," *IEEE Journal on Selected Areas in Communications*, vol. 17, no. 4, pp. 539–550, 1999.
- [10] B. M. Ledvina and M. L. Psiaki, D. J. Sheinfeld, A. P. Cerruti, S. P. Powell, and P. M. Kintner, "A Real-Time GPS Civilian L1/L2 Software Receiver," *Proceedings of the International Technical Meeting of the Satellite Division of the ION*, pp. 986-1005, 2004.
- [11] M. R. Yuce and W. Liu, "A Low-Power Multirate Differential PSK Receiver for Space Applications," *IEEE Transactions on Vehicular Technology*, vol. 54, no. 6, pp. 2074-2084, 2005.
- [12] S. Kay, *Fundamentals of Statistical Signal Processing: Estimation Theory, volume 1*, Englewood Cliffs, NJ: Prentice Hall, 1993.
- [13] D. Rife and R. Boorstyn, "Single Tone Parameter Estimation from Discrete-Time Observations," *IEEE Transactions on Information Theory*, vol. IT-20, no. 5, pp. 591–598, 1974.
- [14] B. G. Quinn, "Estimation of Frequency, Amplitude, and Phase from the DFT of a time series," *IEEE Transactions on Signal Processing*, vol. 45, no. 3, pp. 814–817, 1997.
- [15] H. Fu and P. Y. Kam, "MAP/ML Estimation of the Frequency and Phase of a Single Sinusoid in Noise," *IEEE Transactions on Signal Processing*, vol. 55, no. 3, pp. 834–845, 2007.

- [16] Høst-Madsen and P. Händel, “Effects of sampling and quantization on single-tone frequency estimation,” *IEEE Transactions on Signal Processing*, vol. 48, no. 3, pp. 650–662, 2000.
- [17] O. Dabeer and A. Karnik, “Signal Parameter Estimation Using 1-Bit Dithered Quantization,” *IEEE Transactions on Information Theory*, vol. 52, no. 12, pp. 5389–5405, 2006.
- [18] O. Dabeer and E. Masry, “Multivariate Signal Parameter Estimation under Dependent Noise from 1-Bit Dithered Quantized Data,” *IEEE Transactions on Information Theory*, vol. 54, no. 4, pp. 1637–1654, 2008.
- [19] A. H. Pouzet, “Characteristics of Phase Detectors in Presence of Noise,” *Proceedings of the International Telemeter Conference*, pp. 818-828, 1972.
- [20] F. M. Gardner, *Phaselock Techniques*, Hoboken, NJ: Wiley, 2005.
- [21] C. F. Chang and M. S. Kao, “High-Accuracy Carrier Phase Discriminator for One-Bit Quantized Software-Defined Receivers,” *IEEE Signal Processing Letter*, vol. 15, pp. 397–400, 2008.
- [22] C. F. Chang, R. M. Yang and M. S. Kao, “Implementation of An Innovative Phase Discriminator for Improved Tracking Performance in One-Bit Software GPS Receiver,” *Proceedings of the National Technical Meeting of the ION*, pp. 798-803, 2008.
- [23] A. Polydoros and C. L. Weber, “A Unified Approach to Serial Search Spread-Spectrum Code Acquisition — Part II: A Matched-Filter Receiver,” *IEEE Transactions on Communications*, vol. COM-32, no. 5, pp. 542-560, 1984.
- [24] J. K. Holmes and C. C. Chen, “Acquisition Time Performance of PN Spread-Spectrum Systems,” *IEEE Transactions on Communications*, vol. COM-25, no. 8, pp. 778-783, 1977.
- [25] K. K. Chawla and D. V. Sarwate, “Parallel Acquisition of PN Sequences in DS/SS Systems,” *IEEE Transactions on Communications*, vol. 42, no. 5, pp. 2155-2164, 1994.
- [26] W. Zhuang, “Noncoherent Hybrid Parallel PN Code Acquisition for CDMA Mobile Communications,” *IEEE Transactions on Vehicular Technology*, vol. 45, no. 4, pp. 643-656, 1996.
- [27] M. Salih and S. Tantaratana, “A Closed-Loop Coherent Acquisition Scheme for PN Sequence Using an Auxiliary Sequence,” *IEEE Journal on Selected Areas in Communications*, vol. 14, no. 8, pp. 1653-1659, 1996.
- [28] J. G. R. Delva and I. Howitt, “PN Acquisition for DS/SS Using a Preloop Parallel Binary Search Phase Estimator and a Closed-Loop Selective Search Subsystem,” *IEEE Transactions on Wireless Communications*, vol. 3, no. 2, pp. 408-417, 2004.
- [29] J. W. Cooley and J. W. Tukey, “An Algorithm for the Machine Calculation of Complex Fourier Series,” *Mathematics of Computation*, vol. 19, no. 90, pp. 297–301, 1965.
- [30] W. T. Cochran, J. W. Cooley, D. L. Favon *etc.*, “What Is the Fast Fourier Transform,”



- Proceedings of the IEEE*, vol. 55, no. 10, pp. 1664–1674, 1967.
- [31] A. V. Oppenheim and R. W. Schaffer, *Discrete-Time Signal Processing*, Englewood Cliffs, NJ: Prentice Hall, 1989.
- [32] U. Cheng, W. J. Hurd and J. I. Statman, “Spread-Spectrum Code Acquisition in the Presence of Doppler Shift and Data Modulation,” *IEEE Transactions on Communications*, vol. 38, no. 2, pp. 241–250, 1990.
- [33] D. J. R. van Nee and A. J. R. M. Coenen, “New Fast GPS Code-Acquisition Technique Using FFT,” *Electronics Letters*, vol. 27, no. 2, pp. 158–160, 1991.
- [34] M. L. Mao, W. H. Lin, Y. F. Tseng, H. W. Tsao, and F. R. Chang, “New Acquisition Method in GPS Software Receiver with Split-Radix FFT Technique,” *the 9th International Conference on Advanced Communication Technology*, pp.722-727, 2007.
- [35] J. A. Starzyk and Z. Zhu, “Averaging Correlation for C/A Code Acquisition and Tracking in Frequency Domain,” *Proceedings of the 44th IEEE Midwest Symposium on Circuit and Systems*, pp. 905-908, 2001.
- [36] D. M. Lin and J. B. Y. Tsui, “Acquisition Schemes for Software GPS Receiver,” *Proceedings of ION GPS*, pp.317-325, 1998.
- [37] S. Z. Budisin, “Fast PN Sequence Correlation by Using FWT,” *Proceedings Mediterranean Electrotechnical Conference*, pp. 513-515, 1989.
- [38] A. Alaqeeli and J. Starzyk, “Hardware Implementation for Fast Convolution with a PN Code Using Field Programmable Gate Array,” *Proceedings of the 3rd Southeastern Symposium on System Theory*, pp.197-201, 2001.
- [39] A. Jeffrey, *Handbook of Mathematical Formulas and Integrals*, Amsterdam, Boston: Elsevier, 2004.
- [40] E. K. P. Chong and S. H. Zak, *An Introduction to Optimization*, Hoboken, NJ: Wiley, 2008.
- [41] P. A. Bernhardt, C. L. Siefring, I. J. Galysh, T. F. Rodillo, D. E. Koch, T. L. MacDonald, M. R. Wilkens, G. P. Landis, “Ionospheric Applications of the Scintillation and Tomography Receiver in Space (CITRIS) Mission When Used with the DORIS Radio Beacon Network,” *Journal of Geodesy*, vol. 80, no. 8-11, pp. 473–485, 2006.
- [42] C. J. Kikkert and O. P. Kenny, “A Digital Signal Processing Based Ka Band Satellite Beacon Receiver” *IEEE International Conference on Electronics, Circuits, and Systems*, pp. 1-8, 2008.
- [43] B. W. Parkinson and J. J. Spilker, *Global Positioning System: Theory and Applications, Volume II*, Chapter 21, Washington, DC: AIAA, 1996.
- [44] O. Montenbruck, M. Garcia-Fernandez, and J. Williams, “Performance Comparison of Semicodeless GPS Receivers for LEO Satellites,” *GPS Solutions*, vol. 10, no. 4, pp. 249–261, 2006.
- [45] C.-W. Huwang, T.-P. Tseng, T.-J. Lin, D. Švehla, U. Hugentobler, and B. F. Chao,

- “Quality Assessment of FORMOSAT-3/COSMIC and GRACE GPS Observables: Analysis of Multipath, ionospheric delay and phase residual in orbit determination,” *GPS Solutions*, vol. 14, no. 1, pp. 121–131, 2010.
- [46] O. Montenbruck and R. Kroes, “In-flight performance analysis of the CHAMP BlackJack GPS Receiver,” *GPS Solutions*, vol. 7, no. 2, pp. 74-86, 2003.
- [47] C.-W. Hwang, T.-P. Tseng, T.-J. Lin, and D. Švehla, B. Schreiner, “Precise orbit determination for the FORMOSAT-3/COSMIC satellite mission using GPS,” *Journal of Geodesy*, vol. 83, no. 5, pp. 477-489, 2009.
- [48] D. Švehla and M. Rothacher, “Kinematic and reduced-dynamic precise orbit determination of low earth orbiters,” *Advances in Geosciences*, vol. 1, pp. 47-56, 2003.
- [49] A. Jäggi, U. Hugentobler, H. Bock, and G. Beulter, “Precise orbit determination for GRACE using undifferenced or doubly differenced GPS data,” *Advances in Space Research*, vol. 39, no. 10, pp. 1612-1619, 2007.
- [50] P. A. Bernhardt, C. A. Selcher, S. Basu, G. Bust, and S. C. Reising, “Atmospheric Studies with the Tri-Band Beacon Instrument on the COSMIC Constellation,” *Terrestrial, Atmospheric and Oceanic Sciences*, vol. 11, no. 1, pp. 291-312, 2000.
- [51] M. Yamamoto, “Digital beacon receiver for ionospheric TEC measurement developed with GNU radio,” *Earth Planets Space*, vol. 60, no. 11, pp. e21-e24, 2008.
- [52] K. F. Davies, *Ionospheric Radio*, Peter Peregrinus: London, UK, 1990.
- [53] C. Rocken, Y.-H. Kuo, W. S. Schreiner, D. Hunt, S. Sokolovskiy, and C. McCormick, “COSMIC System Description,” *Terrestrial, Atmospheric and Oceanic Sciences*, vol. 11, no. 1, pp. 21-52, 2000.
- [54] J. E. Volder, “The CORDIC Trigonometric Computing Technique”, *IRE Transactions Electronic Computers.*, vol. EC-8, no. 3, pp. 330–334, 1959.
- [55] P. Beckmann, *Probability in Communication Engineering*, New York, NY: Harbrace, 1967.

# Appendix

## A. Derivation of mean and variance of I-Q channel outputs

According to Eq. (2.4), for  $\Phi_k \in [0, \pi)$ , we have  $\sin \Phi_k \geq 0$ . In inphase (I) channel, the conditional probabilities are denoted as

$$\text{Prob}(a_k = 1 | \Phi_k) = \text{Prob}(\sin(\Phi_k + \phi) + v_k \geq 0 | \Phi_k) = 1 - P_k \quad (\text{A1})$$

$$\text{Prob}(a_k = -1 | \Phi_k) = \text{Prob}(\sin(\Phi_k + \phi) + v_k < 0 | \Phi_k) = P_k. \quad (\text{A2})$$

Thus the mean and variance of  $a_k$  are given by

$$\begin{aligned} \mu_{a_k} &= 1 \cdot \text{Prob}(a_k = 1 | \Phi_k) + (-1) \cdot \text{Prob}(a_k = -1 | \Phi_k) \\ &= 1 - 2P_k \end{aligned} \quad (\text{A3})$$

$$\begin{aligned} \sigma_{a_k}^2 &= \text{E}[a_k^2] - \mu_{a_k}^2 \\ &= 1 - (1 - 2P_k)^2 \\ &= 4(P_k - P_k^2). \end{aligned} \quad (\text{A4})$$

Similarly, for  $\Phi_k \in [\pi, 2\pi)$ , we have  $\sin \Phi_k \leq 0$ . The conditional probabilities are denoted as

$$\text{Prob}(a_k = 1 | \Phi_k) = \text{Prob}(\sin(\Phi_k + \phi) + v_k < 0 | \Phi_k) = P_k \quad (\text{A5})$$

$$\text{Prob}(a_k = -1 | \Phi_k) = \text{Prob}(\sin(\Phi_k + \phi) + v_k \geq 0 | \Phi_k) = 1 - P_k. \quad (\text{A6})$$

The associated mean and variance are given by

$$\mu_{a_k} = 2P_k - 1 \quad (\text{A7})$$

$$\sigma_{a_k}^2 = 4(P_k - P_k^2). \quad (\text{A8})$$

Assume the noise component in each sample is independent. Since  $\Phi_k$ 's are uniformly distributed over  $[0, 2\pi)$ , we have

$$\mu_{I_p} = \frac{1}{p} \left[ \sum_{\Phi_k \in [0, \pi)} (1 - 2P_k) + \sum_{\Phi_k \in [\pi, 2\pi)} (2P_k - 1) \right] \quad (\text{A9})$$

$$\sigma_I^2 = \frac{4}{p^2} \sum_{k=0}^{p-1} P_k - P_k^2. \quad (\text{A10})$$

Similarly, by the same calculation, the mean and variance for the quadrature (Q) channel are obtained by

$$\mu_{Q_p} = \frac{1}{p} \left[ \sum_{\Phi_k \in [0, \pi/2) \cup [3\pi/2, 2\pi)} (1 - 2P_k) + \sum_{\Phi_k \in [\pi/2, 3\pi/2)} (2P_k - 1) \right] \quad (\text{A11})$$

$$\sigma_Q^2 = \frac{4}{p^2} \sum_{k=0}^{p-1} P_k - P_k^2. \quad (\text{A12})$$

## B. Power series representation of mean and variance of I-Q channel outputs

The power series representation of the Q-function is given by [39]

$$Q(x) = \frac{1}{2} - \frac{1}{\sqrt{2\pi}} \sum_{m=0}^{\infty} \frac{(-1)^m x^{2m+1}}{m! 2^m (2m+1)}. \quad (\text{B1})$$

Hence Eq. (2.10) is rewritten by

$$\begin{aligned}\mu_{I_p} &= \frac{1}{p} \left\{ \sum_{\Phi_k \in [\pi, 2\pi)} \left[ 1 - \frac{2}{\sqrt{2\pi}} \sum_{m=0}^{\infty} \frac{(-1)^m (\gamma \sin(\Phi_k + \phi))^{2m+1}}{m! 2^m (2m+1)} \right] - \sum_{\Phi_k \in [0, \pi)} \left[ 1 - \frac{2}{\sqrt{2\pi}} \sum_{m=0}^{\infty} \frac{(-1)^m (\gamma \sin(\Phi_k + \phi))^{2m+1}}{m! 2^m (2m+1)} \right] \right\} \\ &= \sqrt{\frac{2}{\pi}} \sum_{m=0}^{\infty} \frac{(-1)^m \gamma^{2m+1}}{m! 2^m (2m+1)} \left\{ \frac{1}{p} \left[ \sum_{\Phi_k \in [0, \pi)} \sin(\Phi_k + \phi)^{2m+1} - \sum_{\Phi_k \in [\pi, 2\pi)} \sin(\Phi_k + \phi)^{2m+1} \right] \right\}.\end{aligned}\quad (\text{B2})$$

Suppose we choose  $f_s$  such that  $p$  is sufficiently large in Eq. (2.3), Eq. (B2) is approximated by

$$\mu_{I_p} \cong \sqrt{\frac{2}{\pi}} \sum_{m=0}^{\infty} \frac{(-1)^m \gamma^{2m+1}}{m! 2^m (2m+1)} \left\{ \frac{1}{2\pi} \left[ \int_0^{\pi} \sin^{2m+1}(\Phi + \phi) d\Phi - \int_{\pi}^{2\pi} \sin^{2m+1}(\Phi + \phi) d\Phi \right] \right\} \quad (\text{B3})$$

where  $d\Phi = 2\pi/p \rightarrow 0$ .

By the power series representation of the integrand involving the odd power of  $\sin(x)$  [39, Sec. 9.2.1], Eq. (B3) can be further written as

$$\mu_{I_p} = \frac{4}{\sqrt{2\pi}^{3/2}} \sum_{m=0}^{\infty} \frac{\gamma^{2m+1}}{m! 2^{3m} (2m+1)} \left[ \sum_{l=0}^m (-1)^l \binom{2m+1}{l} \frac{\cos(2m+1-2l)\phi}{2m+1-2l} \right]. \quad (\text{B4})$$

The derivation of the mean value of the Q-channel output is omitted because of similarity. In addition, using Eq. (B1), the variances of the I-Q channel outputs of Eq. (2.7) are derived by

$$\begin{aligned}\sigma_{I_p}^2 &= \sigma_{Q_p}^2 \\ &= \frac{4}{p^2} \sum_{k=0}^{p-1} \left\{ \left[ \frac{1}{2} - \frac{1}{\sqrt{2\pi}} \sum_{m=0}^{\infty} \frac{(-1)^m (\gamma \sin(\Phi_k + \phi))^{2m+1}}{m! 2^m (2m+1)} \right] - \left[ \frac{1}{2} - \frac{1}{\sqrt{2\pi}} \sum_{m=0}^{\infty} \frac{(-1)^m (\gamma \sin(\Phi_k + \phi))^{2m+1}}{m! 2^m (2m+1)} \right]^2 \right\} \\ &= \frac{1}{p} - \frac{2}{p^2 \pi} \sum_{k=0}^{p-1} \left[ \sum_{m=0}^{\infty} \frac{(\gamma \sin(\Phi_k + \phi))^{4m+2}}{(m! 2^m (2m+1))^2} + 2 \sum_{x=0}^{\infty} \sum_{y=x+1}^{\infty} \frac{(-1)^{x+y} (\gamma \sin(\Phi_k + \phi))^{2(x+y)+2}}{x! y! 2^{x+y} (2x+1)(2y+1)} \right]^2 \\ &\cong \frac{1}{p} - \frac{2}{p\pi} \cdot \frac{1}{2\pi} \int_0^{2\pi} \left[ \sum_{m=0}^{\infty} \frac{(\gamma \sin(\Phi + \phi))^{4m+2}}{(m! 2^m (2m+1))^2} + 2 \sum_{x=0}^{\infty} \sum_{y=x+1}^{\infty} \frac{(-1)^{x+y} (\gamma \sin(\Phi + \phi))^{2(x+y)+2}}{(x! y! 2^{x+y} (2x+1)(2y+1))} \right] d\Phi.\end{aligned}\quad (\text{B5})$$

By the power series representation of the integrand involving the even power of  $\sin(x)$  [39,

Sec. 9.2.1], Eq. (B5) can be further written as

$$\begin{aligned} \sigma_{I_p}^2 &= \sigma_{Q_p}^2 \\ &= \frac{1}{p} - \frac{2}{p\pi} \left[ \sum_{m=0}^{\infty} \binom{4m+2}{2m+1} \frac{\gamma^{4m+2}}{(m!2^{3m+1}(2m+1))^2} \right. \\ &\quad \left. + 2 \sum_{x=0}^{\infty} \sum_{y=x+1}^{\infty} \binom{2x+2y+2}{x+y+1} \frac{(-1)^{x+y} \gamma^{2(x+y)+2}}{x!y!2^{3(x+y)+2}(2x+1)(2y+1)} \right]. \end{aligned} \quad (\text{B6})$$

### C. Magnitude and phase distribution of $G_m$

The distribution of  $G_m$  in the 1<sup>st</sup>-layer,  $G_m^{(1)}$ , is derived first. We rewrite Eq. (4.38) as

$$w_n = x_n + \beta_n \bar{x}_n \quad (\text{C1})$$

where  $\beta_n \in \{0, 2\}$  and  $\bar{x}_n$  denotes the inverse of  $x_n$ .

In Eq. (C1), when  $\beta_n = 2$ , we have  $w_n = \bar{x}_n$ , indicating that an error occurs because of noise  $\zeta_n$ . The corresponding error probability is given by

$$\begin{aligned} P_e &= \Pr(\beta_n = 2) \\ &= Q(1/\sigma_n) \end{aligned} \quad (\text{C2})$$

where  $Q(z) = \int_z^{\infty} e^{-x^2/2} dx$ .

We can represent Eq. (4.41) as

$$\begin{aligned} W_i &= \sum_{n=0}^{M_1-1} w_{nK_1+i} \alpha^{-n} \\ &= \sum_{n=0}^{M_1-1} x_{nK_1+i} \alpha^{-n} + \sum_{n=0}^{M_1-1} \beta_{nK_1+i} \bar{x}_{nK_1+i} \alpha^{-n} \\ &= X_i + \sum_{n=0}^{M_1-1} \beta_{nK_1+i} \bar{x}_{nK_1+i} \alpha^{-n} \end{aligned} \quad (\text{C3})$$

where  $X_i = \sum_{n=0}^{M_1-1} x_{nK_1+i} \alpha^{-n}$  is assumed to be fixed.

Let  $E\{z\}$  denote the expected value of  $z$ . The mean value of  $W_i$  is obtained by

$$\begin{aligned}
E\{W_i\} &= E\left\{X_i + \sum_{n=0}^{M_1-1} \beta_{nK_1+i} \bar{x}_{nK_1+i} \alpha^{-n}\right\} \\
&= X_i + \sum_{n=0}^{M_1-1} E\{\beta_{nK_1+i}\} \bar{x}_{nK_1+i} \alpha^{-n} \\
&= X_i + 2P_e \cdot \sum_{n=0}^{M_1-1} \bar{x}_{nK_1+i} \alpha^{-n} \\
&= (1-2P_e) \cdot X_i
\end{aligned} \tag{C4}$$

where  $E\{\beta_{nK_1+i}\} = 2P_e$  and  $\sum_{n=0}^{M_1-1} \bar{x}_{nK_1+i} \alpha^{-n} = -X_i$ .

Furthermore, to obtain the variance of  $W_i$ , we calculate

$$\begin{aligned}
E\{W_i W_i^*\} &= E\left\{\left(X_i + \sum_{n=0}^{M_1-1} \beta_{nK_1+i} \bar{x}_{nK_1+i} \alpha^{-n}\right) \cdot \left(X_i + \sum_{m=0}^{M_1-1} \beta_{mK_1+i} \bar{x}_{mK_1+i} \alpha^{-m}\right)^*\right\} \\
&= X_i X_i^* + X_i \cdot \sum_{m=0}^{M_1-1} E\{\beta_{mK_1+i}\} \bar{x}_{mK_1+i} \alpha^m + X_i^* \cdot \sum_{n=0}^{M_1-1} E\{\beta_{nK_1+i}\} \bar{x}_{nK_1+i} \alpha^{-n} \\
&\quad + E\left\{\left(\sum_{n=0}^{M_1-1} \beta_{nK_1+i} \bar{x}_{nK_1+i} \alpha^{-n}\right) \cdot \left(\sum_{m=0}^{M_1-1} \beta_{mK_1+i} \bar{x}_{mK_1+i} \alpha^m\right)\right\} \\
&= |X_i|^2 - 2P_e \cdot X_i X_i^* - 2P_e \cdot X_i^* X_i + \sum_{\substack{n=0 \\ m=n}}^{M_1-1} E\{\beta_{nK_1+i} \beta_{mK_1+i}\} \bar{x}_{nK_1+i} \bar{x}_{mK_1+i} \alpha^{m-n} \\
&\quad + E\left\{\sum_{n=0}^{M_1-1} \beta_{nK_1+i} \bar{x}_{nK_1+i} \alpha^{-n} \sum_{\substack{m=0 \\ m \neq n}}^{M_1-1} \beta_{mK_1+i} \bar{x}_{mK_1+i} \alpha^m\right\} \\
&\approx |X_i|^2 - 4P_e |X_i|^2 + 4P_e \sum_{\substack{n=0 \\ m=n}}^{M_1-1} \bar{x}_{nK_1+i} \bar{x}_{mK_1+i} \alpha^{m-n} \\
&= |X_i|^2 - 4P_e |X_i|^2 + 4P_e M_1
\end{aligned} \tag{C5}$$

where  $E \left\{ \sum_{n=0}^{M_1-1} \beta_{nK_1+i} \bar{x}_{nK_1+i} \alpha^{-n} \sum_{\substack{m=0 \\ m \neq n}}^{M_1-1} \beta_{mK_1+i} \bar{x}_{mK_1+i} \alpha^m \right\} \approx 0$  and  $E\{\beta_{nK_1+i} \beta_{mK_1+i}\} = 4P_e$  when

$$m = n.$$

By using Eq. (C4) and Eq. (C5), the variance of  $W_i$  is derived by

$$\begin{aligned} \text{Var}\{W_i\} &= E\{|W_i|^2\} - (|E\{W_i\}|)^2 \\ &= E\{W_i W_i^*\} - E\{W_i\} \cdot (E\{W_i\})^* \\ &= |X_i|^2 - 4P_e |X_i|^2 + 4P_e M_1 - ((1-2P_e)X_i) \cdot ((1-2P_e)X_i)^* \\ &= 4P_e M_1 - 4P_e^2 |X_i|^2. \end{aligned} \tag{C6}$$

It is reasonable to assume that  $\{x_{nK_1+i}\}$  involved in  $X_i$  is a PN sequence of length  $M_1$ .

Similar to Eq. (4.8), we have

$$|X_i|^2 \approx M_1 + 1. \tag{C7}$$

Let the code phase shift between input and local MLS be  $q = c_1 K_1 + d_1$ . Considering the sidelobe of  $|G_m^{(1)}|$ , i.e.  $m \neq d_1$ , in Eq. (4.43), the phases  $\psi_{i,m}$  can be considered to be uniformly distributed between  $-\pi$  and  $\pi$ . According to [55], the magnitude distribution of  $|G_m^{(1)}|$ , denoted by  $r_s$ , can be modeled using Rayleigh distribution, given as

$$f(r_s) = \frac{r_s}{K_1/2} e^{-r_s^2/K_1} \tag{C8}$$

where  $r_s \geq 0$ .

On the other hand, for the  $|G_m^{(1)}|$  with  $m = d_1$ , Eq. (4.43) is represented by



$$\begin{aligned}
G_{d_1}^{(1)} &= \sum_{i=0}^{K_1-1} e^{j\psi_{i,m}} \\
&= \sum_{i=0}^{K_1-1} e^{j\frac{2\pi}{M_1}c_1 + \Delta\phi_i}
\end{aligned} \tag{C9}$$

where  $\Delta\phi_i$  denotes the phase error induced by noise.

Without loss of generality, we assume  $c_1 = 0$ . Then Eq. (C9) becomes

$$G_{d_1}^{(1)} = \sum_{i=0}^{K_1-1} e^{j\Delta\phi_i}. \tag{C10}$$

The  $\Delta\phi_i$  denotes the phase difference between the input phasor  $W_i$  and local phasor  $Y_i$  caused by noise. Since we have the mean and variance of  $W_i$  in Eq. (C4) and Eq. (C6), according to [55, Sec. 4.4], the distribution of  $\Delta\phi_i$  can be approximated by

$$f(\Delta\phi_i) = \frac{1}{2\pi} e^{-\rho} \left[ 1 + G\sqrt{\pi} \exp(G^2)(1 + \operatorname{erf}(G)) \right] \tag{C11}$$

where  $\rho = \frac{(E\{W_i\})^2}{\operatorname{Var}\{W_i\}}$ ,  $G = \sqrt{\rho} \cos(\Delta\phi_i)$  and  $-\pi \leq \Delta\phi_i \leq \pi$ .

Moreover, in order to obtain the magnitude distribution of  $G_{d_1}^{(1)}$ , Eq. (C10) is reformulated by

$$\begin{aligned}
G_{d_1}^{(1)} &= \sum_{i=0}^{K_1-1} e^{j\Delta\phi_i} \\
&= \sum_{i=0}^{K_1-1} \cos(\Delta\phi_i) + j \sum_{i=0}^{K_1-1} \sin(\Delta\phi_i) \\
&= \Gamma_{\operatorname{Re}} + j\Gamma_{\operatorname{Im}}
\end{aligned} \tag{C12}$$

where  $\Gamma_{\operatorname{Re}} = \sum_{i=0}^{K_1-1} \cos(\Delta\phi_i)$  and  $\Gamma_{\operatorname{Im}} = \sum_{i=0}^{K_1-1} \sin(\Delta\phi_i)$ .

We assume that each  $\cos(\Delta\phi_i)$  and  $\sin(\Delta\phi_i)$  are independent and identically distributed

(i.i.d.) random variables. Let  $\mathcal{N}(\mu, \sigma^2)$  denote the normal distribution function with mean  $\mu$  and variance  $\sigma^2$ . By the central limit theorem,  $\Gamma_{\text{Re}}$  and  $\Gamma_{\text{Im}}$  can be approximated by two normal distributions  $\mathcal{N}(\mu_{\text{Re1}}, \sigma_{\text{Re1}}^2)$  and  $\mathcal{N}(\mu_{\text{Im1}}, \sigma_{\text{Im1}}^2)$ , respectively, and the parameters are obtained by

$$\begin{aligned}\mu_{\text{Re1}} &= E \left\{ \sum_{i=0}^{K_1-1} \cos(\Delta\phi_i) \right\} \\ &= \sum_{i=0}^{K_1-1} E \{ \cos(\Delta\phi_i) \}\end{aligned}\tag{C13}$$

$$\begin{aligned}\sigma_{\text{Re1}}^2 &= \text{Var} \left\{ \sum_{i=0}^{K_1-1} \cos(\Delta\phi_i) \right\} \\ &= \sum_{i=0}^{K_1-1} \text{Var} \{ \cos(\Delta\phi_i) \}\end{aligned}\tag{C14}$$

$$\mu_{\text{Im1}} = \sum_{i=0}^{K_1-1} E \{ \sin(\Delta\phi_i) \}\tag{C15}$$

$$\sigma_{\text{Im1}}^2 = \sum_{i=0}^{K_1-1} \text{Var} \{ \sin(\Delta\phi_i) \}\tag{C16}$$

where  $\text{Var}\{\bullet\}$  denotes the variance.

Numerically, we find  $\mu_{\text{Re1}} \neq 0$ ,  $\mu_{\text{Im1}} = 0$  and  $\sigma_{\text{Re1}}^2 \cong \sigma_{\text{Im1}}^2$ . For simplicity, let  $\sigma_{p1}^2 = (\sigma_{\text{Re1}}^2 + \sigma_{\text{Im1}}^2)/2$ . According to [55], the magnitude of  $G_{d_1}^{(1)}$ , denoted by  $r_p$ , can be modeled by Rice distribution given as

$$f(r_p) = \frac{r_p}{\sigma_{p1}^2} e^{-(r_p^2 + \mu_{\text{Re1}}^2)/2\sigma_{p1}^2} \cdot I_0 \left( \frac{r_p \mu_{\text{Re1}}}{\sigma_{p1}^2} \right)\tag{C17}$$

where  $r_p \geq 0$  and  $I_0(\cdot)$  is the modified Bessel function of the first kind with order zero.

In addition, the joint magnitude of phase distribution of  $G_{d_1}^{(1)}$  is given by

$$f(r_p, \varphi) = \frac{r_p}{2\pi\sigma_{p1}^2} \exp\left(-\frac{r_p^2 + \mu_{\text{Re}1}^2 - 2r_p\mu_{\text{Re}1}\cos\varphi}{2\sigma_{p1}^2}\right) \quad (\text{C18})$$

where  $-\pi \leq \varphi < \pi$ .

The derivation of magnitude and phase distribution of  $G_m$  can be applied to other layers. We take the 2<sup>nd</sup>-layer for example. For the sidelobe of  $|G_n^{(2)}|$  with  $n \neq d_2$  in Eq. (4.52), the phases  $\psi_{i,t+n}$  can be considered to be uniformly distributed between  $-\pi$  and  $\pi$ . The distribution of sidelobe of  $|G_n^{(2)}|$ , denoted by  $l_s$ , can then be modeled by

$$f(l_s) = \frac{l_s}{K_1 K_2 / 2} e^{-l_s^2 / K_1 K_2} \quad (\text{C19})$$

where  $l_s \geq 0$ .

Moreover, let

$$\mu_{\text{Re}2} = \sum_{i=0}^{K_1-1} \sum_{t=0}^{K_2-1} E\{\cos(\psi_{i,t+d_2})\} \quad (\text{C20})$$

$$\sigma_{\text{Re}2}^2 = \sum_{i=0}^{K_1-1} \sum_{t=0}^{K_2-1} \text{Var}\{\cos(\psi_{i,t+d_2})\} \quad (\text{C21})$$

$$\mu_{\text{Im}2} = \sum_{i=0}^{K_1-1} \sum_{t=0}^{K_2-1} E\{\sin(\psi_{i,t+d_2})\} \quad (\text{C22})$$

$$\sigma_{\text{Im}2}^2 = \sum_{i=0}^{K_1-1} \sum_{t=0}^{K_2-1} \text{Var}\{\sin(\psi_{i,t+d_2})\}. \quad (\text{C23})$$

The magnitude of  $G_n^{(2)}$  with  $n = d_2$ , denoted by  $l_p$ , is modeled by

$$f(l_p) = \frac{l_p}{\sigma_{p2}^2} e^{-(l_p^2 + \mu_{\text{Re}2}^2)/2\sigma_{p2}^2} \cdot I_0\left(\frac{l_p \mu_{\text{Re}2}}{\sigma_{p2}^2}\right) \quad (\text{C24})$$

where  $l_p \geq 0$  and  $\sigma_{p2}^2 = (\sigma_{\text{Re}2}^2 + \sigma_{\text{Im}2}^2)/2$ .

In addition, the joint magnitude of phase distribution of  $G_{d_2}^{(2)}$  is denoted by

$$f(l_p, \mathcal{G}) = \frac{l_p}{2\pi\sigma_{p2}^2} \exp\left(-\frac{l_p^2 + \mu_{\text{Re}2}^2 - 2l_p \mu_{\text{Re}2} \cos \mathcal{G}}{2\sigma_{p2}^2}\right) \quad (\text{C25})$$

where  $-\pi \leq \mathcal{G} < \pi$ .

